Effect of swift heavy ion irradiation and annealing on the microstructure and migration behaviour of implanted Sr and Ag in SiC

BY

HESHAM ABDELBAGI ALI

Submitted in partial fulfilment of the requirements for the degree of

DOCTOR OF PHILOSOPHY (PhD) IN PHYSICS

In the Faculty of Natural and Agricultural Sciences at University of Pretoria

November……..2019

Supervisor/Promoter: Prof J. B. Malherbe

Co- supervisor: Prof T. T. Hlatshwayo

UNIVERSITEIT VAN PRETORIA
UNIVERSITY OF PRETORIA
YUNIBESITHI YA PRETORIA

DECLARATION

I, Hesham Abdelbagi Ali Abdelbagi, declare that the dissertation, which I hereby submit for the degree of PhD in University of Pretoria, is my own work and has not been submitted by me for a degree at this or any other tertiary institution.

Signature: ……

Date: ……

SUMMARY

Effect of swift heavy ion irradiation and annealing on the microstructure and migration behaviour of implanted Sr and Ag in SiC

BY

Hesham Abdelbagi Ali

Submitted in partial fulfilment of the requirements for the degree of (PhD) in Physics in the Faculty of Natural and Agricultural Science, University of Pretoria

Supervisor/Promoter: Prof. J. B. Malherbe

Co- supervisor: Prof. T. T. Hlatshwayo

Silicon carbide has been used in many applications in the electronics industry and material sciences. In the nuclear power generation, SiC is used as the main containment layer in the construction of fuel particles of the Generation IV nuclear reactors for the containment of fission products (FPs). SiC performs well in the containment of most FPs during operation temperatures up to 1000 ^{o}C. However, silver (Ag) and strontium (Sr) have been able to escape the fuel particle at temperatures higher than 1000 ^{o}C. The escape of Ag and Sr out of the fuel particle has given birth to the extensive research done on the transport properties of Ag in SiC and the study of structural properties of SiC as used in fuel particles.

This thesis is divided into two parts. At first, we study the structural changes in polycrystalline SiC implanted at room temperature (RT) with Ag and Sr ions before and after SHI irradiation at room temperature and the effect of annealing. The study also investigates the effect of SHI irradiation and the annealing on the migration behaviour of Ag and Sr in SiC.

The implantations were performed as follows: the 360 keV silver (Ag) and 360 keV strontium (Sr) ions were implanted separately into silicon carbide at room temperature to a fluence of 2×10^{16} cm^{-2}. Some of these implanted samples were irradiated by swift heavy ions (SHI). The samples were then characterized by the use of several techniques to determine the damage created in SiC by the ion bombardment process, the distributions of the silver and strontium ions and the effects of SHI irradiation on these distributions. The irradiated and un-irradiated

but Ag or Sr implanted samples were isochronally annealed in vacuum at temperatures ranging from 1100 ˚C to 1500 ˚C in steps of 100 ºC for 5 hours.

Raman spectroscopy technique was used to study the structure of all sets of samples (i.e. irradiated and un-irradiated samples implanted with Ag or Sr) before and after the vacuum annealing process. Scanning electron microscopy was used to monitor the surface modifications after each annealing cycle. The migration behaviour of silver (as well as strontium) in the irradiated and un-irradiated but implanted samples before and after each annealing step were investigated by Rutherford backscattering spectrometry (RBS) technique.

Raman results showed that implantation of Ag (as well as Sr) into SiC at room temperature caused the disappearance of characteristic SiC Raman peaks, an indication of an amorphized layer of silicon carbide. Irradiation of the as-implanted SiC with 167 MeV Xe ions at room temperature to fluences of 3.4×10^{14} cm^{-2} and 8.4×10^{14} cm^{-2} caused partial reappearance of rather broader SiC Raman characteristic peaks indicating some recrystallization of the initially amorphized layer of SiC. This partial recrystallization of the SiC layer was caused by the high electronic energy deposition by Xe ions irradiation at 167 MeV.

A full recrystallization of the silicon carbide was observed resulting in the appearance of the characteristic Raman peaks of SiC for un-irradiated but implanted samples annealed at 1100 °C. For SHI irradiated SiC samples annealed at 1100 °C showed poor recrystallization with a abroad Si-Si peak and C-C peak. The differences in recrystallization between the irradiated and un-irradiated but implanted samples was due to impurities (e.g. Ag or Sr atoms) within the substrate. Moreover, the results showed that the longitudinal optical (LO) phonon mode of SiC for the un-irradiated but implanted sample had a significantly higher intensity compared to that of the SHI irradiated samples. This suggested that the un-irradiated but implanted sample had on average, larger crystals compared to the irradiated samples. The differences in the average crystal sizes between irradiated and un-irradiated but implanted samples was due to the fact that the initial surface/layer states of SiC were in different before annealing, i.e. the un-irradiated samples were amorphous while the irradiated samples were composed of crystallites that were randomly orientated in an amorphous matrix. After annealing irradiated and un-irradiated but implanted samples sequentially up to 1500 °C, two peaks appeared at 1350 and 1580 cm^{-1} corresponding to the D and G bands in the Raman spectra, which are more dominant in all the carbon materials. The presence of the D and G peaks indicates the presence of a carbon layer on the sample surfaces after annealing at 1500 ºC. The free carbon on the surfaces

was due to thermal decomposition of SiC causing the sublimation of silicon, thus leaving a free carbon layer on the surface.

The average crystal sizes were determined from the SEM images of the irradiated and un-irradiated Ag or Sr implanted samples, all annealed at temperatures from 1100 to 1300 °C. The average crystal sizes were not determined for the irradiated and un-irradiated but implanted samples annealed at 1400 ^{o}C and 1500 ^{o}C due to the absence of distinct crystals and the presence of carbon and some crystal clusters on the surfaces. The SEM results agreed with the Raman results which showed that annealing of the un-irradiated but implanted samples resulted in larger average crystal size compared to the irradiated samples annealed under the same conditions.

For room temperature Ag implanted samples, isochronal annealing showed a slight migration of implanted Ag towards the surface, accompanied by a slight loss of Ag after the first annealing cycle (i.e. 1100 ^{o}C). However, annealing the SHI irradiated samples at 1100 ^{o}C resulted in significant loss of about 42% and 54% of implanted Ag in both the SHI irradiated samples at fluences of 3.4×10^{14} cm^{-2} and 8.4×10^{14} cm^{-2} respectively. This was due to the presence of a large number of pores in the surfaces of the SHI irradiated samples as compared to the implanted but un-irradiated samples.

The diffusion coefficients for the irradiated samples at fluences of 3.4×10^{14} cm^{-2} and 8.4×10^{14} cm^{-2} annealed at 1100 ^{o}C were found to be 2×10^{-20} m^2/s and 3.2×10^{-20} m^2/s, respectively. However, there was no measurable diffusion for Ag in un-irradiated but implanted samples which is obviously below our detection limit of 10^{-21} m^2 s^{-1}. These results indicated that bombardment with swift heavy ions enhanced the diffusion of Ag in SiC.

Migration of implanted Sr was already taking place at 1100 °C in both irradiated and un-irradiated but Sr implanted samples. The un-irradiated but Sr implanted samples annealed at 1100 ^{o}C showed a strong migration of Sr towards the surface accompanied by a significant loss (of about 25%) of implanted Sr. In the irradiated samples, Sr migrated towards the surface and into the undamaged bulk after annealing at 1100 ^{o}C. This migration was accompanied by minor loss of about 3% and no loss of implanted Sr for the samples irradiated at 3.4×10^{14} cm^{-2} and 8.4×10^{14} cm^{-2}, respectively. At 1100 ˚C, the un-irradiated but Sr implanted samples which exhibited pores on the surface showed high loss of Sr as compared to the irradiated samples which did not show any pores on the surface. Therefore, the different amounts of retained

strontium after annealing were due to the difference in surface structure of the samples. The un-irradiated but Sr implanted sample retained about 25% of Sr after annealing up to 1500 ^{o}C, while no Sr was retained in the 8.4×10^{14} cm^{-2} and 3.4×10^{14} cm^{-2} irradiated samples after annealing at 1300 and 1400 ^{o}C respectively. From these results, it is quite clear that Sr loss was favoured in the irradiated SiC structure.

Acknowledgements

I will like to acknowledge the following people for their support and valuable contribution in the success of my study.

- My academic promoter, Prof. J. B. Malherbe, my co-promoter Prof. T. T. Hlatshwayo for their wonderful guidance, support, discussion during the course of this study.
- The head of Physics department Prof. C. C. Theron for allowing me to work in the department of Physics.
- Dr. Eric Njoroge, Mr J. Smith and Mr T. M. Mohlala for all the help they provided with the accelerator.
- My friends in the department of physics and special thanks to my colleagues in the Nuclear materials research group, especially T. M. Mohlala, M. Y. A. Ismail, Z. A. A. Yousif, I. A. Joseph and T. A. O. Jafer.
- Mrs T. A. O. Jafer (my lovely wife and the Queen of my heart) for her love, patience, continuous support, encouragement and prayers.
- My parents, brothers, sisters and family members, who supported me during my studies and life.
- The financial assistance of the NRF is hereby acknowledged. Opinions expressed and conclusions arrived at, are those of the author and not to be necessarily attributed to the NRF.

LIST OF ABBREVIATIONS.

CCD - Charged Coupled Devices

CFE - Cold Field Emitter

CVD - Chemical vapour deposited

EBSD - Electron Backscatter Diffraction

EDS – Energy dispersive X-rays spectroscopy

FESEM- Field Emission Scanning Electron Microscope

FPs - Fission Products

FWHM- Full Width at Half Maximum

GeV – Giga electron volt

He – Helium

HTGR – High Temperature Gas-cooled Reactors

IPyC - Inner pyrolytic carbon

keV – Kilo Electron Volt

MCA - Multi-channel analyser

MeV – Mega Electron Volt

OPyC – Outer pyrolytic carbon

PBMR – Pebble Bed Modular Reactor

RBS- Rutherford Backscattering spectrometry

SE - Secondary Electrons

SEM - Scanning electron microscopy

SFE - Schottky Field Emitter

SHI – Swift Heavy Ion

SiC - Silicon Carbide

SRIM - Stopping and Range of Ions in Matter

TEM – Transmission electron microscopy

TFE - Thermal Field Emitter

TRISO – Tri-structural Isotropic

UO_2 – Uranium dioxide

UP – University of Pretoria

TABLE OF CONTENTS

TABLE OF FIGURES.

LIST OF TABLES.

CHAPTER 1
INTRODUCTION

1.1 High Temperature Gas-cooled Reactors (HTGR)

High-temperature gas-cooled reactors (HTGRs) are part of Generation IV reactors which are being considered for generating electricity. These reactors operate at temperatures of up to 1000 °C. Safety in these reactors is one of the most significant considerations. The Pebble Bed Modular Reactor (PBMR) is a relatively new design in nuclear power plants which has been proposed as the HTGR design for South Africa and China [Mal08]. Apart from the PBMR, there are several designs of HTGRs pursued by researchers in different countries such as the USA, Russia, Japan, The Netherlands, etc.

A key feature of the PBMR is the fuel used in the reactor, the so-called Tri-Isotropic (TRISO) fuel particles, see Figure 1.1 [Ber10, Mal08 and www1]. This particle consists of a small spherical UO_2 kernel of approximately 0.5 mm diameter, which is encapsulated by four chemical vapour deposited (CVD) layers. The first layer is a porous carbon buffer layer which is 95 μm thick. This layer reduces recoiling fission products (FPs) and accommodates internal gas buildup. The other three layers are the inner pyrolytic carbon (IPyC) layer, SiC layer and outer pyrolytic carbon (OPyC) layer. The IPyC layer with 40 μm thickness acts as a diffusion barrier to most non-metallic FPs and reduces tensile stress in SiC layer [Ber10, Han03 and Mal08]. The silicon carbide (SiC) layer of 35 μm thick acts as a main diffusion barrier to the FPs. An outer pyrolytic carbon (OPyC) layer of 40 μm thick protects SiC from external mechanical and chemical interactions and helps to reduce stress in SiC [Nic02].

For the PBMR fuel design, about 12000 of fuel particles are then imbedded in a graphite matrix to form a pebble with a diameter of about 60 mm [www1]. These pebbles are inserted from the top of the core in the reactor and circulate from the top to the bottom until they have reached optimum burn up. These particles are designed to keep the fission products (FPs) within the particle. Several studies found that the coating layers are not so effective in retaining some of the gaseous and solid fission products, e.g. Krypton (Kr), Xenon (Xe) and Silver (Ag), Cesium (Cs), Strontium (Sr) at temperatures higher than 1000 ^{o}C [www2]. These fission products are detected outside the TRISO particle. Because the temperature inside the coated fuel particle is higher than the operating temperature, the temperature range of interest for diffusion of these

FPs is from about 800°C to 1600°C, the latter being the estimated temperature during accident conditions. These FPs which escape from the TRISO particle can lead to personnel being exposed to them during maintenance of the reactor. Radioactive FPs, with the associated radioactivity, can be taken into the body by consuming foodstuff and liquids, by inhaling radioactive gases, or by absorption through wounds in the skin. Therefore, retention of the radioactive FPs within TRISO particle is important to avoid serious danger to personnel's health and the environment. Since SiC is the main FPs diffusion barrier in TRISO particle, it is important to study the mechanisms of migration behaviour of FPs in SiC.

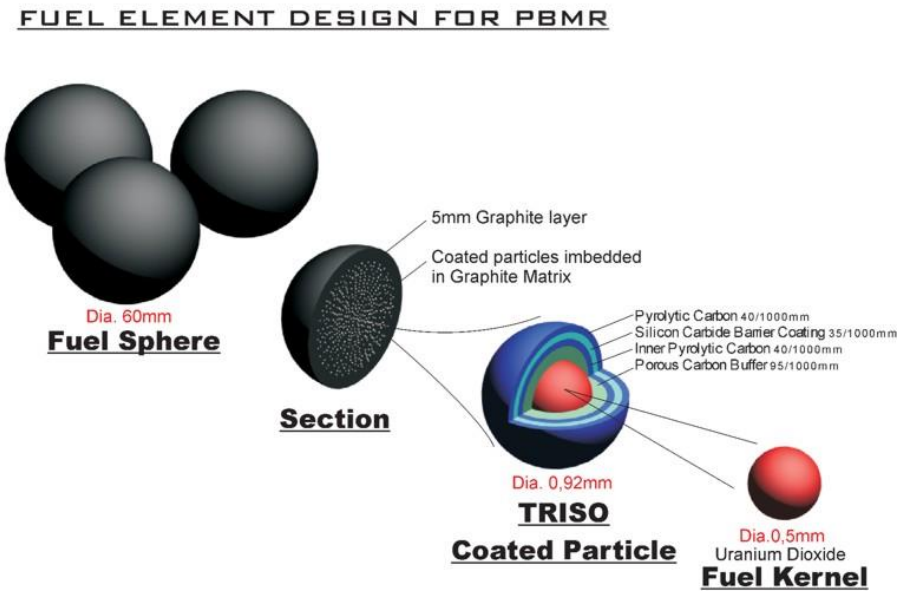

Figure 1.1: *The TRISO fuel particle for a pebble-bed reactor consists of a 0.5 mm sphere of UO_2 surrounded by a porous carbon buffer, an inner layer of isotropic pyrolytic carbon, a barrier layer of SiC, and an outer layer of isotropic pyrolytic carbon. Taken from [www1].*

1.2 Silicon Carbide

Silicon Carbide (SiC) crystal structure was understood a long time ago, but the diffusion mechanism of FPs is still a mystery. SiC has a Mohs hardness of 9.5 making it one of the hardest naturally occurring materials known. SiC has physical and chemical properties such as extreme hardness, high temperature stability, high thermal conductivity, radiation resistance, small neutron capture cross-sections, etc. [Bus03, Fuk76 and Wen98]. The hardness of SiC is due to the short bond length between Si and C atoms which is about 1.89 Å and results in high

bond strength [Dau03, Har95]. Due to its strong chemical bond energy, SiC has a good resistance against chemical attack including a high corrosion resistance. SiC has many applications in the abrasive industry due to it is properties and mechanical strength at temperatures even above 1000 °C [Pir93]. Also, SiC has the ability to maintain or keep most of its properties over a long period of time (i.e. dimensional stability), and under specific condition such as neutron radiation. SiC sublimates at temperature around 2800 °C, and also it has been noted that it starts to decompose at 1500 ˚C into Si, C, SiC_2 and Si_2C [Ber12, Lil93]. Because of its good properties, SiC is used as the main barrier for FPs in TRISO particles. The normal operating temperature of the modern HTGRs is around 950 °C [Saw00, Ver12]. According to Malherbe [Mal13], SiC should be a reliable diffusion barrier for most of the FPs during normal operating temperature.

Silicon carbide is a binary compound with the same number of silicon and carbon atoms. The basic structural unit of SiC is considered to be covalently bonded, with an ionic contribution to the bonds of about 12 %, due to the difference in electronegativity between the silicon and the carbon atom. The fundamental structural unit of SiC is a tetrahedron, either SiC_4 or CSi_4 as shown in Figure 1.2. The carbon atom can be at the centre of the tetrahedron surrounded by four silicon atoms or silicon atom at the centre of the tetrahedron surrounded by four carbon atoms.

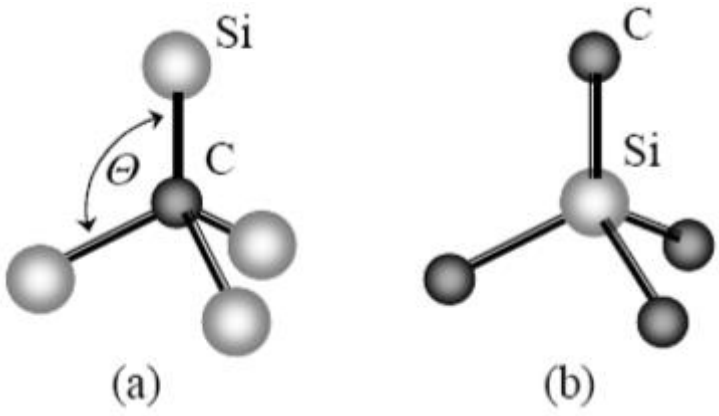

Figure 1.2: *Tetrahedral silicon carbide structure, (a) one carbon and four silicon atoms and (b) one silicon and four carbon atoms. Taken from reference [Zso05].*

The SiC compound exists in more than 200 structural forms (i.e. polytypes) [Dau03]. These different polytypes form because of the difference in the staking sequence of identical atomic planes. To describe these different polytypes in more details, the Ramsdell notation is used,

which can be explained in the following notation: The cubic (zinc blende) SiC structure is used as the basis which requires three layer, first layer is named A and second is named B and the other C (see Figure 1.3), and is known as 3C according to the nomenclature of Ramsdell [Ram47]. These three layers are placed according to a close-packed atomic plane as shown in Figure 1.3. In the Ramsdell notation, the number of layers in the stacking direction (before repeating the sequence) is combined with the letter representing the Bravais lattice type, for example, hexagonal (H), cubic (C) or rhombohedral (R) [www1]. The hexagonal and cubic polytype stacking sequence are shown in Figure 1.3. This figure shows the 2H-SiC, 3C-SiC, 4H-SiC and 6H-SiC with 3C-SiC being the cubic polytype. In this project the polycrystalline 3C- SiC wafers from Valley Design Corporation® were used.

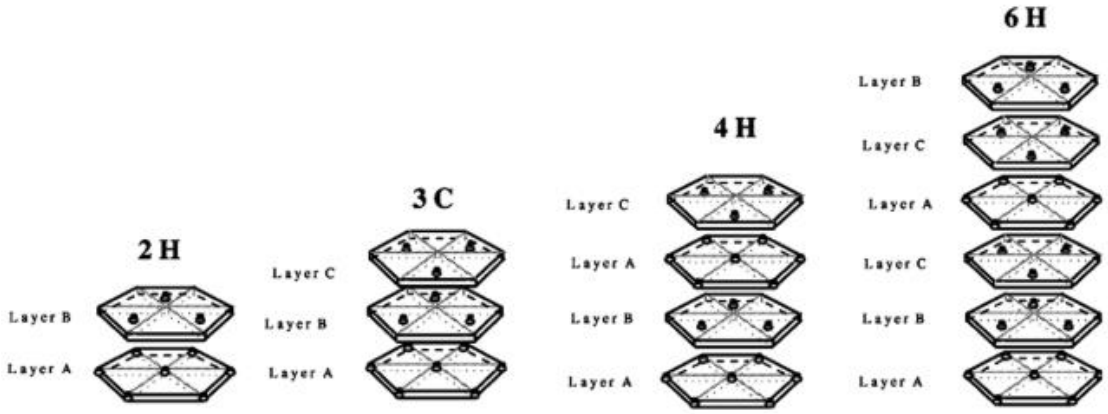

Figure 1.3: *A schematic representation showing the common SiC polytypes and their stacking sequence [Chi06].*

1.3 Radiation damage in SiC

Radiation damage in SiC has been studied widely in the last few decades. For reviews of the topic the reader is referred to [Kat06, Mal13, Sne07, Web00, Wen98 and Wes96]. Study by McHargue *et al.* [McH93] showed that SiC is easily amorphized by ion implantation of low energy ions (i.e. in the order of few hundred keV) at room temperature irrespective of the ions implanted. They also found that the accumulation of the radiation damage is approximately linear with the ions fluence until amorphization of SiC occurs. Study by Hobert *et al.* [Hob97] showed that implantation of very light ions (i.e. He^+) into SiC results in the production of strongly disturbed but still crystalline layers in SiC. Wesch *et al.* [Wes95] implanted Ga^+ ions into SiC at an energy of 230 keV with various fluences and temperatures. Their study shows that, implantation at 80 K for fluences above 1×10^{14} cm^{-2} and at 300 K for ion fluences of between 2×10^{14} cm^{-2} and 3×10^{14} cm^{-2}, results in an amorphization of SiC [Wes95]. However,

for implantation temperatures of 573 K and higher for ions fluences of about 1×10^{16} cm^{-2}, amorphization of SiC was avoided. As reported in a comprehensive review by Malherbe [Mal13] and references therein, the ion implantation at 300 °C (573 K) does not amorphize crystalline SiC although damage is introduced. In this study, 360 keV silver (Ag) and strontium (Sr) ions were implanted separately into SiC at room temperature and fluences of up to 2×10^{16} cm^{-2}.

Annealing out of the radiation damage in SiC has been reported in many publications. Most of these studies used ion beam techniques such as RBS-channeling [Fri09, Fri11, Hal10, Hal12, Hal12a, Kat06, Vis11 and Wen98] and elastic recoil detection analysis (ERDA) [Jia02, Jia07] to study the radiation damage evolution and annealing. Other analysis techniques that have also been employed to study the radiation damage evolution and annealing such as transmission electron microscopy (TEM) [Kat06, Sne98, Sne99 and Wen98], atomic force microscopy [Cap99]; scanning electron microscopy [Fri09, Fri11, Hal10, Hal12 and Hal12a]; and optical vibrational spectroscopies (IR, PL, Raman, etc.) [Hob97, Jia07, Bri09, Wen12].

McHargue *et al.* found that if the damage level is less than that necessary to produce amorphization, the damage is annealed out in the temperature range of 200 °C to 1000 °C [McH93]. However, if an amorphous SiC layer is produced, a small amount of epitaxial regrowth occurs at the amorphous/crystalline interface at temperatures below 1400°C. Audren *et al.* found that SiC is also easily amorphized by 300 keV Cs ions [Aud07]. Their studies showed that 360 keV Cs ions implanted into SiC to fluences of 6×10^{14} cm^{-2} resulted in an amorphous layer extending to a depth of approximately 150 nm below the surface. Rutherford backscattering combined with channeling (RBS/C) studies showed that the annealing of the damage in the implanted SiC started at around 600 °C, beginning from the amorphous layer and bulk substrate interface [Aud07]. Some appreciable recrystallization of amorphous SiC layer was only observed at temperatures above 960 °C, with roughly 50% of the damage annealed at approximately 1300 °C.

In this study, as mentioned above, 360 keV Ag and Sr ions were implanted separately into SiC at room temperature and fluence of 2×10^{16} cm^{-2}. Previous studies by Friedland *et al.* [Fri09, Fri12a and Fri13], have shown that implantation of 360 keV Ag ions into SiC produced an amorphous layer up to a depth of 260 nm and implantation of Sr ions at 360 keV produced amorphous layer up to 240 nm. In these studies, Ag and Sr ions of fluence 2×10^{16} cm^{-2} were implanted into SiC wafers at room temperature. A preliminary annealing for 2 h at 960 °C of a

sample implanted with Ag at room temperature resulted in very little epitaxial regrowth starting from the amorphous layer and bulk substrate interface [Fri09]. For a sample implanted with Sr, annealing of this sample at temperatures of 1000 ºC for 5 hours caused an epitaxial regrowth from the amorphous/crystalline interface, resulting in a relatively stable polycrystalline surface layer of about 180 nm thickness [Fri13]. Similar results were obtained previously by Audren *et al.* [Aud08] where iodine ion was implanted in SiC to fluence of 2.7×10^{14} cm^{-2}. An amorphous layer initially extending to a depth of 250 nm, showed some recrystallization on annealing at a temperature of 1000 °C for 30 min. The studies by Audren *et al.* [Aud08] and Fridland *et al.* [Fri09, Fri11, Fri13] suggest that the recrystallization of the amorphous SiC starts around 900 °C. Annealing temperatures ranging from 850 ˚C to approximately 900 ˚C are required to transform disordered Si-C bonds into the ordered 3C-SiC structure [Wes96]. In this study, Ag and Sr were implanted separately into polycrystalline 3C-SiC samples and then all samples were annealed under vacuum at temperatures ranging from 1100 to 1500 ˚C in steps of 100 ˚C for 5 hours. The results of the radiation damage evolution and annealing of Ag and Sr implanted SiC are presented in chapter 6.

1.4 Diffusion of silver and strontium in SiC

As mentioned in the second paragraph in section 1.1, during normal operation, TRISO particles retain most of the radiological important FPs with the exception of strontium (Sr), europium (Eu) and silver (^{110m}Ag) [www2]. ^{110m}Ag is a strong gamma emitter with a relative long half-life of about 253 days [Dem12]. Radioactive isotopes of Sr can pose important radiological health concerns if released from reactors [Pet03]. This is due to its chemical similarity to calcium, which causes it to be deposited in bones. This makes silver and strontium key FPs whose transport properties in the TRISO particle need to be investigated.

For over four decades, scientists have investigated the migration behaviour of Ag in the SiC. Extensive studies have been performed to explain the transport mechanism of Ag, including out-of-pile release measurements from irradiated TRISO fuel [Bul84, Bro76, Mer09 and Nab77], and ion implantation to investigate silver behaviour in SiC at high temperature [Fri09, Hal12, Hal12a and Mac04]. For the last 12 years, the nuclear material group of the University of Pretoria's Physics Department has been working on a systematic study of fission product elements diffusion in SiC. This has led to several publications of the work on the diffusion of silver [Fri09, Hal10, Hal12, Hes19], strontium [Fri12a, Hes19a], iodine [Fri10, Fri11], cesium

[Fri12b], and xenon [Fri14]. Studies by Friedland *et al.* [Fri09, Fri12a] showed that the diffusion of Ag and Sr in SiC is mainly due to implant induced radiation damage. There are other factors which can enhance the migration or diffusion of fission products in SiC, e.g. damage introduced into SiC by high energy fission products [Gir89, Gir90, Lev96, Lhe94].

In order to understand the transport of silver and strontium through SiC coatings, the effect of swift heavy ion irradiation (SHIs) on these FPs must be clarified (i.e. which has not been thoroughly investigated).

A fission reaction occurs (in the kernel inside the TRISO particle) when a uranium nucleus interacts with a slow neutron and adsorbs the neutron - see Figure 1.4. The uranium nucleus then becomes unstable and splits into smaller nuclei, releasing energy of about 200 MeV and two or three neutrons [Kop04]. This energy is of the same magnitude as the SHI energies of 167 MeV which was used in this study. SHI ions lose most of their energies firstly via electron excitations and later nuclear stopping. The energy loss of SHIs as they traverse through SiC layer can cause changes in the structure of SiC. The effect of the SHIs on the structure of SiC has been studied in many publications [Hal15, Hal16, Kal07, Zin00 and Zin02]. For irradiated un-implanted SiC, the phase transition and amorphous latent track formation by SHIs were not observed in SiC even up to the practical upper limit of electronic stopping power for SiC, Se = 34 keV/nm [Kal07, Zin00 and Zin02]. For the pre-implanted SiC samples (i.e. implanted and then irradiated by SHI), it was found that the SHIs caused recrystallization of an initially amorphous SiC layer [Hal15, Hal16]. These structural changes in the pre-implanted SiC samples by SHIs might influence the migration behaviour of FPs in SiC. As extensively reviewed in references [Hon11] and [Mal13], the microstructure of SiC can affect the migration behaviour of Ag or other FPs. Recently, some studies have investigated the migration behaviour of different FPs in SiC after SHI irradiation. No migration of implanted I, Kr and Xe in SiC has been detected after SHI irradiation at room temperature and at 500 ^{o}C [Aud08, Hal15 and Hal16]. The effect of carbon irradiation was studied in a post-implanted SiC with Ag ions [Len16]. Based on the literature reviewed there are no studies reported on the effect of annealing on the migration behaviour of Ag and Sr in the implanted and then SHI irradiated SiC.

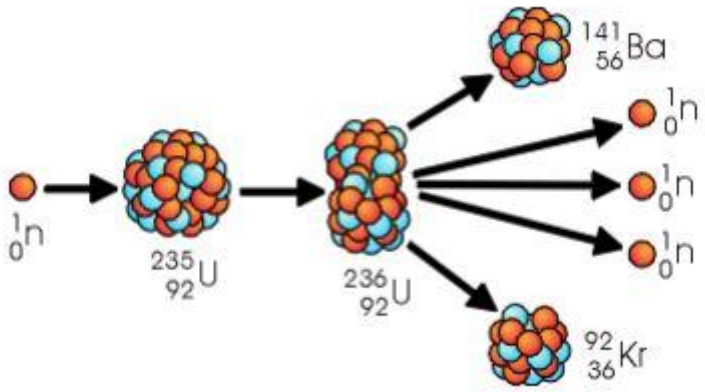

Figure 1.4: *Illustration of a uranium fission reaction. Taken from [www3].*

In this thesis the effect of ion implantation, swift heavy ion (SHI) irradiation and annealing on the structure of polycrystalline 3C-SiC and migration behaviour of Ag and Sr was investigated using Raman spectroscopy, scanning electron microscopy (SEM) and Rutherford backscattering spectrometry (RBS). For this, silver (Ag) and strontium (Sr) were implanted separately into polycrystalline 3C-SiC substrates. Some of these samples (i.e. SiC implanted by Ag and Sr) were irradiated by SHIs. All samples were then annealed under vacuum at temperatures ranging from 1100 to 1500 ˚C in steps of 100 ˚C. The results obtained are presented in chapter 6 and show that SHIs has an effect on the migration behaviour of Ag and Sr in silicon carbide.

1.5 Research Objective

The aim of this thesis was two parts. It was first to investigate structural changes in room temperature Ag and Sr implanted polycrystalline SiC after SHI irradiation at room temperature. Raman spectroscopy was used to study the microstructure of the samples (i.e. irradiated and un-irradiated but Ag or Sr implanted samples) before and after vacuum annealing at temperatures between 1100 and 1500 °C. Scanning electron microscopy was used to determine morphological changes after these treatments. Although the migration of silver (as well as strontium) in SiC has been thoroughly investigated over several decades, there have been very few ones on the effect of SHI on this migration. It is known that SHI irradiation affects the microstructure of the substrate [Gir89, Gir90, Hal15, Hal16, Lev96, Lhe94]. The microstructure of the substrate can again affect the diffusion behaviour. Consequently, the thesis also qualitatively investigates the migration behaviour of Ag and Sr in SHI irradiated and un-irradiated samples. For this purpose Rutherford backscattering spectrometry was used.

1.6 Outlay of this Thesis

Chapters in this thesis are organized as follows: Chapter 2 discusses diffusion theory, Chapter 3 ion implantation, Chapter 4 analytical techniques used in this thesis, Chapter 5 experimental procedures in details, Chapter 6 presents and discusses the results of this study, Chapter 7 summarizes the findings and conclusion and Chapter 8 is a summary of research outputs from this work.

1.7 References

[Aud07] A. Audren, A. Benyagoub, L. Thome and F. Garrido, Ion implantation of Cs into silicon carbide: Damage production and diffusion behavior. Nucl. Instr. Methods. Phys. Res. B 257 (2007) 227 - 230.

[Aud08] A. Audren, A. Benyagoub, L. Thome and F. Garrido, Ion implantation of iodine into silicon carbide: influence of temperature on the produced damage and on the diffusion behavior. Nucl. Instr. Methods. Phys. Res. B 266 (2008) 2810–2813.

[Ber10] N. G. van der Berg, J. B. Malherbe, A. J. Botha and E. Friedland, SEM analysis of the microstructure of the layers in triple-coated isotropic (TRISO) particles. Surf. Interface Anal. 42 (2010) 1156 - 1159.

[Ber12] N. G. van der Berg, J. B. Malherbe, A. J. Botha and E. Friedland, Thermal etching of SiC. Appl. Surf. Sci. 258 (2012) 5561-5566.

[Bri09] D. J. Brink, J. B. Malherbe and J. Camassel, Neutron irradiation effects in SiC. Nucl. Instr. Methods. Phys. Res. B 267 (2009) 2716 - 2718.

[Bro76] P. E. Brown and R. L. Faircloth, Metal fission product behavior in high temperature reactors - UO_2 coated particle fuel. J. Nucl. Mater. 59 (1976) 29 - 41.

[Bul84] R. E. Bullock, Fission-product release during post irradiation annealing of several types of coated fuel particles. J. Nucl. Mater. 125 (1984) 304 - 319.

[Bus03] T. Bus, A. Van Veen, A. Shiryaev, A. V. Fedorov, H. Schut, F. D. Tichelaar, and J. Sietsma, Thermal recovery of amorphous zones in 6H-SiC and 3C-SiC induced by low fluence 420 keV Xe irradiation. Mater. Sci. Eng. B. 102 (2003) 269 – 276.

[Cap99] M. Capano, S. Ryu, J. A. Cooper, M.R. Melloch, K. Rottner, S. Karlsson, N. Nordell, A. Powell, and D.E. Walker, Surface roughening in ion implanted 4H - silicon carbide. J. Elect. Mater. 28 (1999) 214 - 218.

[Chi06] W. Y. Ching, Y. N. Xu, P. Rulis and L. Ouyang, The electronic structure and spectroscopic properties of 3C, 2H, 4H, 6H, 15R and 21R polymorphs of SiC. Mater. Sci. Eng. A 422 (2006) 147- 156.

[Dau03] T. L. Daulton. T. J. Bernatowicz, R. S. Lewis, S. Messenger, F. J. Stadermann and S. Amari, Polytype distribution of circumstellar silicon carbide: microstructural characterization by transmission electron microscopy. Geochim Cosmochim Acta 67 (2003) 4743 - 4767.

[Deb12] A. Debelle, M. Backman, L. Thome, W. J. Weber, M. Toulemonde, S. Mylonas, A. Boulle, O. H. Pakarinen, N. Juslin, F. Djurabekova, K. Nordlund, F. Garrido and D. Chaussende, Combined experimental and computational study of the recrystallization

process induced by electronic interactions of swift heavy ions with silicon carbide crystals. Phys. Rev. B. 86 (2012) 100102.

[Dem12] P. Demkowicz, J. Hunn and R. Morris, Preliminary results of post- irradiation examination of the AGR-1 TRISO fuel compacts. Proceedings of the HTR Tokyo, Japan, 2012.

[Fri09] E. Friedland, J. B. Malherbe, N. G. van der Berg, T. Hlatshwayo, A. J. Botha, E. Wendler and W. Wesch, Study of silver diffusion in silicon carbide. J. Nucl. Mater. 389 (2009) 326 – 331.

[Fri10] E. Friedland, N. G. van der Berg, J. B. Malherbe, R. J. Kuhudzai, A. J. Botha, E. Wendler and W. Wesch, Study of iodine diffusion in silicon carbide. Nucl. Instr. Methods. Phys. Res. B 268 (2010) 2892-2896.

[Fri11] E. Friedland, N. G. van der Berg, J. B. Malherbe, J. J. Hancke, J. R. N. Barry, E. Wendler and W. Wesch, Investigation of silver and iodine transport through silicon carbide layers prepared for nuclear fuel element cladding. J. Nucl. Mater. 410 (2011) 24 - 31.

[Fri12a] E. Friedland, N.G. van der Berg, J.B. Malherbe, E. Wendler and W. Wesch, Influence of radiation damage on strontium and iodine diffusion in silicon carbide. J. Nucl. Mater. 425 (2012) 205 - 210.

[Fri12b] E. Friedland, N. van der Berg, T. Hlatshwayo, R. Kuhudzai, J. Malherbe, E. Wendler and W. Wesch, Diffusion behavior of cesium in silicon carbide at T > 1000 °C. Nucl. Instr. Methods. Phys. Res. B 286 (2012) 102 - 107.

[Fri13] E. Friedland, T. Hlatshwayo and N van der Berg, Influence of radiation damage on diffusion of fission products in silicon carbide. Phys. Stat. Solidi C 10 (2013) 208 - 215.

[Fri14] E. Friedland, K. Gärtner, T. T. Hlatshwayo, N. G. van der Berg and T. T. Thabethe, Influence of radiation damage on xenon diffusion in silicon carbide. Nucl. Instr. Methods. Phys. Res. B 332 (2014) 415 - 420.

[Fuk76] K. Fukuda and K. Iwamoto, Xenon diffusion behaviour in pyrolytic SiC. J. Mater. Sci. 11 (1976) 522 – 528.

[Gir89] A. I. Girka, A. Yu. Didik, A. D. Mokrushin, E. N. Mokhov, S. V. Svirida, A. V. Shishkin and V. G. Shmarovoz, Clustering vacancies during thermal annealing of SiC irradiated by hard ions. Sov. Techn. Phys. Lett. 15 (1989) 24-27.

[Gir90] A. I. Girka, A. D. Mokrushin, E. N. Mokhov, V. M. Osadchiev, S. V. Scirida and A V. Shishkin, Positron diagnostics of phase transitions in a system formed by SiC, nitrogen, and vacancy defects. Zh. Eksp. Teor. Fiz. 97 (1990) 578-590.

[Hal10] T. T. Hlatshwayo, Diffusion of silver in 6H-SiC. PhD thesis, University of Pretoria. (2010).

[Hal12] T. T. Hlatshwayo, J. B. Malherbe, N. G. van der Berg, L. C. Prinsloo, A. J. Botha, E. Wendler and W. Wesch, Annealing of silver implanted 6H–SiC and the diffusion of the silver. Nucl. Instr. Methods. Phys. Res. B 274 (2012) 120 – 125.

[Hal12a] T. T. Hlatshwayo, J.B. Malherbe, N.G. van der Berg, A.J. Botha and P. Chakraborty, Effect of thermal annealing and neutron irradiation in 6H-SiC implanted with silver at 350° C and 600° C. Nucl. Instr. Methods. Phys. Res. B 273 (2012) 61 – 64.

[Hal15] T. T. Hlatshwayo, J. H. O'Connell, V.A. Skuratov, M. Msimanga, R. J. Kuhudzai, E.G. Njoroge and J.B. Malherbe, Effect of Xe ion (167 MeV) irradiation on polycrystalline SiC implanted with Kr and Xe at room temperature. J. Phys. D Appl. Phys. 48 (2015) 465306.

[Hal16] T. T. Hlatshwayo, J. H. O'Connell, V. A. Skuratov, E. Wendler, E. G. Njoroge, M. Mlambo and J. B. Malherbe, Comparative study of the effect of swift heavy ion irradiation at 500 ^{o}C and annealing at 500 ^{o}C on implanted silicon carbide. RSC Adv. 6 (2016) 68593 - 68598.

[Han03] D. Hanson, A review of radionuclide release from HTGR cores during normal operation. EPRI, Palo Alto, CA (2003) 1009382.

[Har95] G. L. Harris, Introduction, in G.L. Harris (ed.), Properties of Silicon Carbide. Inspec. IEEE Exeter (1995).

[Hes19] H. A. A. Abdelbagi, V. A. Skuratov, S. V. Motloung, E. G. Njoroge, M. Mlambo, J. B. Malherbe, J. H. O'Connell and T. T. Hlatshwayo, Effect of swift heavy ions irradiation in the migration of silver implanted into polycrystalline SiC. Nucl. Instr. Methods Phys. Res. B 461 (2019) 201-209.

[Hes19a] H. A. A. Abdelbagi, V. A. Skuratov, S. V. Motloung, E. G. Njoroge, M. Mlambo, T. T. Hlatshwayo and J. B. Malherbe, Effect of swift heavy ions irradiation on the migration behavior of strontium implanted into polycrystalline SiC. Nucl. Instr. Methods. Phys. Res. B 451 (2019) 113-121.

[Hob97] H. Hobert, H. Dunken, F. Seifert, R. Menzel, T. Bachmann and W. Wesch, He^{+} beam induced damage of silicon carbide studied by vibrational spectroscopy. Nucl. Instr. Methods. Phys. Res. B 129 (1997) 244 - 249.

[Hon11] E. L. Honorato, H. Zhang, D. Yang and P. Xiao, Silver diffusion in silicon carbide coatings. J. Am. Ceram. Soc. 94 (2011) 3064 – 3071.

[Jia02] W. Jiang, W. J. Weber, C. M. Wang and Y. Zhang, Disordering behavior and helium

diffusion in He^+ irradiated 6H–SiC. J. Mater. Res. 17 (2002) 271 - 274.

[Jia07] W. Jiang, Y. Zhang, M. H. Engelhard, W. J. Weber, G. J. Exarhos, J. Lian and R. C. Ewing, Behavior of Si and C atoms in ion amorphized SiC. J. Appl. Phys. 101 (2007) 023524.

[Kal07] E. V. Kalinina, V. A. Skuratov, A. A. Sitnikova, E. V. Kolesnikova, A. S. Tregubova and M. P. Scheglov, Structural peculiarities of 4H-SiC irradiated by Bi ions. Semiconductors 41 (2007) 376 – 380.

[Kat06] Y. Katoh, N. Hashimoto, S. Kondo, L. Snead and A. Kohyama, Microstructural development in cubic silicon carbide during irradiation at elevated temperatures. J. Nucl. Mater. 351 (2006) 228 - 240.

[Kop04] V. I. Kopeikin, L. A. Mikaelyan and V. V. Sinev, Reactor as a source of antineutrinos: Thermal fission energy. Phys. Atom. Nucl. 67 (2004) 1892–1899.

[Len16] B. Leng, H. Ko, T. J. Gerczak, J. Deng, A. J. Giordani, J. L. Hunter, D. Morgan, I. Szlufarska and K. Sridharan, Effect of carbon ion irradiation on Ag diffusion in SiC. J. Nucl. Mater. 471 (2016) 220-232.

[Lev96] M. Levalois, I. Lhermitte-Sebire, P. Marie, E. Paumier, J. Vicens, Optical and electrical properties of 6H α-SiC irradiated by swift Xe ions. Nucl. Instr. Methods. Phys. Res. B 107 (1996) 239-241.

[Lhe94] I. Lhermitte-Sebire, J. Vicens, J. L. Chermant, M. Levalois and E. Paumier, Transmission electron microscopy and high-resolution electron microscopy studies of structural defects induced in 6H α-SiC single crystals irradiated by swift Xe ions. Phil. Mag. A 69 (1994) 237 - 253.

[Lil93] S. Lilov, Study of the equilibrium processes in the gas phase during silicon carbide sublimation. Mat. Sci. Eng. B 21 (1993) 65- 69.

[Mac04] H. J. MacLean, R. G. Ballinger, Silver ion implantation and annealing in CVD silicon carbide: the effect of temperature on silver migration. Second Topical Meeting on High Temperature Reactors 2004 (HTR-2004), Beijing, China, (2004) 22 - 24.

[Mal08] J. B. Malherbe, E. Friedland and N. G. van der Berg, Ion beam analysis of materials in the PBMR reactor. Nucl. Instr. Methods. Phys. Res. B 266 (2008) 1373- 1377.

[Mal13] J.B. Malherbe, Topical Review: Diffusion of fission products and radiation damage in SiC, J. Phys. D Appl. Phys. 46 (2013) 473001.

[McH93] C. McHargue and J. Williams, Ion implantation effects in silicon carbide. Nucl. Instr. Methods. Phys. Res. B 80 (1993) 889 - 894.

[Mer09] J. J. van der Merwe, Evaluation of silver transport through SiC during the German HTR fuel program. J. Nucl. Mater. 395 (2009) 99-111.

[Nab77] H. Nabielek, P. E. Brown and P. Offermann, Silver release from coated particle fuel. Nucl. Technol. 35 (1977) 483 - 493.

[Nic02] H. Nickel, H. Nabielek, G. Pott and A.W. Mehner, Long time experience with the development of HTR fuel elements in Germany. Nucl. Eng. Des. 217 (2002) 141- 151.

[Pet03] D. Petti, J. Buongiorno, J. Maki, R. Hobbins and G. Miller, Key differences in the fabrication, irradiation and high temperature accident testing of US and German TRISO-coated particle fuel, and their implications on fuel performance. Nucl. Eng. Des. 222 (2003) 281-297.

[Pir93] P. Pirouz and J. W. Yang, Polytypic transformations in SiC: the role of TEM. Ultramicroscopy. 51 (1993) 189 - 214.

[Ram47] R. S. Ramsdell, Studies on silicon carbide. Am. Min. 32 (1947) 64 - 82.

[Saw00] K. Sawa, S. Ueta and T. Iyoku, Research and development program of HTGR fuel in Japan. Nuclear science and engineering department, Japan atomic energy agency, Japan (2000) 208.

[Sne07] L. L. Snead, T. Nozawa, Y. Katoh, T. Byun, S. Kondo and D.A. Petti, Handbook of SiC properties for fuel performance modeling. J. Nucl. Mater. 371 (2007) 329 - 377.

[Sne98] L. L. Snead, S. J. Zinkle, J. C. Hay and M. C. Osborne, Amorphization of SiC under ion and neutron irradiation. Nucl. Instr. Methods. Phys. Res. B 141 (1998) 123 - 132.

[Sne99] L. L. Snead and J. C. Hay, Neutron irradiation induced amorphization of silicon carbide. J. Nucl. Mater. 273 (1999) 213 - 220.

[Ver12] K. Verfondern, HTGR fuel overview. IEK-6, Research center Jülich, Germany IAEA training course on HTGR technology, Beijin, China, 22-26 October (2012) Slide. 10.

[Vis11] E. Viswanathan, Y. S. Katharria, S. Selvakumar, A. Arulchakkaravarthi, D. Kanjilal and K. Sivaji, Investigations on the structural and optical properties of the swift heavy ion irradiated 6H-SiC. Nucl. Instr. Methods. Phys. Res. B 269 (2011) 1103 - 1107.

[Web00] W. J. Weber, Models and mechanisms of irradiation-induced amorphization in ceramics. Nucl. Instr. Methods. Phys. Res. B 166 (2000) 98 - 106.

[Wen12] E. Wendler, Th. Bierschenk, F. Felgenträger, J. Sommerfeld, W. Wesch, D. Alber, G. Bukalis, L. C. Prinsloo, N. Van der Berg, E. Friedland and J. B. Malherbe, Damage formation and optical absorption in neutron irradiated SiC. Nucl. Instr. Methods. Phys. Res. B 286 (2012) 97 - 101.

[Wen98] E. Wendler, A. Heft, and W. Wesch, Ion-beam induced damage and annealing behaviour in SiC. Nucl. Instr. Methods. Phys. Res. B 141 (1998) 105 – 117.

[Wes95] W. Wesch, A. Heft, E. Wendler, T. Bachmann and E. Glaser, High temperature ion implantation of silicon carbide. Nucl. Instr. Methods. Phys. Res. B 96 (1995) 335 - 338.

[Wes96] W. Wesch, Silicon carbide: synthesis and processing. Nucl. Instr. Methods. Phys. Res. B 116 (1996) 305 - 321.

[www1] http://www.pbmr.co.za. 12 December 2012.

[www2] TECDOC- 978, Fuel performance and fission product behaviour in gas-cooled reactors, Tech. rep, IAEA, Vienna, 1997. Available from: https://www.iaea.org/publications/5633/fuel-performance-and-fission-product-behaviour-in-gas-cooled-reactors.

[www3] Classroom Physics Demos. *MouseTrap Reactor*. [online] Available at: http://demos.smu.ca/index.php/demos/modern/30-mousetrap-reactor [Accessed 27 October 2015].

[Zin00] S. J. Zinkle, J. W. Jones and V. A. Skuratov, Microstructure of swift heavy ion irradiated SiC, Si_3N_4 and AlN. Materials Research Society Symposium. 650 (2000) 136–142.

[Zin02] S. J. Zinkle, V. A. Skuratov and D. T. Hoelzer, On the conflicting roles of ionizing radiation in ceramics. Nucl. Instr. Methods. Phys. Res. B 191 (2002) 758 - 766.

[Zso05] Z. Zolanim, Irradiation- induced crystal defects in silicon carbide. PhD thesis, BUTE-DAP, Department of atomic Physics (2005).

CHAPTER 2
DIFFUSION

The atoms in a crystal lattice oscillates about a fix position, which is usually its lattice site. The atom can change its lattice position if its possess enough potential energy to overcome the barrier between its initial position and the final position. The phenomenon of material transport by atomic motion from a region of high concentration to a region of low concentration is known as diffusion [Cra75]. A net flux results when there are more atoms that are randomly moving from a region of higher concentration to a region of lower concentration. Therefore, the diffusion transport is strongly dependent on the concentration gradient of the material.

2.1 The Diffusion coefficient

Fick's first law [Fic55] states that the flux (J) of diffusing particles is in such a way as to reduce the particles number density (i.e. concentration) (C); that is, the particles move from a region of higher concentration to a region of lower concentration – see Figure (2.1). The particles can be atoms, molecules, or ions. Fick's first law is also known as steady state diffusion and can be expressed in one dimension as

$$J = -D\frac{dC(x,t)}{dx} \tag{2.1}$$

where J is the flux of particles (i.e. diffusion flux) and C number density (i.e. concentration). The negative sign in equation (2.1) indicates that diffusion is occurring in the opposite direction to the increase in concentration. Diffusion is a process which leads to an equalisation of concentration. The factor of proportionality, D, is denoted as the diffusion coefficient or as the diffusivity of the species considered.

The diffusion flux (J) is expressed in number of particles (or moles) that flow through a unit area per unit time and the concentration in number of particles per unit volume. Therefore, the diffusion coefficient D has the dimension of length^2 per time and in our measurements bears the unit [nm^2 s^{-1}].

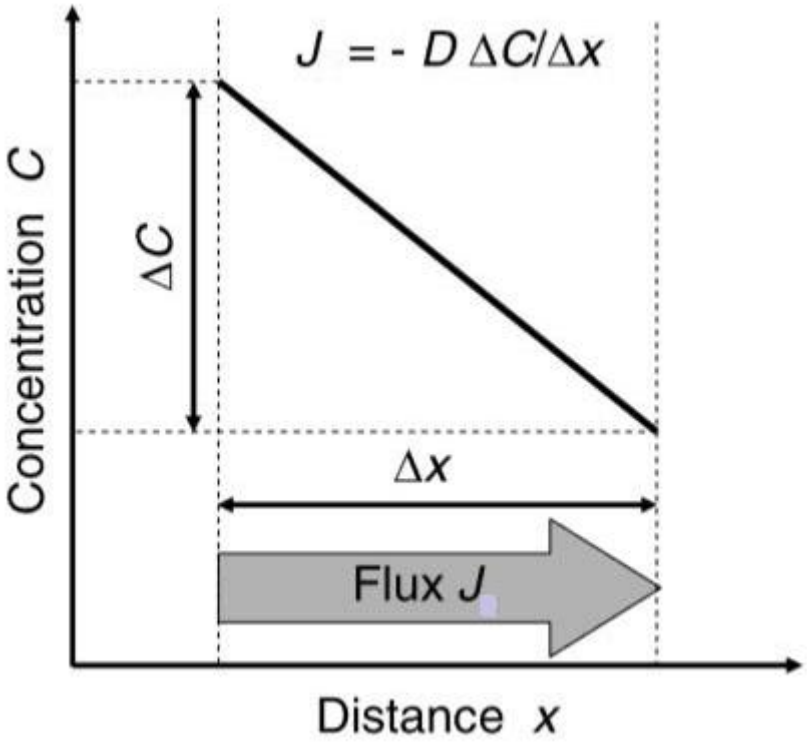

Figure 2.1: *Illustration of Fick's first law*

In most systems where diffusion occurs, the concentration changes with time, and this changes equation (2.1) and a new law is, therefore needed. The change in the concentration (C) with time is expressed by Fick's second law in equation (2.2), which is derived from the continuity equation (2.1).

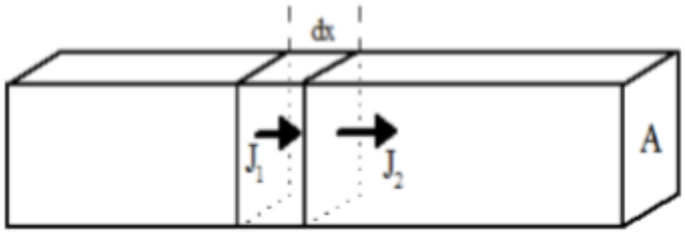

Figure 2.2: *A differential volume element in a bar of cross-sectional area A. The impurity fluxes entering and exiting the volume are denoted by J_1 and J_2 respectively. Taken from [Cam96].*

In Figure (2.2), *A* is the cross-sectional area shown as a bar. From Figure (2.2), if we take two cross-sections separated by a distance *dx*, the flux through the first cross-section J_1 will not be the same as the flux through the second cross-section ($J_1 \neq J_2$). Then

$$\frac{\partial J}{\partial x} = \frac{J_2 - J_1}{dx} \tag{2.2}$$

As $J_2 \neq J_1$, the concentration of the diffusing particles in the small volume element of the bar should change. Since the number of impurity atoms in the volume element is the product of the concentration and the differential volume element ($A.\,dx$), the continuity equation is then

$$A.\,dx\,\frac{\partial C}{\partial t} = -A(J_2 - J_1) = -A.\,dx\,\frac{\partial J}{\partial x} \tag{2.3}$$

Equation (2.3) can thus be written as

$$\frac{\partial C}{\partial t} = -\frac{\partial J}{\partial x} \tag{2.4}$$

We can substitute equation (2.1) into equation (2.4) to yield [She89]:

$$\frac{\partial C}{\partial t}\,(x,t) = \frac{\partial}{\partial x}\left(D\,\frac{\partial C}{\partial x}\right) \tag{2.5}$$

If the diffusion coefficient D is assumed to be independent of the position, then the continuity equation (i.e. Fick's second low) can be written as

$$\frac{\partial C}{\partial t}\,(x,t) = D\,\frac{\partial^2 C}{\partial x^2} \tag{2.6}$$

For an isotropic medium, in three dimensions, Fick's second law (equation 2.6) can be written as

$$\frac{\partial C}{\partial t} = D\nabla^2 C \tag{2.7}$$

In a limited temperature range the temperature dependence of diffusion coefficient (D), is given by an Arrhenius equation [Sha73]:

$$D = D_0 \exp\left[\frac{-E_a}{kT}\right] \tag{2.8}$$

where E_a is the activation energy, k is the Boltzmann constant, D_0 is the pre-exponential factor and T is the absolute temperature in units of Kelvin.

2.2 Evaluation of the diffusion coefficient

Several methods of evaluating the diffusion of impurities in different materials can be found in [Hei05 and Cra75].

In this work, as will be discussed in more detail in ion implantation in section 3.5, the implanted profile is usually very near a Gaussian function. This is due to the statistical nature of the collisions between energetic impinging ions with the substrate atoms [Mal17]. In this study, the diffusion of silver in silicon carbide after annealing at temperatures ranges from 1100 ˚C to 1300 ˚C (to be discussed in chapter 6), were found to be Fickian. To solve the diffusion coefficient D for the Fickian diffusion at the above annealed samples, Malherbe *et al.* [Mal17] derived a solution to the Fick diffusion in equation (2.5) for an original Gaussian profile with projected range R_p and range straggling ΔR_p - see equation below

$$C(\xi, 0) = A_0 \, exp\left[-\frac{(\xi - R_p)^2}{2\Delta R_p^2}\right] \tag{2.9}$$

Here, ξ is the depth below the surface. The solution for the diffusion of the implanted profile with annealing time is given by the equations (2.10) and (2.11) below

$$N(x,t) = \frac{A_0 \cdot \Delta R_p}{2\sqrt{2Dt + \Delta R_p^2}} \, e^{\left[-\frac{(x-R_p)^2}{4Dt+2\Delta R_p^2}\right]} \left[1 + erf\left(\frac{2DtR_p + x\Delta R_p^2}{\Delta R_p \sqrt{2(2Dt)^2 + 4Dt\Delta R_p^2}}\right) - ke^{\left[\frac{xR_p}{Dt+\Delta R_p^2/2}\right]} \left\{1 + erf\left(\frac{2DtR_p - x\Delta R_p^2}{\Delta R_p \sqrt{2(2Dt)^2 + 4Dt\Delta R_p^2}}\right)\right\}\right] \tag{2.10}$$

and

$$k = 1 - \left[\frac{2N_0}{A_0} \frac{\sqrt{2Dt + \Delta R_p^2}}{\Delta R_p} \, exp\left(\frac{R_p^2}{4Dt+2\Delta R_p^2}\right) \Bigg/ \left\{1 + erf\left(\frac{R_p\sqrt{Dt}}{\Delta R_p \sqrt{2Dt + \Delta R_p^2}}\right)\right\}\right] \tag{2.11}$$

There are two extreme cases for the parameter *k* in the above equation. *k*= -1 represents the case of a perfect reflecting surface, while *k*= 1 represents in the case of a perfect sink at the surface of the substrate. Because our implanted species (Ag and Sr) are deep implants in SiC and have low vapour pressure, these implanted atoms will immediately sublimate when they reach the surface of SiC. Therefore, we used *k*= 1 in this study.

To measure the diffusion coefficients at the different annealing temperatures, a software package (i.e. MATLAB program) was written in-house to fit our data and extract diffusion coefficients. As will be discussed in chapter 6 some of diffused profiles exhibited asymmetric peaks (i.e. not Gaussian). Those profiles could not be fitted to equation (2.10).

2.3 Diffusion Mechanisms

The diffusion in crystals takes place due to the presence of defects. Therefore, for diffusion to take place an atom must have enough energy to be able to break the bonds with its neighbouring atoms and move to a new site, which can be a defect or empty site. The defect structure includes point defects such as vacancies and interstitials (Frenkel-pairs) as well as planar defects (dislocation or stacking faults), complex defects (defect resulting from clustering of point or planar defect) and grain boundaries. Defect structure plays a role in the diffusion mechanism

and it is very important to understand it. Therefore, in this section the three major diffusion mechanisms namely: vacancy, interstitial and high diffusivity path mechanisms, are discussed. A discussion of the other mechanisms is given in reference [Hei05].

2.3.1 Vacancy Mechanism

The unoccupied lattice sites in a crystal are a type of point defect which is known as vacancies [Cal07], and it plays a role in the diffusion of impurities. In the vacancy mechanism [She89], the atom in a crystal will interchange its position with the neighbouring vacancy. When this happens, the atom which has moved leaves a vacancy behind. Therefore, during the movement of the atom, the vacancy seems to have also moved or jumped in the opposite direction of the atom (see Figure 2.3). In this figure, the solid circle and dotted circle represent the atom and vacancy respectively, while (a) and (b) illustrate the position before and after the diffusion.

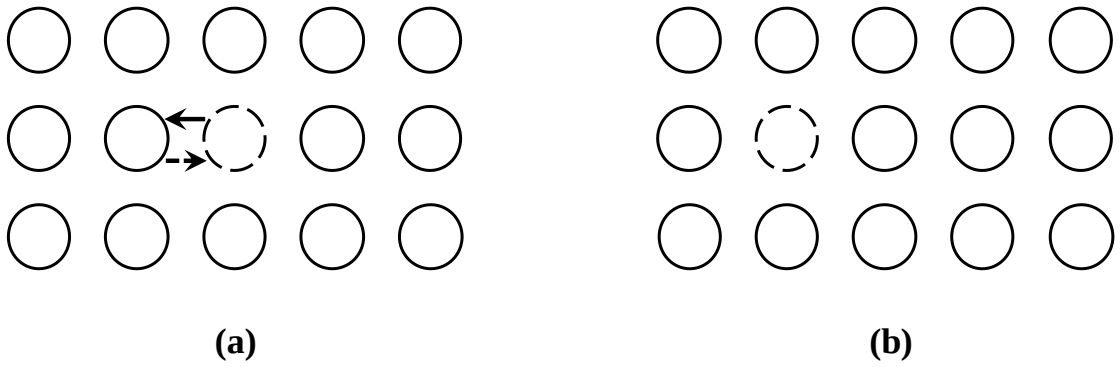

Figure 2.3: *Schematic representation of the vacancy diffusion mechanism: the dotted circle represents a vacancy, the open circles represent atoms, (a) and (b) shows the positions before and after diffusion respectively.*

2.3.2 Interstitial Mechanism

In interstitial diffusion (shown in Figure 2.4) [Cal07] an atom migrates from one interstitial to another without displacing any of the lattice atoms. An interstitial atom can be either smaller or bigger or the same size as the host atoms. In general, the interstitial diffusion is faster than the vacancy diffusion since there are many more interstitial sites than vacancy sites. And also the bonding of interstitials to the surrounding atoms is normally weaker.

A related diffusion mechanism is known as interstitialcy diffusion [Sha70, She89] and is shown in Figure 2.5. In this case, the interstitial atoms have approximately the same size as the host atoms. These interstitial atoms can move into another normal lattice site by pushing one of its nearest neighbour lattice atoms out of a lattice position into an adjacent lattice site.

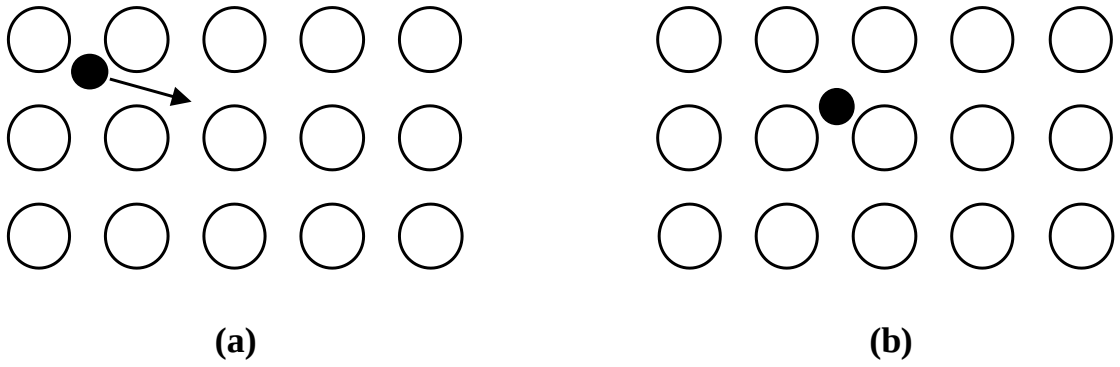

Figure 2.4: *Interstitial mechanism, (a) before and (b) after an interstitial diffusion.*

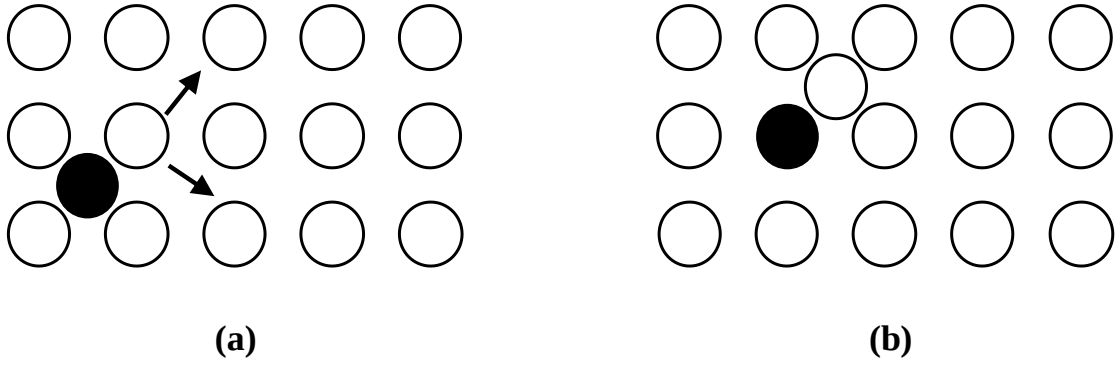

Figure 2.5: *The process of interstitialcy mechanism, (a) before and (b) after interstitialcy diffusion took place.*

2.3.3 High diffusivity paths

Vacancy, interstitial or interstitially diffusion, as discussed above, is temperature dependent. These diffusion mechanisms are known as volume diffusion. In the high diffusivity paths, the mean jump frequency of atoms at dislocations loops, grain boundaries, or surface is much higher than that of the same atom in a lattice position. Therefore, this diffusivity is higher in these mechanisms. These kinds of diffusion can take place in the polycrystalline material, similar to the material used in this study.

The diffusion in polycrystalline material is a more complex process due to the fact that these materials are composed of a large number of crystallites whose has different size, shape and composition distributions. Here, the grain boundary diffusion can rarely be decoupled from lattice or volume diffusion as the diffusion species can also leak from the boundary into the lattice and *vice versa*. Therefore, the diffusion of impurities/atoms can occur along volume, grain boundaries and surface in polycrystalline materials [Poa78].

2.4 Analysing diffusion coefficients

There are several analytical methods to determine impurity diffusion coefficients in different materials. Some of these analytical methods are discussed by Heitjans et al. and Poate et al. [Hei05, Poa78]. In this thesis, Rutherford backscattering spectrometry (RBS) was used, which is one of the ions beam analytical techniques. RBS is discussed in detail in chapter 4. In general, RBS is used in materials sciences to determine the structure and composition of materials. This done by measuring the backscattered charged particles of known incident energy (alpha particles were used in this study) from the specimen of interest.

2.5 References

[Cal07] W. D. Callister, D. G. Rethwisch, Materials science and engineering an introduction. 7th edition, John Wiley, USA. (2007) 122.

[Cam96] S. A. Campbell, The science and engineering of microelectronic fabrication. Oxford University Press, New York. (1996).

[Cra75] J. Crank, The mathematics of diffusion. Oxford University Press, Bristol, England. (1975).

[Fic55] A. Fick, Ueber Diffusion. Ann. Phys. Leipzig. 170 (1855) 59.

[Hei05] P. Heitjans, J. Karger, Diffusion in condensed matter. Springer, Netherlands. (2005).

[Mal17] J.B. Malherbe, P.A. Selyshchev, O.S. Odutemowo, C.C. Theron, E.G. Njoroge, D.F. Langa and T.T. Hlatshwayo, Diffusion of a mono-energetic implanted species with a Gaussian profile. Nucl. Instr. Methods Phys. Res. B. 406 (2017) 708-713.

[Poa78] J. M. Poate, K. N. Tu and J. W. Mayer, Thin films-interdiffusion and reactions. John Wiley, USA. (1978) 578.

[Sha70] B. L. Sharma, Diffusion in semiconductors. Trans. Tech. Publications, Clausthal-Zellerfeld Germany. (1970).

[Sha73] D. Shaw, Atomic diffusion in semiconductor. Plenum Press, London, UK. (1973).

[She89] P. Shewmon, Diffusion in solid. The Minerals, Metals and Materials Soc., USA. (1989).

CHAPTER 3
ION IMPLANTATION AND ION IRRADIATION

Ion implantation is widely used in the fabrication of semiconductor devices and in different material doping processes [Lar12]. It can be explained as the penetration of ions into the material, whereby the ions collide with the host material leading to the ions loosing of energy and eventually coming to rest inside the material. The energy is lost through inelastic and elastic collisions with the target atoms. When this technique is used, it is important to be able to predict the final distribution of the ions in the material.

Irradiation by swift heavy ions (SHIs) is slightly different from normal ion implantation, due to the difference in the energy of ions. SHIs have large energies in the range of MeV to GeV, while ion implantation energies range from 10 to 500 keV. SHIs also lose their energy via inelastic and elastic collisions with the target atoms until they come to rest inside the material. The differences between SHIs and ions implantation, the final distribution of ions within the substance, ion energy deposition and the contribution of atomic collisions (nuclear stopping) and electronic excitations (electronic stopping) which will be discussed later. The final ion distribution can only be calculated if all the processes involved until the ion comes to rest inside the material of interest are clearly understood. Hence this chapter describes the most important processes that occur during SHIs and ion implantation.

3.1 Stopping Force

The theory in this section is discussed in all the standard textbooks and review papers in the field such as [Was07 and Wi173]. The energy loss of ions within the material is the factor that affects the final distribution of ions and defects. The stopping force depends on the type and energy of ion and on the properties of the substrate material. The stopping force (S) (sometimes termed as stopping power) of a target is defined as the energy loss per unit path length at a particular depth of the particle due to its interactions with substrate atoms.

The transfer of energy from an energetic ion to the material can be divided into two independent processes, namely nuclear energy loss and electronic energy loss. The nuclear energy loss is caused by elastic collisions between the ion and nuclei of the atoms in the material/ substrate. The electronic energy loss is caused by inelastic collisions between the ion and electrons of the

target atoms. These two kinds of stopping force are described in sections 3.1.1 and 3.1.2. The stopping force (S) is equal to the sum of both nuclear stopping force (S_n) and electronic stopping force (S_e). The stopping force can be written as:

$$S = -\frac{dE}{dx} = \left[\frac{dE}{dx}\right]_n + \left[\frac{dE}{dx}\right]_e \tag{3.1}$$

where *n* and *e* represent nuclear and electronic stopping force respectively.

From the equation (3.1), the stopping cross section can be determined by dividing the total stopping force *S* by target density *N:*

$$\varepsilon = - \left[\frac{1}{N}\right]\left[\frac{dE}{dx}\right] \tag{3.2}$$

where ε is the stopping cross section.

The actual distance travelled by an ion before finally coming to rest in a target material is called the range of the ion. The mean total range of the ions (i.e. average total range of the ions) can be calculated by integrating the energy loss

$$R_T = \int_0^{E_0} \frac{dE}{S} = \int_0^{E_0} \frac{dE}{(dE/dx)_n + (dE/dx)_e} \tag{3.3}$$

where R_T is the average total range of the ions and E_0 is the incident ion energy. The range of ions will be discussed extensively in section 3.4.

In nuclear stopping force, the elastic collisions between the projectile ion and the target atoms result in a transfer of a large amount of energy and momentum of the projectile ion to the target atoms. This can cause a significant change in the ion directions within the target and displacements of target atoms from their lattice positions. As mentioned above, in the case of electronic stopping force, the slowing down of the charged ion is due to inelastic collisions between the charged ion and electrons in the material.

The stopping force depends on the type and energy of the particle/ion and on the properties of the substrate material. At low ion energies the nuclear stopping dominates, while at high ion energies the electronic stopping dominates. In electronic stopping force, the direction of the particle (i.e. ion) effectively does not change, and the path is almost completely a straight line (i.e. heavy charged particles are much more massive than electrons; therefore, such heavy ions are only slightly deflected by the electrons of the atoms). In nuclear stopping force, the

particle/ion interacts with a nucleus of the target atom and a significant deviation from the initial direction of the particle may occur. The different regimes in energy loss is shown in Figure 3.1. In Figure 3.1, the three energy regions *L*, *I* and *H* are representing the low energy region, intermediate and high energy region respectively. At low energies which are below the critical energy (E_c) (shown in Figure 3.1), nuclear stopping is the dominant stopping mechanism. At higher energies (> E_c), the electronic stopping starts to dominate and reaches a maximum then decreases at the very high energy region or Bethe-Bloch region. In the *L* region, $v_1 < v_0 Z_1^{2/3}$, in *I* region $v_1 \approx v_0 Z_1^{2/3}$ and in the *H* region $v_1 >> v_0 Z_1^{2/3}$, where v_1 and v_0 are represent the velocity of the ion and Bohr velocity respectively, and Z_1 is the atomic number of the ion. In this study, we are interested in the low and intermediate energy loss regimes as will be discussed later in section 3.1.2.

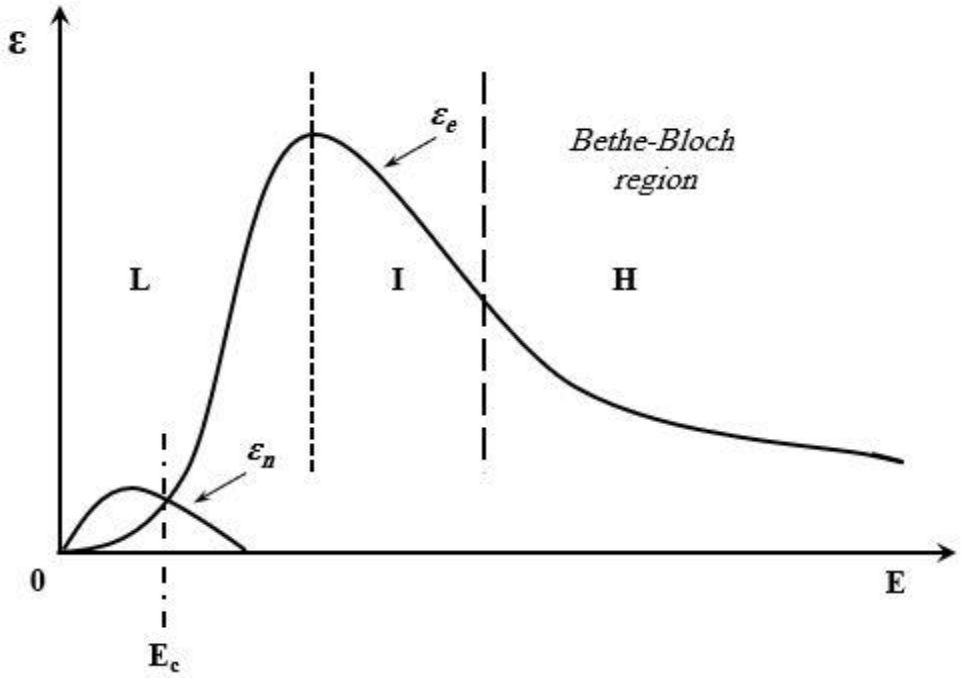

Figure 3.1: *The nuclear ε_n and electronic ε_e stopping force as a function of the ion energy E. Redrawn from reference [Was07].*

As mentioned above, the electronic stopping force reaches a maximum and decreases again at the high energy region which is described by Bethe-Bloch equation [Bet30] where the ion has a very short time to interact with the target atoms due to its high velocities.

3.1.1 Nuclear Stopping

In this energy loss mechanism, the charged particle loses its energy through a series of elastic two-body collisions with target atoms. Thus, this scattering will be described by the potential between the charged ion and target atom. In the case of head-on collision, the colliding ion will backscatter from the target atom due to the repulsion between the colliding ion and target nuclei. In this case, the interatomic potential between the two positive charges of ion and the target atom can be represented by equation (3.4) below

$$V(r) = \frac{Z_1 Z_2 e^2}{4\pi\varepsilon_0 r}\ \Phi\left[\frac{r}{a}\right] \tag{3.4}$$

where Z_1 and Z_2 are the atomic numbers of the ion and target respectively, e is the electron charge, r is the interatomic distance, ε_0 is the permittivity of free space and $\Phi\left[\frac{r}{a}\right]$ is the screening function which depends depending on the electron density distribution in the two atoms [Gna99]. The interatomic potentials for a many number of atomic pairs have been calculated using the Hartree-Fock method [Zie85].

The elastic collision between the energetic ion of mass M_1 and target atom of mass M_2 results in the transfer of kinetic energy T from the energetic ion to the target atom. This transferred energy can be calculated using equation (3.5) below. The kinetic energy (T) can be calculated from the conservation of energy and momentum. From equation (3.5), T is calculated from the atomic masses of the projectile M_1 and the target atom M_2, projectile/ion energy E_0 and scattering angle θ in the centre of mass system [Was07]. The scattering angle θ is the angle at which the incident particle/ion scatters from the target atom. The kinetic energy (T) is generally given as:

$$T = E_0 \frac{4\,M_1 M_2}{(M_1+M_2)^2} \sin^2\left(\frac{\theta}{2}\right) \tag{3.5}$$

and in the laboratory system [Tho06] as:

$$T = E_0 \frac{4\,M_1 M_2}{(M_1+M_2)^2} \cos^2\theta \tag{3.6}$$

In the laboratory system, an elastic collision between the ion and a target atom is shown in Figure 3.2. In this Figure, the elastic collision caused the deflection of M_1 and M_2 with angles relative to the M_1 original trajectory, of θ and φ, respectively.

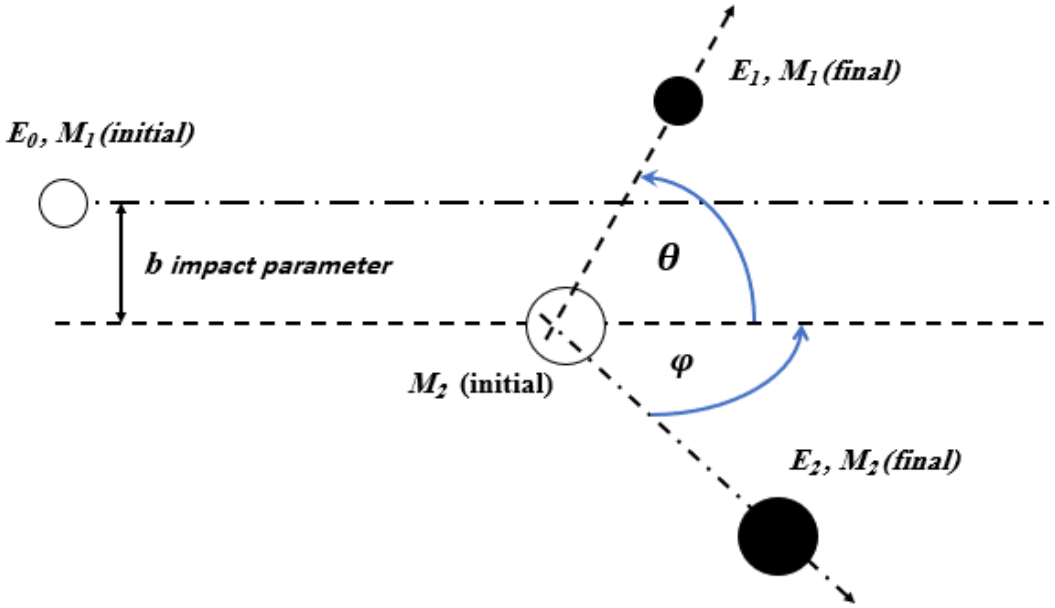

Figure 3.2: *Collision trajectory between ion M_1 of initial energy E_0 and the target atom M_2 (initial), causing M_2 to move with energy E_2 and the deflected M_1 with reduced energy E_1.*

Knowing the interatomic potential, it is possible to derive the average nuclear stopping force S_n which defines the average energy that is transferred by each nuclear collision if the particle's initial energy is E_0. S_n can be calculated by integrating the energy transfer $T(E_0, \theta)$ of a nuclear collision event over all possible impact parameters b [Zie88].

$$S_n = 2\pi \int_0^{\infty} T(E,b) b db = 2\pi \frac{4 M_1 M_2}{(M_1+M_2)^2} E_0 \int_0^{b_{max}} \sin^2\left(\frac{\theta}{2}\right) b db \qquad (3.7)$$

3.1.2 Electronic Stopping

In the electronic stopping force, the slowing down of an energetic ion when it penetrates the material is caused by the inelastic collisions between the ion and the target electrons. During this process, the energy transfer from the ion to the target electrons is more complicated compared to the nuclear stopping discussed in the above section. The processes facilitating this transfer of kinetic energy from the ion to the target electron have been investigated for many years [Zie85]. These include the excitations and ionization of target atoms and excitations, ionization or electron-capture of the incident ion. The energy loss process is usually divided into three parts based on the ion velocity with the Bohr velocity as:

$$v_0 = e^2/\hbar \qquad (3.8)$$

where v_0 is the Bohr velocity, e is the electron charge and $\hbar$ is the reduced Planck's constant, in which $\hbar$ equals $h/2\pi$. As shown in Figure 3.1, the L region deals with the low energy region, where the ion's velocity v_1 is less than $v_0 Z_1^{2/3}$. The $v_0 Z_1^{2/3}$ for silver and strontium ions is 2.8×10^9 cm/s and 2.5×10^9 cm/s respectively. At 360 keV ion energy, silver and strontium have an initial velocity of 8×10^7 cm/s and 8.9×10^7 cm/s respectively, which is less than it is $v_0 Z_1^{2/3}$. At these ion velocities, the ion cannot transfer enough energy to electrons that are much lower in energy than the Fermi level. Thus, in this region only electrons in energy levels close to the Fermi level are contributed in the inelastic energy loss process. In this low energy region, the electronic stopping has been calculated by assuming a free electron gas with a density ρ. Then, the electronic stopping S_e of a charged particle can be written [Lin54] as:

$$S_e = \int L(v,\rho)(Z_1(v))^2 \rho dV \tag{3.9}$$

where S_e is the electronic stopping, L is the stopping interaction function of the particle (ion) of a unit charge with velocity v. Z_1 is the atomic number of the incident ion, and ρ is the electron density of each volume element of the target dV.

The second region of the energy loss process deals with the so-called intermediate region, where the ion velocity v_1 is almost equal to $v_0 Z_1^{2/3}$. In the second region of the energy loss model, the particle (ion) is partly ionized and the electronic stopping reaches it maximum (Figure 3.1). For swift heavy ions irradiation, the $v_0 Z_1^{2/3}$ for xenon ions is 3.14×10^9 cm/s. At 167 MeV ion energy, xenon has an initial velocity of 1.57×10^9 cm/s, which is close to the value of $v_0 Z_1^{2/3}$.

The third region in the model (H region in Figure 3.1) is described by the Bethe-Bloch equation [Bet30] for very high velocities, where the ion velocity is now given by the condition $v_1 >> v_0 Z_1^{2/3}$. The electronic stopping in this region is proportional to Z_1^2 and is given as:

$$\varepsilon_e = \frac{4\pi Z_1^2 Z_2 e^4}{m_e v_1^2}\left[\ln\frac{2m_e v_1^2}{I} - \ln(1-\beta^2) - \beta^2 - \frac{C}{Z_2} - \frac{\delta}{2}\right] \tag{3.10}$$

where m_e is the mass of electron, v_1 the velocity of the projectile, β is the velocity of the projectile divided by the speed of light ($\beta = v/c$). C/Z_2 is the shell correction, δ is the density function due to dielectric polarization of the stopping medium at very high kinetic energies, and I is the mean excitation potential which is defined theoretically [Kam84] as:

$$\ln I = \sum_n f_n \ln(E_n - E_0) \tag{3.11}$$

where f_n is the corresponding oscillator strengths for target atoms, E_0 and E_n are the ground state and the possible energy transitions respectively. Many models have been used to estimate *I*. An approximation for *I* is given by Block's rule [Blo33]:

$$I = (10\ eV)\ Z_2 \tag{3.12}$$

In this thesis, we are interested in the low and intermediate energy loss regimes depicted in Figure 3.1. The low energy regime is for the implantation of silver and strontium of 360 keV into SiC and intermediate energy regime for the Rutherford backscattering spectrometry (RBS) which using 1.6 MeV α- particle to measure the implanted ions in the SiC. In our RBS system, the $v_0 Z_1^{2/3}$ for α- particle is 3.5×10^9 cm/s. At 1.6 MeV ion energy, α- particle has an initial velocity of 8.77×10^9 cm/s, which is close to the value of $v_0 Z_1^{2/3}$. As mentioned above, the swift heavy ion irradiation of xenon ions with 167MeV-into SiC is in the intermediate energy loss regime.

3.2 Energy loss in compounds

For the work presented in this thesis, we used SiC as a substrate for the ion implantation and SHIs irradiation. The energy loss discussed in the above sections is for a target consisting of one element. This section will discuss the energy loss behaviour in multi element targets or compounds.

The binary compound $A_m B_n$ is composed of two different elements *A* and *B*. The collisions between ions and component target are still considered to be independent encounters taking place one at a time. Therefore, the total stopping of an ion penetrating the compound can be found using a simple additive rule. This rule is known as the Bragg rule [Bra05] where the stopping cross section of element *A* and *B* are written as ε^A and ε^B respectively. So, the total stopping cross section is given by Bragg rule [Bra05] and shown in equation (3.13) below.

$$\varepsilon^{A_m B_n} = m\varepsilon^A + n\varepsilon^B \tag{3.13}$$

where *m* and *n* are the relative molar fractions of the compound consisting of elements *A* and *B*.

Deviations of the energy loss from the Bragg's rule have been found experimentally [Zie88]. This is due to the chemical and physical state of the material. Otherwise, the rule assumes that the projectile ion-target atom interaction is independent of the environment [Tes95]. Marked

deviations of the order of 10%-20% from the Bragg rule have been observed in experimental results for the stopping maximum for light organic gasses, as well as solid compounds. The deviations are especially evident when there are large differences between the atomic masses of the constituents such as in the case of oxides and nitrides of heavy metals [Zie88]. These deviations led to the development of the 'Core and Bonds' model (CAB) with respect to correcting for the chemical state of the compound [Zie88]. The compound's stopping force is estimated from the measured values of 114 organic compounds. In this model for the stopping of ions in compounds, it is assumed that two contributions are involved. These are the effects of the non-bonding core and the bonding valence electrons. To determine the CAB correction, the bond structures of the compound must be known.

3.3 Energy Straggling

An energetic ion moving through a substrate loses its energy via many interactions with the medium's atoms. The discreteness of such interactions leads to statistical fluctuations. This means, that identical energetic ions with the same initial energy when entering the medium will not have the same energy after traversing the same thickness (x) of the same medium. This phenomenon is known as straggling [Fe186].

In the electronic energy loss, the straggling is derived from the Bloch-Bethe equation [Boh48, Fe186] discussed in equation (3.10). This so-called Bohr straggling is given by:

$$\Omega_B^2 = 4\pi Z_1^2 Z_2 e^4 N x \tag{3.14}$$

where Ω_B^2 is the variance of the average energy loss of a projectile after passing a target thickness x. The distribution of the energy loss which arises from many independent collisions becomes approximately Gaussian when the energy loss is small compared to the incident energy [Fe186]. Therefore, the full width at half maximum (*FWHM*) of energy loss distribution is then given by $FWHM_B = 2\Omega_B\sqrt{2\ln 2}$, where Ω_B is the standard deviation. The Bohr theory of straggling has been extended by Lindhard *et al.* [Lin53] to include corrections for energies where the assumptions may not be valid. In a compound target, the total energy straggling is found by a linear additivity rule in a similar way to the Bragg's rule for energy loss [Chu76, Tes95].

3.4 Range and Range Straggling

The mean total distance travelled by energetic ions with initial energy E_0 from the surface of the material to the point where they stop is called the mean total range R_T. The mean total range R_T was given by equation (3.3) above.

During the energy loss processes, the statistical fluctuation of interactions and multiple scattering of an ion from the target atoms lead to zigzags in the ion's path. The phenomena of statistical fluctuation of interactions causes ions with the same initial energy to be implanted at different depths. Therefore, by taking all these factors into account, the range of an ion is given by equation (3.15) below.

$$R_i = \sum l_i \tag{3.15}$$

where R_i is the range of an ion and l_i is the length of an individual sections of the ion moving through a target medium (see Figure 3.3). The mean total range of the ions (i.e. average total range R_T) is given by

$$R_T = \frac{R_{i_1} + R_{i_2} + R_{i_3} + \cdots + R_{i_n}}{n} \tag{3.16}$$

where R_T is the mean total range of the ions, R_i is the range of an ion and n is the number of the incident ions.

Figure (3.3) shows two charged particles moving through a material, i.e. one particle with a low incident energy to simulate the implantation ion and another with high incident energy to simulate the swift heavy ion irradiation. The path of the ion with the higher incident energy in matter is nearly a straight line in the beginning due to electronic stopping, while at the end, (after loss of most of the ion's kinetic energy) the ion follows a zigzag path due to nuclear stopping. The low energy ion takes a shorter path with large deflections. The straight distance (which is perpendicular to the target surface) from the target surface to where the ion comes to rest, is referred to as the projected range R_p of the ion – see Figure 3.3. Due to scattering of the ion in its interactions with the substrate atoms, projected range (R_p) is always smaller than the range of an ion R_i. Furthermore, multiple collisions between an ion and the target atoms will cause an ion to deviate from its original path, making it to spread out. The average of all the ion ranges and ion projected ranges give the terms ion range R and projected range, R_p, for a particular substrate and ion with a specific initial energy.

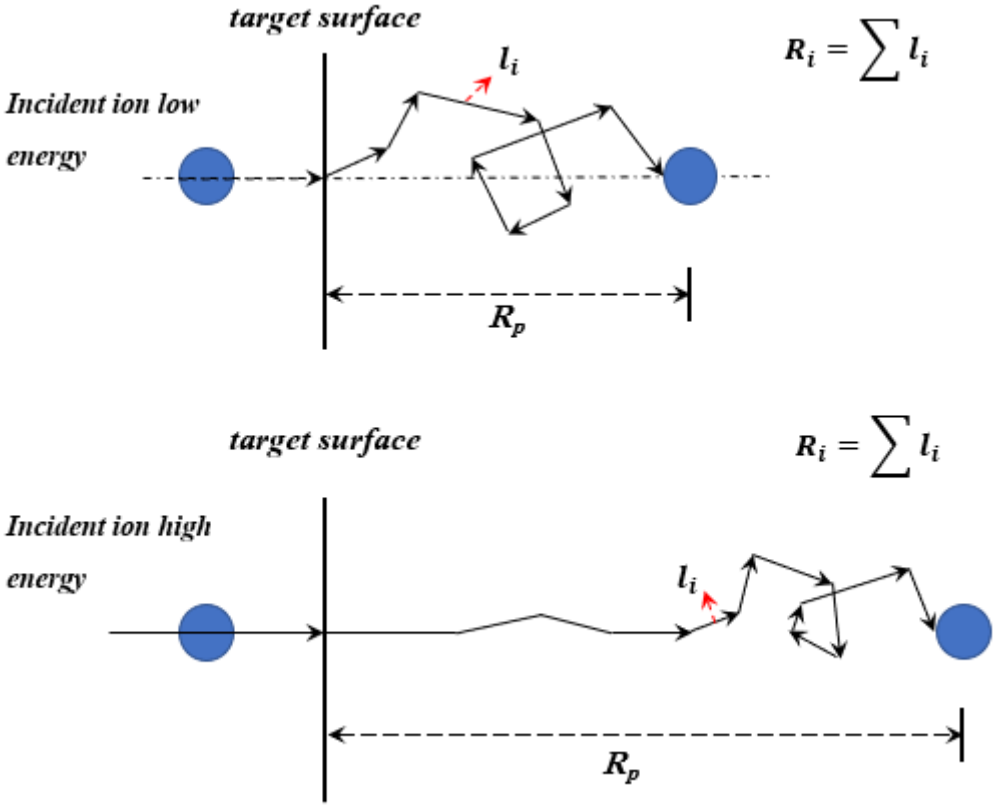

Figure 3.3: *The projected range R_p and the total range R for incident ion with low (top figure) and high (bottom figure) energy in target material.*

The implanted profile is usually very near a Gaussian, as represented in Figure 3.4, which also shows R_p, *FWHM* and ΔR_p. This is due to the statistical nature of the collisions between energetic impinging ions with the substrate atoms [Mal17]. The concentration of incident ions as a function of depth *x* is given by [Hic07]:

$$C(x) = C_P\, e^{\left[-\frac{(x-R_p)^2}{2\pi\Delta R_p^2}\right]} \tag{3.17}$$

where ΔR_p is the standard deviation of the distribution (range straggling), R_p is the projected range and C_p is the maximum concentration value/height in Gaussian ion distribution which is given by [Agu88]:

$$C_P = \frac{\emptyset}{\sqrt{2\pi N \Delta R_p}} \tag{3.18}$$

where the ion fluence is $\emptyset$ (ion/cm^2), *N* is atomic density of the substrate. The range straggling is defined by:

$$\Delta R_p = \sqrt{\frac{1}{\emptyset}\int_{-\infty}^{\infty}\left(x - R_p\right)^2 C(x)\, dx} \tag{3.19}$$

The average depth of the implanted ions is called the projected range (R_p), and can be estimated by:

$$R_p = \frac{1}{\emptyset}\int_{-\infty}^{\infty} x\, C(x)dx \tag{3.20}$$

The FWHM of the implantation profile can be calculated from the standard deviation (i.e. range straggle (ΔR_p)): $FWHM = 2\ (\Delta R_p)\sqrt{2\ln 2}$. Our strontium and silver implanted depth profiles were found to be near Gaussian- see Figure 3.4. The implanted distribution of 167 MeV Xe ions is too deep to be determined by our RBS measurement conditions (see section 3.5). The other moments in a general implantation profile such as skewness and kurtosis can be obtained by equations (3.21) and (3.22) respectively. Skewness, γ, measure the degree of asymmetry of a distribution. The skewness of a profile can has a positive value if the distribution has an asymmetric tail extending towards more positive values, and if the opposite occurs the skewness will have a negative value.

$$\gamma = \frac{\int_{-\infty}^{\infty}(x-R_p)^3\, C(x)dx}{\emptyset\ \Delta R_p^3} \tag{3.21}$$

$$\beta = \frac{\int_{-\infty}^{\infty}(x-R_p)^4\, C(x)dx}{\emptyset\ \Delta R_p^4} \tag{3.22}$$

β is the kurtosis and described as the contribution ion distribution profile tail over the flatness of the profile shape. For a perfect Gaussian profile, the skewness and kurtosis should equal to zero and 3 respectively.

Strontium and silver depth profiles are shown in Figure (3.4). The as-implanted Sr and Ag depth profiles were fitted to an Edgeworth distribution using the Genplot fitting function program to obtain the projected range (R_p), range straggling ΔR_p, skewness (γ) and kurtosis (β). The Edgeworth distribution is expressed as:

$$N(x) = Af(x)e^{\left[\frac{(x-R_p)^2}{2\Delta R_p^2}\right]} \tag{3.23}$$

$$f(x) = 1 + \frac{\gamma}{6}\left[\left(\frac{x-R_p}{\Delta R_p}\right)^3 - 3\left(\frac{x-R_p}{\Delta R_p}\right)\right] + \frac{(\beta-3)}{24}\left[\left(\frac{x-R_p}{\Delta R_p}\right)^4 - 6\left(\frac{x-R_p}{\Delta R_p}\right)^2 + 3\right] \tag{3.24}$$

For Sr profile the skewness (γ) = 0.1, kurtosis (β) = 2.93, projected range (R_p) = 146 nm and straggling (ΔR_p) = 40 nm, while for Ag profile peak the skewness (γ) = 0.4, kurtosis (β) = 2.8, projected range (R_p) =114.6 nm and straggling (ΔR_p) = 43 nm.

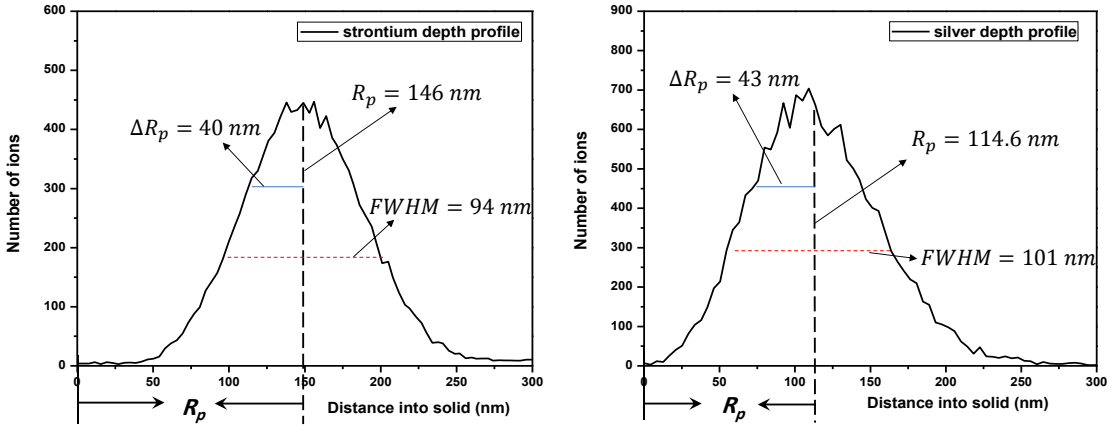

Figure 3.4: *The final distribution of implanted strontium and silver ions as function of distance in the material, which is obtained experimentally by RBS. The projected range R_p, projected range straggling ΔR_p and the full width at half maximum (FWHM) and their values are indicated in this figure. Values were obtained by fitting the as-implanted Sr and Ag spectrum depth profile with a Gaussian distribution.*

3.5 The distribution and simulation of implanted and irradiated ions

The final depth and distribution of ions in the implanted target is dependent on a large number of factors. These factors include the ion's kinetic energy, atomic number of the ion, the ion incident angle, properties of the substrate/implanted material such as atomic number and mass of atoms forming it and its microstructure [Gib75]. The crystallinity and temperature of the target and fluence of implanted ions play an important role in the final distributions of ions [Gib75].

It is important to use a Monte Carlo program to simulate the ion implantation or swift heavy ion irradiations before performing it experimentally. This program gives an idea of what to expect in the experimental results. Here, we will discuss the computer simulation performed before the implantation of strontium, silver and swift heavy ion irradiation of xenon into silicon carbide.

In this thesis, we used the SRIM software (which is based on a Monte Carlo simulation method) to calculate the interaction of ions with matter. The Stopping and Range of Ions in Matter (SRIM) [Zie13] software was developed to determine the ion range, damage ranges and distribution of the damage in the implanted material. Also, SRIM determines the angular and energy distributions of backscattered and transmitted ions in amorphous targets. As the SRIM software assumes the target to be amorphous, the calculation of SRIM software does not

considered the channelling of bombarding ions. SRIM has an error of approximately 5-10% [Zie13]. The efficiency of SRIM is achieved by the fact that the program does not take into account the structure nor dynamic composition changes in the material that is caused by the ions penetrating it. When performing the calculations, SRIM assumes the following:

- Binary collisions *i.e.* ignoring the influence of neighbouring atoms.
- Recombination of atoms with vacancies is also neglected;
- The electronic stopping force is an averaged fit from a large number of experimental stopping force data of various elements;
- The interatomic potential used in nuclear stopping has a universal form which is an averaging fit to quantum mechanical calculations from the experimental data;
- This program considers the target as an amorphous material.

Figure 3.5 shows the SRIM [Zie13] results of 360 keV strontium (Sr) and of 360 keV silver (Ag) implanted in SiC. The experimental results of Sr and Ag depth profiles from RBS (the red profiles) are included for comparison. The estimated implantation depth distribution of Sr and Ag ions from SRIM (the black profile - see Figure 3.5) is near a Gaussian distribution with projected range (R_p) of 138 nm and 109 nm for Sr and Ag respectively. The bottom of Figure 3.5 showing the energy loss profiles (i.e. electronic and nuclear energy loss) of Sr and Ag ions implanted separately into SiC. The electronic energy loss is higher at the surface but reduces as it enters deeper into the target, while nuclear energy loss increases. As mentioned above, this due to the fact that the ion energy decreases as it penetrates deeper into the target, resulting in increased nuclear energy loss. Table 3.1 below showing the experimental R_p, ΔR_p, γ and β values of Sr and Ag implanted separately into SiC at room temperature with SRIM obtained values.

Table 3.1. *The experimental R_p, ΔR_p, γ and β values of Sr and Ag implanted separately in SiC at room temperature with SRIM obtained values*

	Projected range (R_p)	**Range straggling (ΔR_p)**	**Skewness (γ)**	**Kurtosis (β)**
SRIM simulation (Sr)	138 nm	38 nm	0.03	2.79
As-implanted profile (Sr)	146 nm	40 nm	0.1	2.93
SRIM simulation (Ag)	109 nm	28 nm	0.06	2.79
As-implanted profile (Ag)	114.6 nm	43 nm	0.4	2.8

The discrepancy in the projected ranges calculated by SRIM and the one obtained from the experimental data (see Table 3.1) was about 5.5% and 4.9% for Sr and Ag respectively (the experimental R_p was larger than the one by SRIM). However, the projected ranges of Ag profiles (as well as Sr profiles) from RBS and SRIM are effectively in agreement with each other because of the experimental error (about 5-10%) for depth profile. Another important aspect follows from the values of the third and fourth moments (i.e. skewness and kurtosis) of the Ag and Sr as-implanted profiles. They show that these profiles are very near to a Gaussian profile. From equations (3.21) and (3.22), it follows that a perfect Gaussian profile the skewness $\gamma = 0$ and the kurtosis $\beta = 3$ for the Edgeworth function. The as-implanted values of $\gamma = 0.1$ and $\beta = 2.93$ for Sr profile and as-implanted values of $\gamma = 0.4$ and $\beta = 2.80$ for Ag profile are near to the ideal Gaussian profile values (i.e. $\gamma = 0$, $\beta = 3$). The Sr and Ag as-implanted profiles is nearly symmetric because a γ value between $-0.5 < \gamma < 0.5$ is generally accepted to give a fairly symmetric profile. A positive sign for γ implies that the depth profile was skewed behind R_p. The fact that the Sr and Ag as-implanted profiles are nearly Gaussian is important for this study because it means that to determine the diffusion coefficient D from annealed samples/profiles, the solution to the Fick diffusion equation for an initial Gaussian profile by Malherbe *et al.* [Mal17] can be used. From Table 3.1, there is a discrepancy between the projected range straggling calculated by SRIM and the one obtained from the experimental data. This discrepancy in the projected range straggling between our RBS results and SRIM simulation can be attributed to some assumptions made in the SRIM program (as mentioned above) such as:

- The SRIM program assumes only binary collisions and the effects of neighbouring atoms are neglected.
- The SRIM program considers the target as an amorphous material with random atom locations. Thus, the properties of the crystal lattice are ignored.
- The recombination of vacancies and interstitial atoms resulting from bombardment processes is neglected by the SRIM program.

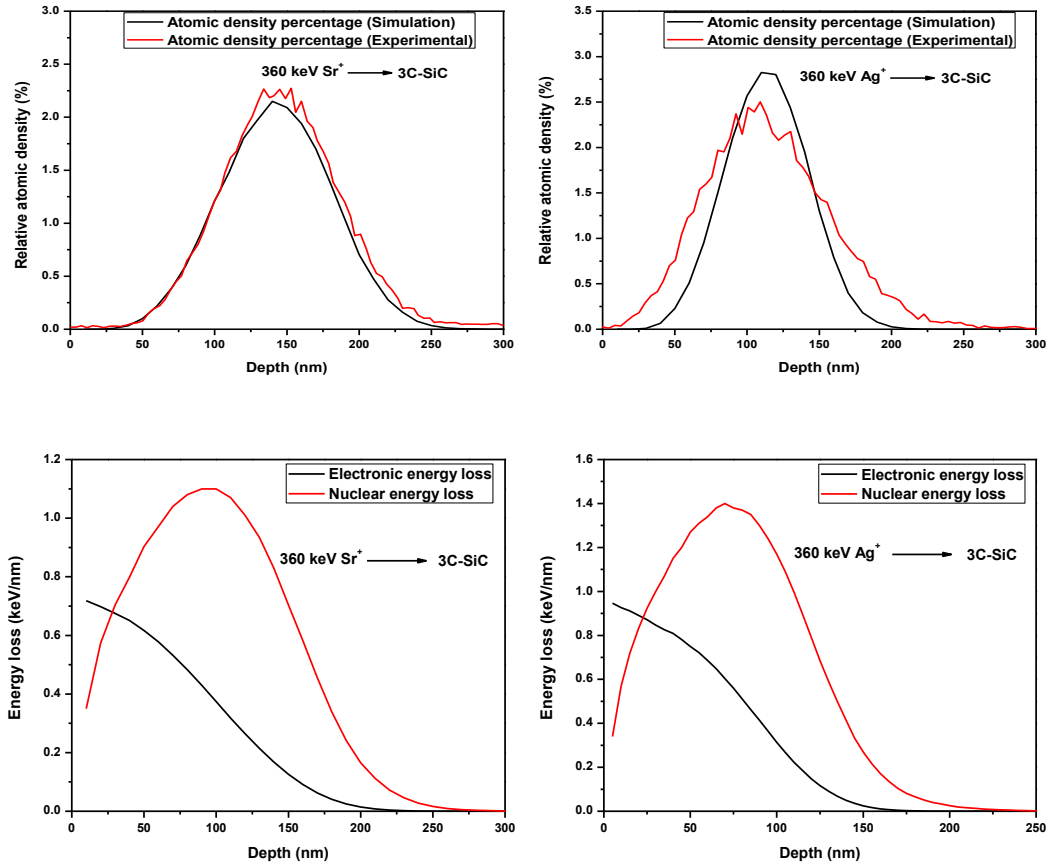

Figure 3.5: *Results of SRIM 2010 calculations for strontium (360 keV) and silver (360 keV) implanted on 3C-SiC. A typical strontium and silver depth profile (red peaks) measured by RBS is also included on the top figure. The bottom figure shows the electronic and nuclear energy loss for strontium (360 keV) and silver (360 keV) ions.*

Figure 3.6 shows the SRIM results of Xenon (Xe) ions irradiated in SiC at energy of 167 MeV. These results showed that the Xe projected range around 13 μm, which is too deep to be determined by our RBS measurement conditions. In this energy (i.e. 167 MeV), the electronic energy loss is higher at the beginning, while the nuclear energy loss increases as the ion gets deeper into the target – as shown at the bottom of Figure 3.6.

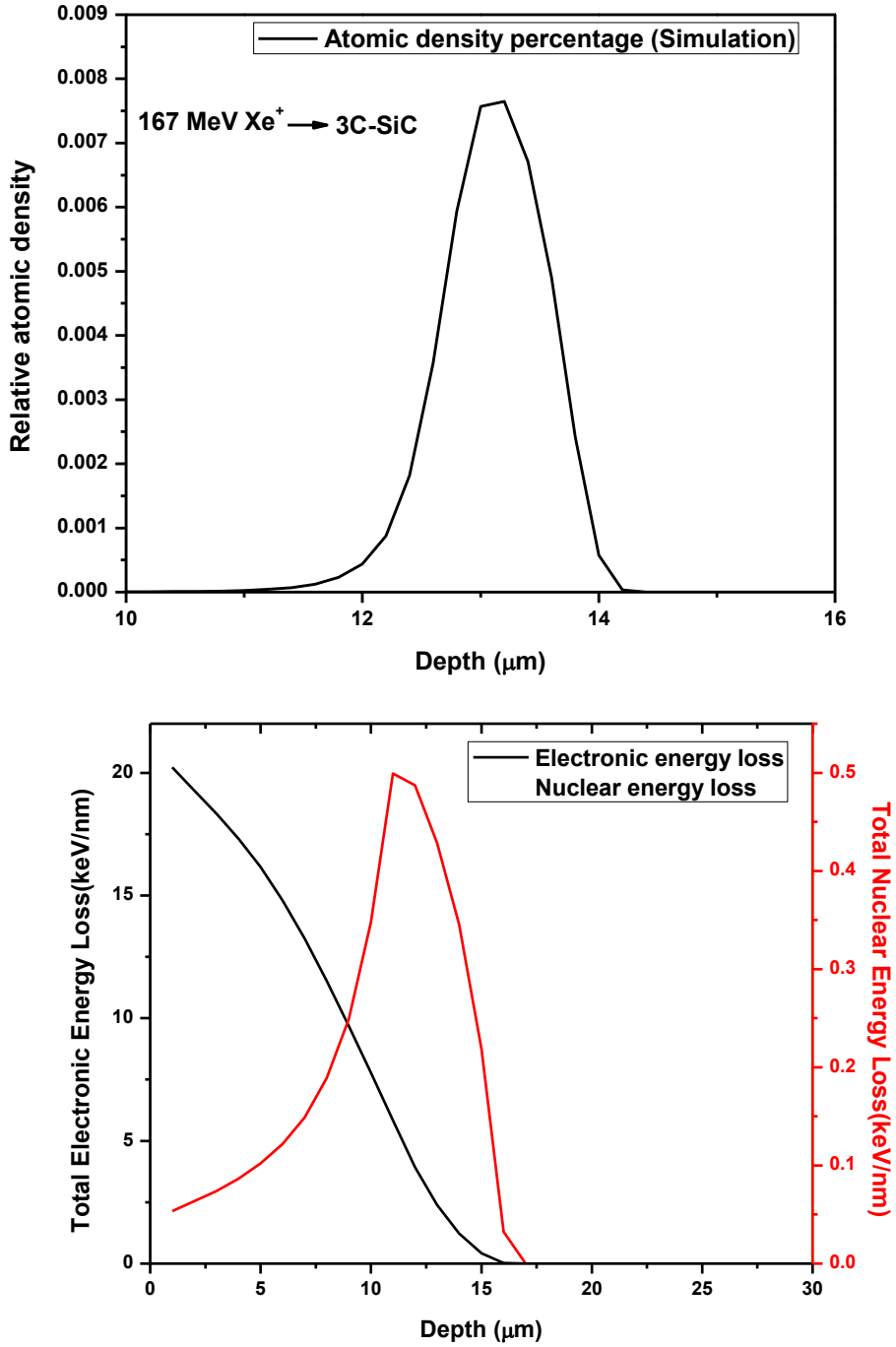

Figure 3.6: *Results of SRIM 2010 calculations for xenon (167 MeV) irradiated on 3C-SiC. The bottom figure shows the electronic and nuclear energy loss for xenon (167 MeV) ion.*

3.6 Radiation Damage

The transferred energy by an energetic ion or moving ion to the target atom result in a damaged crystal lattice. This due to the destruction of the lattice structure by ion implantation. To destruct the lattice structure in a substrate, an energetic ion should transfer sufficient energy to

the target atoms to displace them from their lattice sites. The minimum amount of energy that is required to displace a lattice atom from its original position is called displacement energy (E_d) (i.e. to create a vacancy site in the lattice of the substrate). In this study we used silicon carbide as a substrate, where the displacement energies for silicon and carbon are 35 eV and 20 eV respectively [Dev01]. The defects introduced into the crystal structure during ion implantation are known as radiation damage. In crystals the defects are categorized as point defects, planar defects, volume defects or linear defects [Nas06]. The amount of radiation damage produced during implantation depends on some factors such as type of ion, kind of target, implantation temperature and implantation fluence. If the damage is beyond a certain point in a target material, it will cause the formation of an amorphous layer. During the ion implantation a disorder is produced by each incident ion. Therefore, increasing the ion dose leads to an increase in the disorder until all atoms have been displaced and an amorphous layer (over a depth of R_p) is generated [Nas06].

Radiation damage in SiC has been studied widely in last few decades [Kat06, Mal13, Sne07, Web00, Wen98 and Wes96]. Studies by McHargue *et al.* [McH93] showed that ion implantation at room temperature easily induces amorphization in silicon carbide even at low ion energies in the order of few hundred kilo-electron-volts irrespective of the ions implanted. However, studies by Hobert *et al.* [Hob97] showed that implantation of very light ions (i.e. He^+) into SiC results in the production of strongly disturbed but still crystalline layers in SiC. At low ion implantation fluence (i.e. ion fluences $\leq 10^{13}$ ions per cm^2) the radiation damage can be limited to the formation point defects, dislocation loops, stacking faults and localized amorphous zones [Nag75]. Naguib and Kelly, [Nag75] also state that, complete amorphization can be obtained when ion fluence is in the range from 10^{13} to 10^{16} ions per cm^2. In this study, silver and strontium ions were implanted separately into SiC at room temperature to a fluence of 2×10^{16} cm^{-2}. Ag and Sr ions implantation result in amorphization of the near surface region of SiC as presented in chapter 6. It is also shown that the radiation damage (i.e. defects) play a crucial role in the transport of Ag and Sr in SiC.

Annealing out of the radiation damage in SiC have been studied widely by using several techniques such as; RBS-channelling [Fri09, Fri11, Hal10, Hal12, Hal12a, Kat06, Vis11 and Wen98], elastic recoil detection analysis (ERDA) [Jia02, Jia07], atomic force microscopy [Cap99]; scanning electron microscopy [Fri09, Fri11, Hal10, Hal12 and Hal12a]; transmission electron microscopy (TEM) [Kat06, Sne98, Sne99 and Wen98] and optical vibrational

spectroscopies (IR, PL, Raman, etc.) [Bri09, Jia07, Hob97, Wen12]. The radiation damage evolution and annealing were discussed in more details in chapter 1 and reviewed in reference [Mal13].

The effect of swift heavy ion irradiation on the crystal structure of un-implanted (i.e. virgin) and pre-implanted (i.e. implanted and then irradiated by SHI) SiC have been shown in many publications [Bac13, Ben06, Ben08, Ben09, Con14, Deb14, Hal15, Hal16, Kal07, Sku14, Sor06, Sor12, Zin00 and Zin02]. For un-implanted SiC (i.e. not initially implanted but only irradiated by SHI), the phase transition and amorphous latent track formation by SHIs were not observed in SiC even up to the practical upper limit of electronic stopping force for SiC, Se = 34 keV/nm [Kal07, Zin00 and Zin02]. Studies by Zinkle *et al.* [Zin00] suggest that the high resistance of SiC to track formation may be due to it is high thermal conductivity. Investigations on the creation of radiation damage in SiC by SHI irradiation and the annealing of radiation damage retained after implanting different low energy ions have recently been reported [Aud08, Bac13, Ben06, Ben08, Ben09, Con14, Deb14, Sku14, Sor06, Sor12]. These studies seem to agree that SHI irradiation leads to point defect production in SiC and partially restores crystallinity in heavily damaged SiC. Epitaxial regrowth of the amorphized layer from the amorphous crystalline zone (a-c) was also observed. This phenomenon is known as swift heavy ion-beam-induced epitaxial recrystallization (SHIBIEC) and occurs due to electronic energy deposition by SHIs and thermal spikes. The thermal spikes are caused when SHIs transfer their energy into the target electrons. This depends on the energy transferred i.e. electron stopping force. Studies by Hlatshwayo *et al.* [Hal15 and Hal16] showed that the recrystallization of an initially damaged and amorphous polycrystalline SiC layer resulting in randomly orientated nanocrystallites after SHIs irradiation at room temperature and at 500 ^{o}C. To explain the results the thermal spike model was proposed [Deb12]. These previous studies gave less attention to the effect of SHI irradiation on the migration of initially implanted fission products. In this study, the effect of SHI irradiation and annealing on the migration of Ag and Sr implanted separately into SiC is investigated. The results presented in chapter 6 have shown that the SHIs irradiation of the as-implanted SiC resulted in limited recrystallization (i.e. reduce the radiation damage) of the initially amorphized SiC.

3.7 References

[Agu88] F. A. Lopez, C. R. A. Catlow, P. D. Townsend, Point defects in materials. Academic press. (1988).

[Aud08] A. Audren, A. Benyagoub, L. Thome and F. Garrido, Ion implantation of iodine into silicon carbide: influence of temperature on the produced damage and on the diffusion behavior. Nucl. Instr. Methods. Phys. Res. B 266 (2008) 2810–2813.

[Bac13] M. Backman, M. Toulemonde, O. Pakarinen, N. Juslin, F. Djurabekova, K. Nordlund , A. Debelle and W. J. Weber, Molecular dynamics simulations of swift heavy ion induced defect recovery in SiC. Comput. Mater. Sci. 67 (2013) 261-256.

[Ben06] A. Benyagoub and A. Audren, Athermal crystallization induced by electronic excitations in ion irradiated silicon carbide. Appl. Phys. Lett. 89 (2006) 241914.

[Ben08] A. Benyagoub, Irradiation effects induced in silicon carbide by low and high energy ions. Nucl. Instr. Methods. Phys. Res. B 266 (2008) 2766-2771.

[Ben09] A. Benyagoub and A. Audren, Study of the damage produced in silicon carbide by high energy heavy ions. Nucl. Instr. Methods. Phys. Res. B 267 (2009) 1255-1258.

[Bet30] H. Bethe, Zur Theorie des Durchgangs schneller Korpuskularstrahlen durch Materie. Ann. Phys. Leipzig 5 (1930) 324.

[Blo33] F. Bloch, Zur Bremsung rasch bewegter Teilchen beim Durchgang durch Materie. Ann. Phys. Leipzig 16 (1933) 285.

[Boh48] N. Bohr, The penetration of atomic particles through matter. Mat. Fys. Medd. Dan. Vid. Selsk. 18 (8) (1948).

[Bon71] E. Bonderup, P. Hvelplund, Stopping power and energy straggling for swift Protons. Phys. Rev. A. 4 (1971) 562.

[Bra05] W. Bragg and R. Kleeman, XXXIX. On the α particles of radium, and their loss of range in passing through various atoms and molecules. Phil. Mag. 10 (1905) 318-340.

[Bri09] D. J. Brink, J. B. Malherbe and J. Camassel, Neutron irradiation effects in SiC. Nucl. Instr. Methods. Phys. Res. B 267 (2009) 2716 - 2718.

[Cap99] M. Capano, S. Ryu, J. A. Cooper, M.R. Melloch, K. Rottner, S. Karlsson, N. Nordell, A. Powell, and D.E. Walker, Surface roughening in ion implanted 4H - silicon carbide. J. Elect. Mater. 28 (1999) 214 - 218.

[Chu76] W. Chu, Calculation of energy straggling for protons and helium ions. Phys. Rev. A 13 (1976) 2057.

[Con14] J. H. O'Connell, V. A. Skuratov, A. S. Sohatsky and J. H. Neethling, 1.2 MeV/amu Xe ion induced damage recovery in SiC. Nucl. Instr. Methods. Phys. Res. B 326 (2014) 337-340.

[Deb12] A. Debelle, M. Backman, L. Thome, W. J. Weber, M. Toulemonde, S. Mylonas, A. Boulle, O. H. Pakarinen, N. Juslin, F. Djurabekova, K. Nordlund, F. Garrido and D. Chaussende, Combined experimental and computational study of the recrystallization process induced by electronic interactions of swift heavy ions with silicon carbide crystals. Phys. Rev. B 86 (2012) 100102.

[Deb14] A. Debelle, M. Backman, L. Thome, K. Nordlund, F. Djurabekova, W. J. Weber, I. Monnet, O. H. Pakarinen, F. Garrido and F. Paumier, Swift heavy ion induced recrystallization in cubic silicon carbide: New insights from designed experiments and MD simulations. Nucl. Instr. Methods. Phys. Res. B 326 (2014) 326-331.

[Dev01] R. Devanathan, W. Weber and F. Gao, Atomic scale simulation of defect production in irradiated 3C-SiC. J. Appl. Phys. 90 (2001) 2303.

[Fe186] L. Feldman and J. Meyer, Fundamental of surface and thin film analysis. Elsevier Science Publishing Co. New York. (1986).

[Fri09] E. Friedland, J. B. Malherbe, N. G. van der Berg, T. Hlatshwayo, A. J. Botha, E. Wendler and W. Wesch, Study of silver diffusion in silicon carbide. J. Nucl. Mater. 389 (2009) 326 – 331.

[Fri11] E. Friedland, N. G. van der Berg, J. B. Malherbe, J. J. Hancke, J. R. N. Barry, E. Wendler and W. Wesch, Investigation of silver and iodine transport through silicon carbide layers prepared for nuclear fuel element cladding. J. Nucl. Mater. 410 (2011) 24 - 31.

[Gib75] J. Gibbons, W. Johnson and S. Mylroie, Projected range statistics, semiconductors and related materials. Second Edition, Dowden, Hutchingson & Ros, Pennsylvania. (1975).

[Gna99] H. Gnaser, Low- energy ion irradiation of solid surfaces. Springer, Berlin. 146 (1999).

[Hal10] T. T. Hlatshwayo, Diffusion of silver in 6H-SiC. PhD thesis, University of Pretoria. (2010).

[Hal12] T. T. Hlatshwayo, J. B. Malherbe, N. G. van der Berg, L. C. Prinsloo, A. J. Botha, E. Wendler and W. Wesch, Annealing of silver implanted 6H–SiC and the diffusion of the silver. Nucl. Instr. Methods. Phys. Res. B 274 (2012) 120 – 125.

[Hal12a] T. T. Hlatshwayo, J.B. Malherbe, N.G. van der Berg, A.J. Botha and P. Chakraborty, Effect of thermal annealing and neutron irradiation in 6H-SiC implanted with silver at 350° C and 600° C. Nucl. Instr. Methods. Phys. Res. B 273 (2012) 61 – 64.

[Hal15] T. T. Hlatshwayo, J. H. O'Connell, V. A. Skuratov, M. Msimanga, R. J. Kuhudzai, E. G. Njoroge and J. B. Malherbe, Effect of Xe ion (167 MeV) irradiation on polycrystalline SiC implanted with Kr and Xe at room temperature. J. Phys. D Appl. Phys. 48 (2015) 465306.

[Hal16] T. T. Hlatshwayo, J. H. O'Connell, V. A. Skuratov, E. Wendler, E. G. Njoroge, M. Mlambo and J. B. Malherbe, Comparative study of the effect of swift heavy ion irradiation at 500 ^{o}C and annealing at 500 ^{o}C on implanted silicon carbide. RSC Adv. 6 (2016) 68593 - 68598.

[Hic07] D. P. Hickey, Ion implantation induced defect formation and amorphization in the Group IV semiconductors: Diamond, silicon and germanium. Available at: http://etd.fcla.edu. (2007).

[Hob97] H. Hobert, H. Dunken, F. Seifert, R. Menzel, T. Bachmann and W. Wesch, He^{+} beam induced damage of silicon carbide studied by vibrational spectroscopy. Nucl. Instr. Methods. Phys. Res. B 129 (1997) 244 - 249.

[Jia02] W. Jiang, W. J. Weber, C. M. Wang and Y. Zhang, Disordering behavior and helium diffusion in He^{+} irradiated 6H–SiC. J. Mater. Res. 17 (2002) 271 - 274.

[Jia07] W. Jiang, Y. Zhang, M. H. Engelhard, W. J. Weber, G. J. Exarhos, J. Lian and R. C. Ewing, Behavior of Si and C atoms in ion amorphized SiC. J. Appl. Phys. 101 (2007) 023524.

[Kal07] E. V. Kalinina, V. A. Skuratov, A. A. Sitnikova, E. V. Kolesnikova, A. S. Tregubova and M. P. Scheglov, Structural peculiarities of 4H-SiC irradiated by Bi ions. Semiconductors 41 (2007) 376 – 380.

[Kam84] E. Kamaratos, The mean excitation energy for stopping power I, the Bragg rule, and chemical and phase effects. Application of a statistical treatment to the determination of I for chemically bound particles. Chem. Rev. 84 (1984) 561-576.

[Kat06] Y. Katoh, N. Hashimoto, S. Kondo, L. Snead and A. Kohyama, Microstructural development in cubic silicon carbide during irradiation at elevated temperatures. J. Nucl. Mater. 351 (2006) 228 - 240.

[Lar12] L. A. Larson, J. M. Williams and M. I. Current, Ion implantation for semiconductor doping and materials modification. Rev. of Accelerator Sci. and Tech. 4 (2012) 11 - 40.

[Lin53] J. Lindhard and M. Scharff, Energy loss in matter by fast particles of low charge. Kgl.

Dan. Vid. Selsk. Mat. Fys. Medd. 27 (15) (1953) 1–32.

[Lin54] J. Lindhard, On the properties of a gas of charged particles. Kgl. Dan. Vid. Selsk. Mat. Fys. Medd. 28 (8) (1954).

[McH93] C. McHargue and J. William, Ion implantation effects in silicon carbide. Nucl. Instr. Methods. Phys. Res. B 80 (1993) 889-894.

[Mal13] J.B. Malherbe, Topical Review: Diffusion of fission products and radiation damage in SiC. J. Phys. D Appl. Phys. 46 (2013) 473001.

[Mal17] J. B. Malherbe, P. A. Selyshchev, O. S. Odutemowo, C. C. Theron, E. G. Njoroge, D. F. Langa and T. T. Hlatshwayo, Diffusion of a mono-energetic implanted species with a Gaussian profile. Nucl. Instr. Methods. Phys. Res. B 406 (2017) 708.

[Nag75] H. Nagiub, R. Kelly, Criteria for bombardment-induced structural changes in non-metallic solids. Rad. Effects. 25 (1975) 1-12.

[Nas06] M. Nastasi, J. W. Mayer, Ion Implantation and Synthesis of Materials. Springer. (2006).

[Sku14] V. A. Skuratov, J. O'Connell, A. S. Sohatsky and J. Neethling, TEM study of damage recovery in SiC by swift Xe ion irradiation. Nucl. Instr. Methods. Phys. Res. B 327 (2014) 89-92.

[Sne07] L. L. Snead, T. Nozawa, Y. Katoh, T. Byun, S. Kondo and D.A. Petti, Handbook of SiC properties for fuel performance modeling. J. Nucl. Mater. 371 (2007) 329 - 377.

[Sne98] L. L. Snead, S. J. Zinkle, J. C. Hay and M. C. Osborne, Amorphization of SiC under ion and neutron irradiation. Nucl. Instr. Methods. Phys. Res. B 141 (1998) 123 - 132.

[Sne99] L. L. Snead and J. C. Hay, Neutron irradiation induced amorphization of silicon carbide. J. Nucl. Mater. 273 (1999) 213 - 220.

[Sor06] S. Sorieul, J. Costantini, L. Gosmain, L. Thome and J. Grob, Raman spectroscopy study of heavy-ion-irradiated α-SiC. J. Phys: Condens. Matter. 18 (2006) 5235- 5251.

[Sor12] S. Sorieul, X. Kerbiriou, J. Costantini, L. Gosmain, G. Calas and C. Trautmann, Optical spectroscopy study of damage induced in 4H-SiC by swift heavy ion irradiation. J. Phys: Condens. Matter. 24 (2012) 125801.

[Tho06] J. J. Thomson, Conduction of electricity through gases. Cambridge Univ. Press, Cambridge, UK. (1906).

[Tes95] J. R. Tesmen and M. Nastasi, Handbook of modern ion beam materials analysis. MRS, Pittsburgh, USA. (1995).

[Tow06] P. D. Townsend, P. J. Chandler, L. Zhang, Optical effects of ion implantation.

Cambridge University Press, New York. (2006).

[Vis11] E. Viswanathan, Y. S. Katharria, S. Selvakumar, A. Arulchakkaravarthi, D. Kanjilal and K. Sivaji, Investigations on the structural and optical properties of the swift heavy ion irradiated 6H-SiC. Nucl. Instr. Methods. Phys. Res. B 269 (2011) 1103 - 1107.

[Was07] G. Was, Fundamentals of radiation materials science, metals and alloys. Springer, Berlin. (2007).

[Web00] W. J. Weber, Models and mechanisms of irradiation-induced amorphization in ceramics. Nucl. Instr. Methods. Phys. Res. B 166 (2000) 98 - 106.

[Wen12] E. Wendler, T. Bierschenk, F. Felgenträger, J. Sommerfeld, W. Wesch, D. Alber, G. Bukalis, L. C. Prinsloo, N. Van der Berg, E. Friedland and J. B. Malherbe, Damage formation and optical absorption in neutron irradiated SiC. Nucl. Instr. Methods. Phys. Res. B 286 (2012) 97 - 101.

[Wen98] E. Wendler, A. Heft and W. Wesch, Ion-beam induced damage and annealing behaviour in SiC. Nucl. Instr and Meth. B 141(1998) 105-117.

[Wes96] W. Wesch, Silicon carbide: synthesis and processing. Nucl. Instr. Methods. Phys. Res. B 116 (1996) 305 - 321.

[Wi173] R. Wilson and G. Brewer, Ion beams with applications to ion implantation. John Wiley and Sons Inc. New York. (1973).

[Zie85] J. Ziegler, J. Biersack, The stopping and range of ions in matter. Treatise Heavy-Ion Sci. (1985) 93–129.

[Zie88] J. Ziegler, Ion implantation science and technology. 2nd edition Academic press, New York. (1988).

[Zie13] J. F. Ziegler, www.SRIM.org, USA, 2013.

[Zin00] S. J. Zinkle, J. W. Jones and V. A. Skuratov, Microstructure of swift heavy ion irradiated SiC, Si_3N_4 and AlN. Materials Research Society Symposium. 650 (2000) 136–142.

[Zin02] S. J. Zinkle, V. A. Skuratov and D. T. Hoelzer, On the conflicting roles of ionizing radiation in ceramics. Nucl. Instr. Methods. Phys. Res. B 191 (2002) 758 - 766.

CHAPTER 4
ANALYTICAL TECHNIQUES

The effects of swift heavy ions (SHIs) irradiated in polycrystalline 3C-SiC implanted with silver and strontium were investigated. The diffusion behaviour of silver and strontium in polycrystalline 3C-SiC and the structural changes due to the SHIs irradiation were also investigated using Rutherford backscattering spectrometry (RBS), scanning electron microscopy (SEM) and Raman spectroscopy techniques. In this chapter, the analytic techniques are discussed and described in sections 4.1, 4.2 and 4.3.

4.1 Rutherford backscattering spectrometry (RBS)

Rutherford backscattering spectrometry (RBS) is an ion beam analytical technique which is usually used to quantitatively determine the components of thin layers or the near surface region of solids. This analysis involves a very simple principle where energetic ions are projected towards a target and then backscatter at a particular angle where they can be detected by specific detector. Therefore, the RBS technique is based on the analysis of the energy of the backscattered ions (helium ions (He^+) in our case) from the material of interest. In this thesis the material of interest is polycrystalline 3C- SiC with silver or strontium implanted on it.

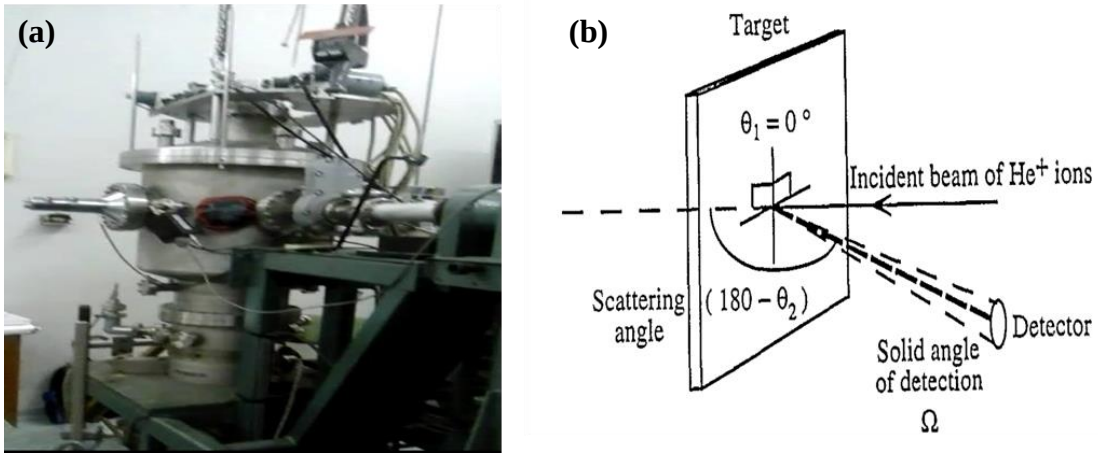

Figure 4.1: *(a) RBS equipment at the University of Pretoria, (b) Geometry of the RBS experiment [Gol96].*

4.1.1 Components of Rutherford backscattering spectrometry

Rutherford backscattering spectrometry contains three systems namely: accelerator, scattering chamber and detector system. In the accelerator, charged particles (He^+) are generated by a RF-

source and accelerated to high energies by applying a huge potential difference across the accelerator pipe. The Van de Graaff accelerator was developed in the beginning of 1929 by Van de Graaff. In this accelerator a high potential difference is built up and maintained on a smooth conducting surface. This done by the continuous transfer of positive static charges from a moving belt to the surface, see Figure 4.2 (a). The belt is made of silk or other high dielectric material. The ion source is located inside the high-voltage terminal. Ions are accelerated from the source to the target by the electric voltage between the high-voltage supply and ground [Chu78]. In this study, the Van de Graaff accelerator at the University of Pretoria was used. The energy of He^+ ions that used in this study was 1.4 MeV and 1.6 MeV. The maximum voltage of this accelerator is 2.7 MeV. Schematic diagrams of the accelerator and the scattering chamber are shown in Figure 4.2 (b) and 4.2 (c) respectively.

To deflect the ion beam into either beam line 1 or line 2 there is a dipole magnet in front of the Van de Graaff accelerator. Hence, it acts to separate a beam according to their energy and mass. The difference between line 1 and line 2 is that the line 1 it has a chamber which work below room temperature, while line 2 is working at room temperature. In this study, line 2 was used. The slits are used to focus and guide the beam into the chamber and to produce a monochromatic beam consisting of one species (i.e. helium ions) with a specific energy. Inside the chamber, there is a collimator which is used to shape the beam into a specific size before interaction with specimen, see Figure 4.2 (c). The size of the ion beams is affected by the size of collimator. The three-axis goniometer system which has a precision of 0.02^o in each of the angle settings, is connected to a stainless-steel sample holder. During the inelastic interactions between the He^+ ions and target atoms, secondary electrons are generated. These secondary electrons can falsify the measurements. They can be suppressed by applying a negative voltage of 200 V connected to a ring-shaped electrode in front of the target.

The backscattered alpha particles beam (BS. Beam) in Figure 4.2 (c), are detected by a Si surface barrier detector operating with a reverse bias of 40 V. The output charge signal of the detector is then fed into the pre-amplifier where it is integrated into a voltage signal that is proportional to the backscattered ion energy. The voltage signal is amplified by the amplifier and digitized by an analogue to digital converter (ADC) inside the multi-channel analyzer (MCA) and stored in the computer connected to the MCA. Outputs of the multi-channel analyzer consists of counts (of backscattered ions) vs. the channel number spectrum. The

number of backscattered particles at 165^{o} (for our experimental set-up) is called the yield while the channel number is proportional to the backscattered energy.

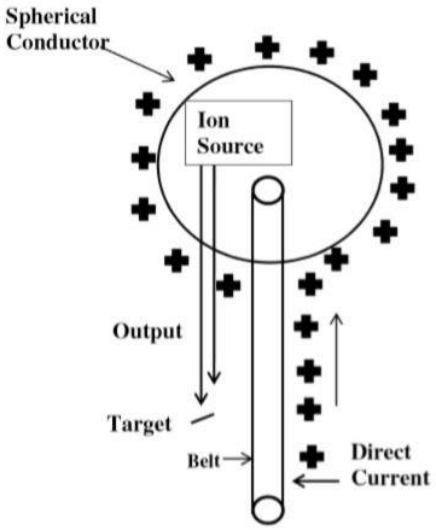

Figure 4.2 (a): *A schematic diagram of a Van de Graaff accelerator [www1].*

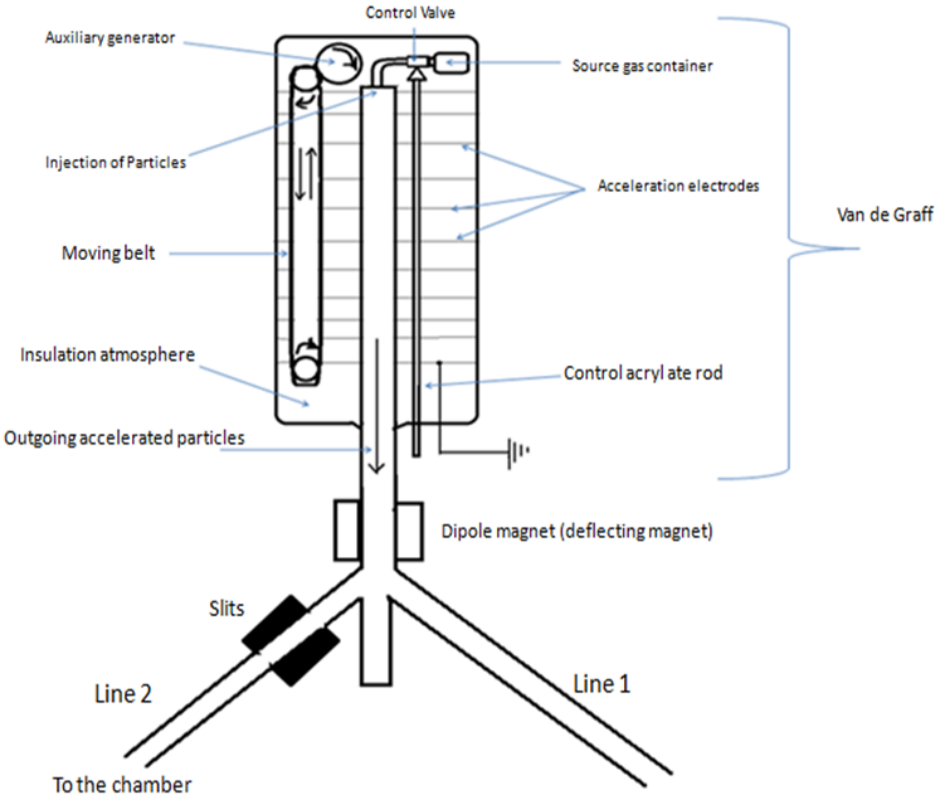

Figure 4.2 (b): *A schematic diagram showing the Van de Graaff accelerator and beam lines of the University of Pretoria.*

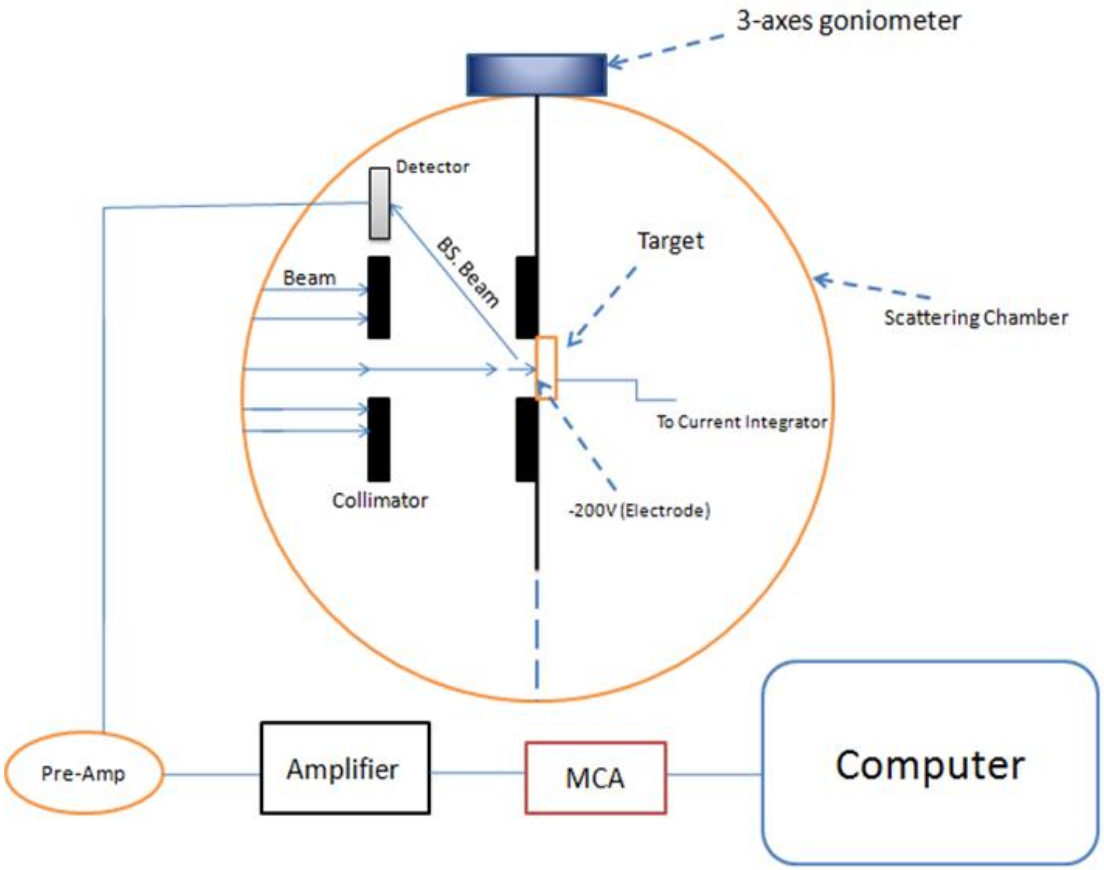

Figure 4.2 (c): *A schematic diagram showing the side view of the scattering chamber and detector system of Van de Graaff accelerator of University of Pretoria.*

4.1.2 Details of Rutherford backscattering spectrometry

Rutherford backscattering spectrometry is a dominant ion beam analytical technique in thin films science. This due to the non-destructive nature, simplicity, identification power, possibility of simultaneous multi-element depth profiling with good depth resolution. As this technique depends on the detection of backscattered alpha particles, the detector is placed at angles between 90^{o} to 180^{o} with respect to the incoming beam – see Figure 4.3 for the definition of the angle. The backscattered yield vs. channel number is measured if only the backscattered alpha particles are detected. Therefore, it is possible to collect information about masses and the depth distribution of the target elements if the stopping power, kinematic factor and scattering cross section of the ions are well understood. All the above factors are discussed later in this chapter.

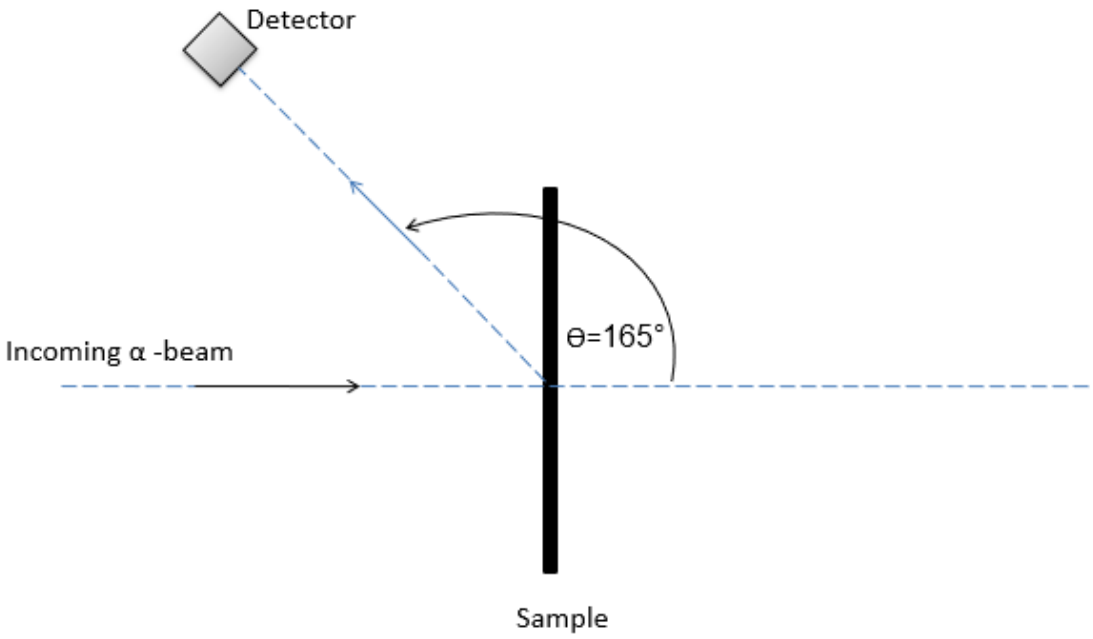

Figure 4.3: *A schematic diagram showing the RBS experimental setup at the University of Pretoria.*

4.1.3 Kinematic factor

When an ion beam hits a solid target, energy is transferred from the incident projectile ions to target atoms. This process is described by kinematic equations describing an elastic collision [Ken12]. In a classical two-body elastic collision- see Figure 4.4, the backscattered α-particle (E_1) can be calculated by using the conservation of energy and momentum:

$$E_1 = KE_0 = \left(\frac{\left(M_2^2 + M_1^2 \sin^2\theta\right)^{1/2} \pm M_1 \cos\theta}{M_2 + M_1} \right)^2 * E_0 \qquad (4.1)$$

where E_o and E_1 is the energy of the incident and backscattered particles respectively, M_1 and M_2 are the masses of the analysing particle (α-particle) and the target atom, K is the kinematic factor (the ratio of the backscattered particle's energy to its incident energy before scattering) and θ is the scattering angle. The scattering angle θ and the recoil angle φ are defined as positive numbers with the arrows as shown in Figure 4.4. All quantities refer to a laboratory system of coordinates. When the incoming particle collide with a target atom, the target atom then recoils from its initial site at angle φ with respect to the incident beam - see Figure 4.4.

From equation (4.1), the energy of the backscattered particle (E_1) can be calculated using the kinematic factor K. The kinematic factor K is the ratio of the energy of the backscattered particle E_1, to that of the incident particle E_0 (i.e. E_1/E_o). The kinematic factor K depends only on the mass ratio M_1/M_2 and on scattering angle θ as indicated above. In equation (4.1), the

plus sign is taken when the mass of the projectile (M_1) is less than that of the mass of the target atom (M_2), otherwise the minus sign is taken.

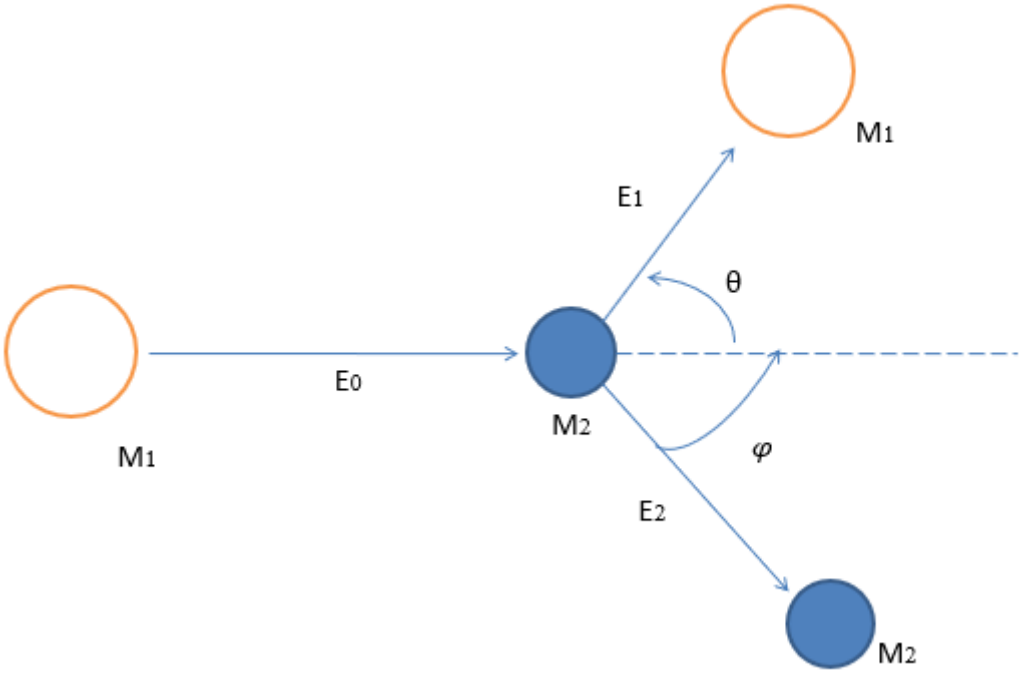

Figure 4.4: *Schematic picture of elastic scattering. M_1 and M_2 are the masses of the incident ion and recoiling atoms, respectively.*

4.1.4 Depth scale

The incident projectiles collide with atoms in the target at different depths. Recoiled particles with different energies will therefore be detected [Chu78]. From the setup of the experiment (see Figure 4.5) we can calculate a relation between energies of detected backscattered particles and their original depth.

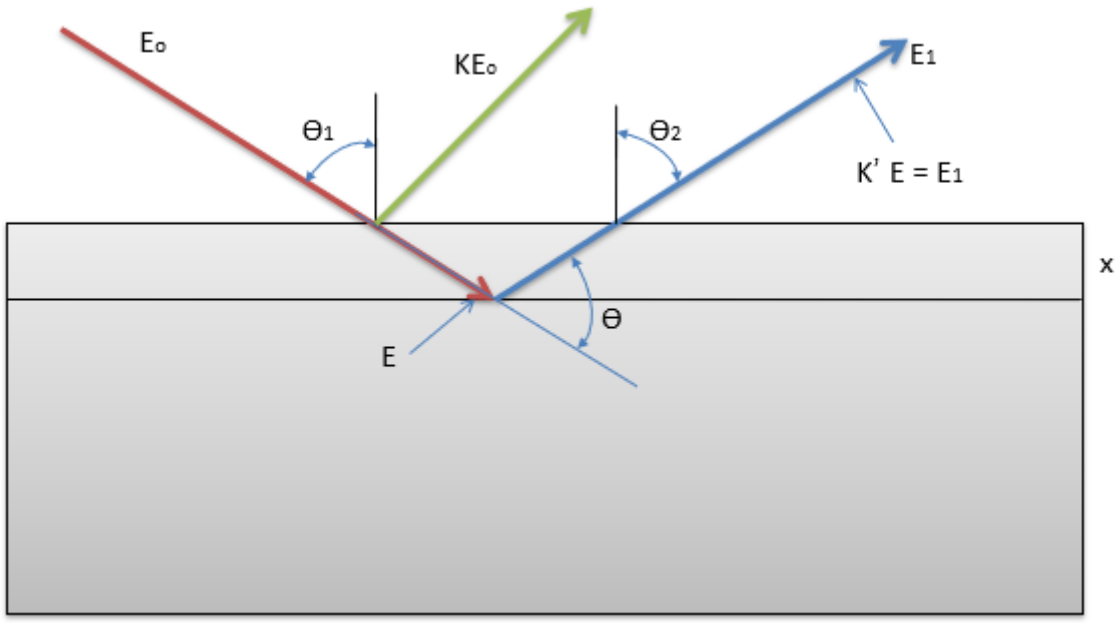

Figure 4.5: *A schematic diagram showing the backscattering event of an alpha particles and its energy loss from depth x. Recoiled particles, from the target surface, have the largest energies. The incident projectiles and recoiled particles loose their energy when traveling through the target. From the energies of the detected particles their depth of collision can be calculated.*

The energy of the incident alpha particle in the Figure (4.5) above is given as E_o. The initial energy of the incident alpha particle E_o reduces to E just before the backscattering because the particle loses energy moving through the substrate. The backscattered particle at depth x loses more energy on its way out of the target and eventually the energy reduces to the exit energy E_1. Therefore, the backscattered alpha particle from the substrate surface will have a higher energy (i.e. KE_o) compared to one backscattered from depth x (i.e. E_1). This is due to the two-body elastic collision (mentioned in section 4.1.3) between the alpha particle and substrate atom on the surface compared to the multi-collisions at depth x.

The energy lost by the alpha particle on its way into the target particle is given as $E_o - E$ while the energy lost on its way out is given as $K'E - E_1$. Assuming that the energy loss (dE/dx) is constant over each path, the energy of the backscattered alpha particle at depth x is then given as [Chu78]:

$$KE_o - E_1 = \left[\frac{K}{\cos\theta_1}\frac{dE}{dx}(in) + \frac{1}{\cos\theta_2}\frac{dE}{dx}(out)\right] * x \qquad (4.2)$$

where 'in' and 'out' refer to the constant values of dE/dx along the inward and outward path, KE_o is the energy of the backscattered alpha particles at the surface atoms of the target, while E_1 is the energy of the alpha particle backscattered from the atom at depth *x*.

The difference between E_1 and KE_0 is ΔE:

$$\Delta E = KE_0 - E_1 \tag{4.3}$$

Then equation 4.3 can written as:

$$\Delta E = [S]\, x \tag{4.4}$$

The energy loss factor that contains the relationship between energy and depth information is represented by [S]. Where [S] is given by

$$[S] = \left[\frac{K}{\csc\theta_1}\frac{dE}{dx}(in) + \frac{1}{\csc\theta_2}\frac{dE}{dx}(out)\right] \tag{4.5}$$

The depth resolution δx of the RBS at depth *x* is defined as the depth interval that corresponds to the total detected ion energy spread δE_1, where E_1 is the energy of the alpha particle backscattered from the atom at depth *x*.

$$\delta x = \delta E_1/[S] \tag{4.6}$$

where δE_1 is the energy spread and often called the energy resolution, *[S]* is the stopping factor and is defined above in equation (4.5). The energy spread δE_1 of the detected ions is affected by several factors such as: (I) ion beam energy distribution, (II) ion beam collimation and focusing, (III) ion elastic and inelastic scattering within the sample and (IV) the detection of backscattered ions.

The resultant energy distribution may be obtained as a convolution of energy distributions resulting from the all factors mentioned above. When these distributions are Gaussian, the resultant ion energy spread δE_1 can be approximated by the full width at half maximum (FWHM) of their convolution and calculated by summing quadratically the FWHMs of all components.

$$\delta E_1^2 = \sum_i \delta E_i^2 \tag{4.7}$$

4.1.5 Scattering cross section

As mentioned in section 4.1.4, the elastic collision between the projectile and the target atom can result in a backscattering event. The average differential scattering cross section is used in RBS to express the probability of a backscattering event at a particular solid angle. The

differential cross section is defined by the number of particles recorded by a detector (*A*) in the solid angle (Ω) per number of incident particles per unit area. The differential cross section (σ) for backscattering is given in the equation (4.8) below [Chu78]

$$\sigma = \left(\frac{Z_1 Z_2 e^2}{4E}\right)^2 . \frac{4\left[\left(M_2^2 - M_1^2 sin^2\theta\right)^{\frac{1}{2}} + M_2 \cos\theta\right]^2}{M_2 sin^4\theta \left(M_2^2 - M_1^2 sin^2\theta\right)^{\frac{1}{2}}} \quad (4.8)$$

where E is the energy of the projectile immediately before scattering (see Figure 4.5), Z_1 is the atomic number of the projectile with mass M_1, Z_2 is the atomic number of the target with mass M_2, σ is the differential cross-section in the laboratory system, e is the electronic charge and θ is the scattering angle.

The total number of the backscattered projectiles registered by the detector can be written as:

$$A = \sigma \Omega Q N \quad (4.9)$$

The total number of incident particles (Q) is determined by the time integration of the current of charged particles incident on the target, *A* is the detected particles by the detector. If σ and Ω are known (σ is the differential cross section and Ω is the solid angle of the detector). Then the number of target atoms per unit area, *N* [atoms/cm^2], can be calculated from equation (4.9).

4.1.6 RBS calibration

The incident energies of 1600 keV and 1400 keV were used together with the corresponding channel numbers of silicon and carbon to perform the energy calibration of the acquired RBS spectra. The corresponding kinematic factor (*K*) of the elements on the surface was multiplied by the incident beam energy (E_0) to obtain the surface energy values (KE_0). These surface energy (KE_0) values were then plotted against the surface energy channel position of the Si and C elements. A graph with a linear fit of energy of the scattered He^+ vs the surface channel number was plotted. This fit can be represented by a linear equation:

$$E = mx + c \quad (4.10)$$

where m and c are the energy conversion factor (in keV/ch) and the offset in (keV) respectively. This linear fit equation is used to obtain the energy to channel function which determines the location of the peak edge of the elements from the RBS spectra. The energy calibration curve obtained for this study is shown in Figure 4.6. From the straight line in Figure 4.6, the energy conversion factor (m) was calculated as 3.075 keV while the offset (c) at channel zero is 34.9 keV.

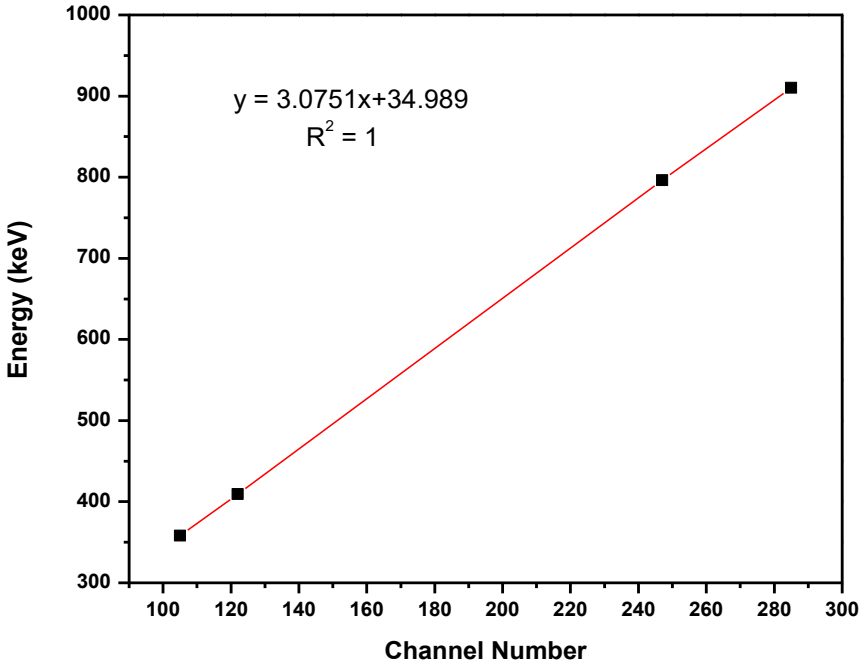

Figure 4.6: *The energy calibration curve.*

4.2 Scanning electron microscopy (SEM)

The history of electron optics started in 1925, when Busch showed that an electro-magnetic field could be used to focus electrons. In 1924 his contemporary, de Broglie, postulated the wave nature of the electrons. Later, Ernst Ruska and Max Knoll (in 1931) confirmed Busch's lens formula experimentally and the idea of an electron microscope began to grow. Finally, Knoll and Ruska built the first working Transmission Electron Microscope (TEM) in 1936. But it was realized that TEM could not be used to investigate all kinds of samples, like the topography of bulky samples cannot be imaged. This led to the introduction of a new class of electron microscope, the scanning electron microscope (SEM). In 1935, Knoll was the first one who suggested the scanning electron beam device. The first scanning electron microscopy was built in 1942 by Zworykin with a resolution of 50 nm. Finally, in 1963 Pease and Nixon built the first prototype of a high-resolution SEM that is able to reach 6 nm resolution, which was commercialized in 1965 by Cambridge Scientific Instrument, under the name of "Stereoscan" [Oat02].

In scanning electron microscopy, an electron beam is scanned across a sample's surface and variety of signals are generated when the electrons interact with the sample. The interaction of the electrons with material is discussed in more details in section 4.2.1.

4.2.1 Interaction of electron beam with materials

In this section, we review briefly the physics of electron beam interaction with matter. Figure 4.7 shows the number of different particles that are produced when the electrons interact with the sample.

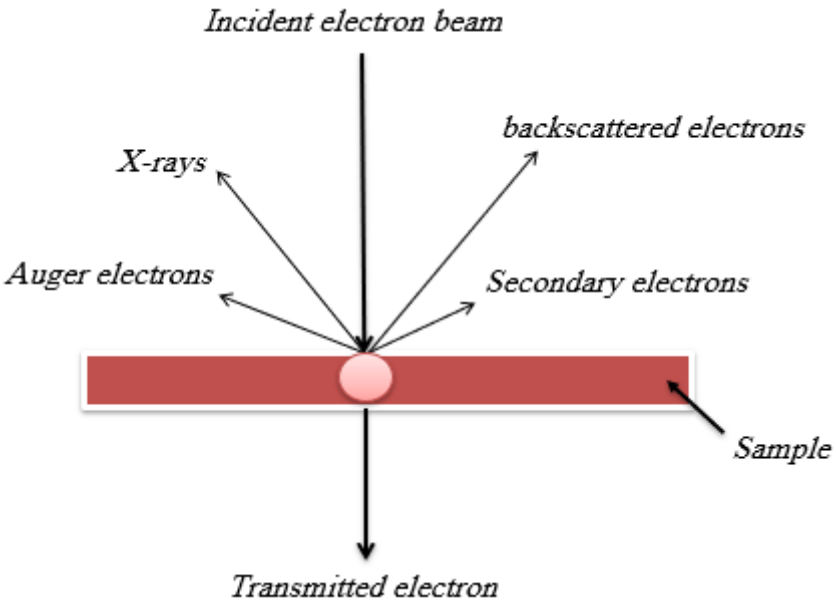

Figure 4.7: *A schematic diagram showing the rays which are emitted when an energetic electron hits the sample.*

Electron-matter interactions can be classified into two classes

a. Elastic Interactions

In this interaction, no energy is transferred from the electron to the sample. As a result, the electron leaves the sample with its original energy E_0. The electron trajectory within the specimen changes because it deflected from its path by coulomb interaction. Here, the backscattered electrons (e^-) are generated by an elastic collision between an incoming electron and nucleus of the target atom. The elements with higher atomic numbers will produce more backscattered electrons. Therefore, a sample composed of two or more elements differing significantly in their atomic number, will produce an image showing great contrast of the elements despite a uniform topology. For example, in the image formed by these electrons, strontium or silver will appear brighter than Si and C of SiC because of higher Z. The backscattered electrons can also be used to form electron backscatter diffraction (EBSD) image which is useful in the determination of crystallographic structure of the sample [Cha86].

b. Inelastic Interactions

In this interaction, a part of the energy that an electron carries are transferred to the specimen. The result is the generation of:

- Secondary electrons

These electrons are the results of the inelastic collisions between the incident electrons and the electrons of the target atoms. Secondary electrons usually have energies of less than 50 eV and are used to form the image of the surface topography of the sample in SEM system [Chr12]. These electrons are generated along the incident electrons' trajectories. However, only those electrons generated from a very shallow depth from the sample surface (within 5 to 15 nm) are detected; – the others are absorbed in the sample owing to their low energy.

- Auger electrons

Excitation caused by the primary electron beam can create inner shell holes (in low energy levels). Outer shell electrons (in high energy levels) then move to fill up the holes in the lower levels. This creates an energy surplus in the atom, which can be corrected by emitting an outer (lower energy) electron (Auger electrons) or by the production of an X-ray. Auger electrons are emitted from the near surface region of the sample. Therefore, the signals resulting from Auger electrons can be utilized for chemical analysis of the sample surface [Zha09]. The X-rays signals are also used in chemical characterization of the sample by using a technique commonly referred so as dispersive X-rays spectroscopy (EDS).

The volumes involved in the production of backscattered electron, secondary electron and X-rays, form into a shape that ranges from oval to a semi-circle within the specimen- see Figure 4.8 (a) and (b). This shape is called an interaction volume and depends on the following three factors: electron energy, the atomic number Z of the target and the angle of incidence for the electron beam. Higher energy electrons penetrate deeper into the sample and generate a larger interaction volume as compares to the less energy electrons - see Figure 4.8 (a). A sample with high atomic number Z stops or absorbs more electrons and causes a small interaction volume. The angle of incidence of the electron beam: the greater the angle (further from normal), the smaller the volume.

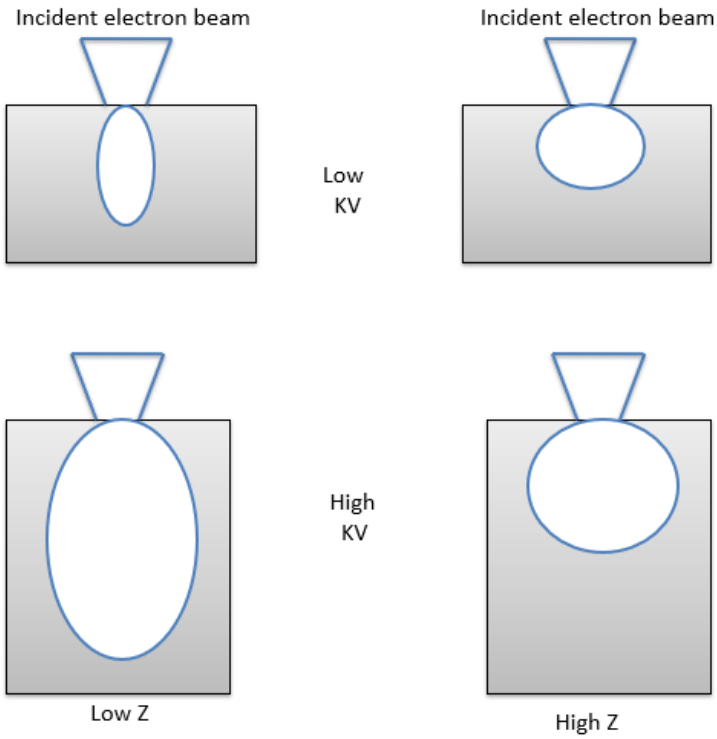

Figure 4.8 (a): *Interaction volumes of the incident electron beam (white) in compact samples (grey) depending on electron energy and atomic number Z.*

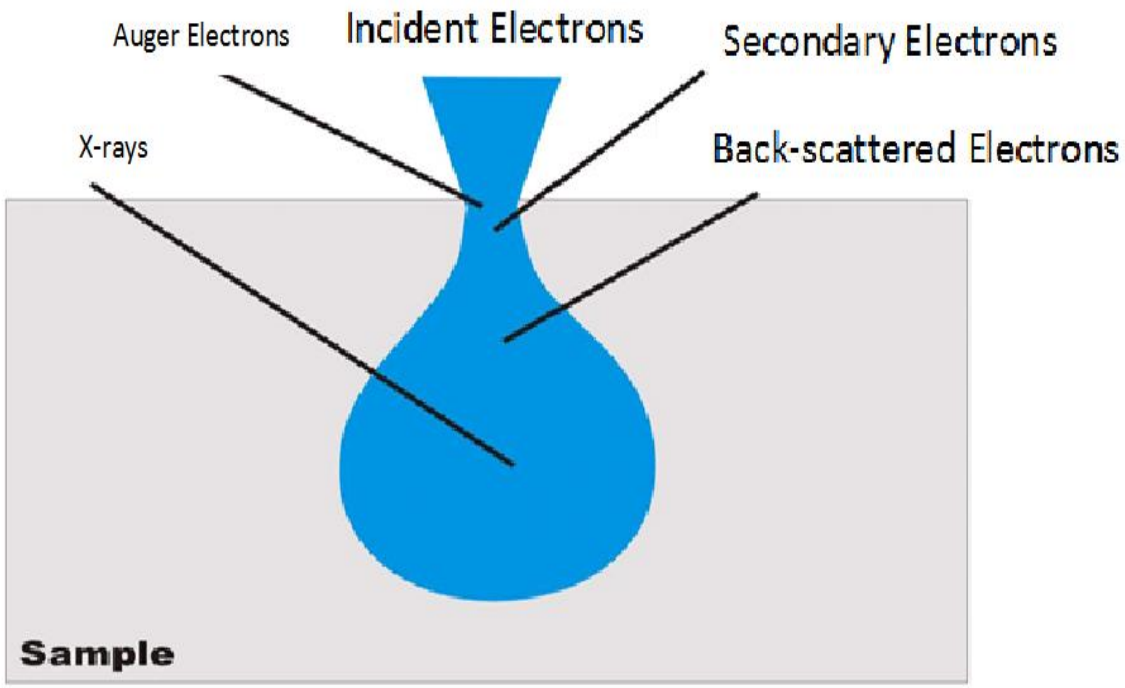

Figure 4.8 (b): *A schematic diagram of the interaction volume in a compact sample and the origins of detectable signals.*

4.2.2 Components of Scanning Electron Microscopy

The cold field emitter (CFE) relies purely on the high applied field (i.e. electric field) to cause electrons to tunnel out of the cathode wire. The CFE has its name because CFE sources are operated at room temperature. Then the emission of electrons is only a factor of the voltage applied between the cathode and the anode. Cold field emission requires that the cathode surface must be atomically clean. This is done by having the CFE in an ultrahigh vacuum. Before the operation, the tip is flushed clean by heating it for a few seconds to a temperature of about 2500 K. This cleaning process shortens the lifetime of the emitter. Since a tip is usually only flashed once a day, the useful life of a CFE is very long. The advantage of the CFE is the virtual source size of 3-5 nm, which requires little demagnification to obtain a 1 nm diameter probe.

In the thermionic emission, the free electrons are emitted from the surface of a metal when external heat energy is applied. Since the thermal field emitter (TFE) is operated at elevated temperatures, the electrons emission in TFE is found to fall in the intermediate region between field emission and thermionic emission [Tab12]. This elevated temperatures during the operation of TFE has the advantage of keeping the tip clean and reducing the adsorption of gases on the tip.

Apart from CFE and TFE mentioned above, the third type of the field emission sources is the Schottky field emitter (SFE). The SFE is the type fitted on a Zeiss Ultra 55 field emission scanning electron microscope (at University of Pretoria's Laboratory for Microscopy and Microanalysis) which was used in this study. The SFE source is operated at high temperature (i.e. 1800 K) in an ultrahigh vacuum. Schottky field emitters are made by coating the tip (i.e. tungsten) with a layer of zirconium oxide (ZrO_2). Zirconium oxide is deposited on the tungsten tip in order to reduce the work function of tungsten. In the Schottky emitter, the ultrahigh vacuum aids its long-term stability, prevents poisoning of the ZrO_2 cathode, and maximizes brightness.

Modern advanced microscopy work requires SEM systems with a stable electron gun. The stability of an electron gun is a measure of how constant the electron emission is per unit time. Schottky field emitters (SFE) are the most stable sources with a beam current stability of about 1%/h.

From the above paragraph, the stability of an electron gun is a key aspect of electron microscopy. There are three major types of electron guns: the tungsten filament, Lanthanum hexaboride (LaB_6) and field emission. The three types of field emissions (CFE), (TFE) and (SFE) are discussed above. In the tungsten filament, the electron emission requires electrons to gain enough energy to exceed the work function of the filament (4.55 eV for tungsten). In a filament this is provided by thermal processes (i.e. thermionic emission), which is why tungsten filaments for electron sources operate at >1000 ˚C. That heat is, in turn, produced by electrical resistance of current in the filament. The Lanthanum hexaboride (LaB_6) filament is also a thermal filament (i.e. thermionic emission). However, it is more efficient than the tungsten filament due to its lower work function.

The electron beam energy spread is the spread in electron energies leaving the source. The energy spread describes the different energies of the individual electrons in the beam. The field emitter guns offer a smaller energy spread (0.3 - 0.7 eV) as compared to LaB_6 gun (i.e. 1.5 eV), while it is 3 eV for the tungsten hairpin gun. This high energy spread (3 eV) for the tungsten hairpin gun can result in chromatic aberration, where the beam is slightly less focused due to these energetic differences. Since the field emitter guns have the lowest energy spread of about 0.3 - 0.7 eV, it is the best option (from the three guns mentioned above) to get high resolution images in SEM systems.

A series of electromagnetic lenses and apertures are used to guide the electron beam into the specimen and focus the beam of electrons on it. The apertures control the final electron beam size (probe size) on the specimen. The probe is scanned across the sample, and the signal is produced (i.e. secondary electrons and backscattering electrons - as discussed in section 4.2.1). These signals are detected and amplified before being displayed on the monitor.

A secondary electron detector attracts those scattered electrons and depending on the number of electrons that reach the detector, registers different levels of brightness on a monitor. As seen in Figure 4.9, for perpendicular incidence, the illumination region is uniform around the axis of the beam when the surface is flat. In the flat surface, only secondary electrons activated near the surface can escape. Any secondary electrons elsewhere in the interaction volume (see Figure 4.8 (a) and (b)) will be captured or absorbed in the sample before they can escape owing to their low energy. More secondary electrons can escape the sample surface on edges or the protrusion and spherical shapes than in flat areas. The tilt effect and edge effect are among the contrast factors for secondary electrons, both as a result of sample surface morphology.

Therefore, effects of topography on the generation of secondary electrons give form and outline to the images produced by the Secondary Electron detector- see Figure 4.9. Secondary electrons preferentially flow to and are emitted from edges, protrusion and spherical shapes of the sample. This results in the edge, protrusion and spherical shapes appearing brighter- see Figure 4.9. Similarly holes on the surface will result in a lower yield of secondary electrons due to less electrons which can escape from the hole (as seen in Figure 4.9). This will result in a hole being darker on the monitor.

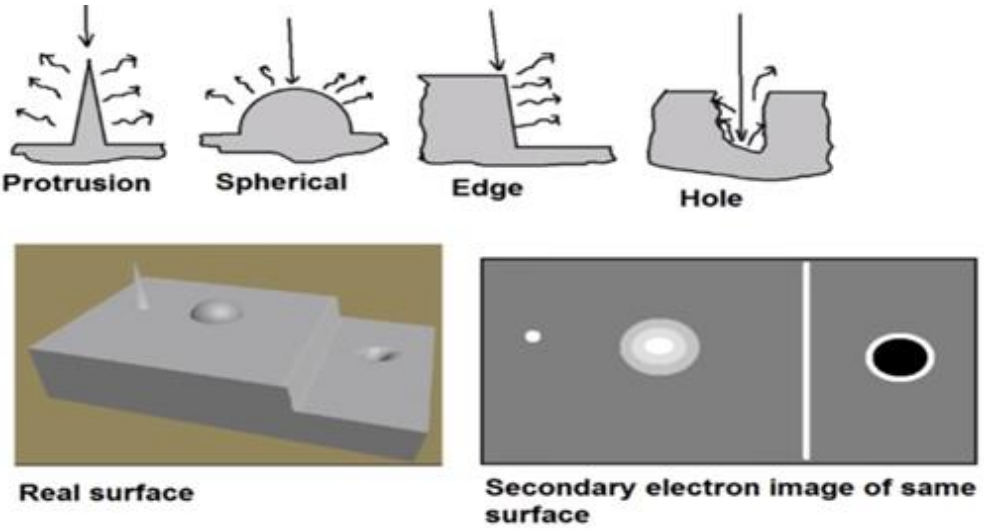

Figure 4.9: *A schematic representation of the edge effect of SE with different surface conditions. Taken from [www2].*

In this study, a high-resolution Zeiss Ultra 55 field emission scanning electron microscopy (FESEM) operated at 2 kV under vacuum was used. This FESEM uses a Schottky field emission gun. The Zeiss Ultra 55 is contains three systems namely: SE (secondary electron) detector, BE (backscattered electron) detector and an in-lens SE detector. In this study, the in-lens SE detector was used. In-lens SE detector is highly surface sensitive. This is due to the small penetration depths and smaller scattering volume of low energy electrons. FESEM was used to study the SiC surface before and after ion implantation, swift heavy ion irradiation and annealing. The results are discussed in chapter 6.

4.3 Raman Spectroscopy

Raman spectroscopy is a technique based on the inelastic scattering of monochromatic light, using a laser source. The inelastic light scattering in a substance means that the photons in the incident light transfers their energy to molecular vibrations. These photons with energy E_o

interact with a molecule, and they can be either transmitted, reflected or scattered at the same energy. Some of the incident photons will be scattered at optical frequencies that differs from their incident energies E_o (i.e. inelastic scattering). This process is known as the Raman Effect. The frequencies of the scattered photons are shifted up or down (i.e. have higher or lower frequencies compared to their initial frequency) in comparison with original monochromatic frequency. This shifting gives information about rotational, vibration and electronic energy of a molecular or crystal structure. This means that the Raman spectra will be different depending on the material's molecular structures. Raman spectroscopy can be used to study different types of materials (solid, liquid and gaseous). It can also be used for probing the molecular structure and any changes induced in the material. In this research, Raman spectroscopy is used to study the SiC structure before and after ion implantation, swift heavy ion irradiation and annealing. Figure (4.10) showed three different form of laser light scattering, namely Rayleigh scattering, Stokes and anti-Stokes Raman scattering. The Rayleigh scattering is an elastic scattering, which is strong and has the same frequency as the incident beam (ν_0). Raman scattering has frequencies of $\nu_0 \pm \nu_m$, where ν_m is the vibrational frequency of a molecule. This lines of $(\nu_0 - \nu_m)$ and $(\nu_0 + \nu_m)$ are named the Stokes and anti-Stokes lines respectively - see Figure (4.10). Therefore, in this spectroscopy we measure the vibrational frequency (ν_m) as a shift from the incident beam frequency (ν_0).

A modern Raman instrument consist of four major components which is: a) excitation source (Laser), b) sample illumination system and light collection optics, c) wavelength selector (filter or spectrophotometer), d) detector (array, CCD or PMT) [Jia11]. A sample is normally illuminated with a laser beam in the ultraviolet (UV), visible (Vis) or near infrared (NIR) range. Scattered light is collected with a lens and is sent through an interference filter or spectrophotometer to obtain Raman spectrum of a sample.

Due to the weakness of the Raman scattering, it is very difficult to separate it from the dominant Rayleigh scattering. Therefore, sensitive multi-channel detectors like Charged Coupled Devices (CCD) are used to increase the sensitivity to the Raman scattering. To improve the sensitivity of the Raman instrument to the Raman scattering, notch filters are also used. Notch filters are used to transmit both Stokes and anti-Stokes Raman signals while blocking the Rayleigh scattering (which mentioned above) from reaching the detector. A schematic diagram of the Raman setup is shown in Figure 4.11.

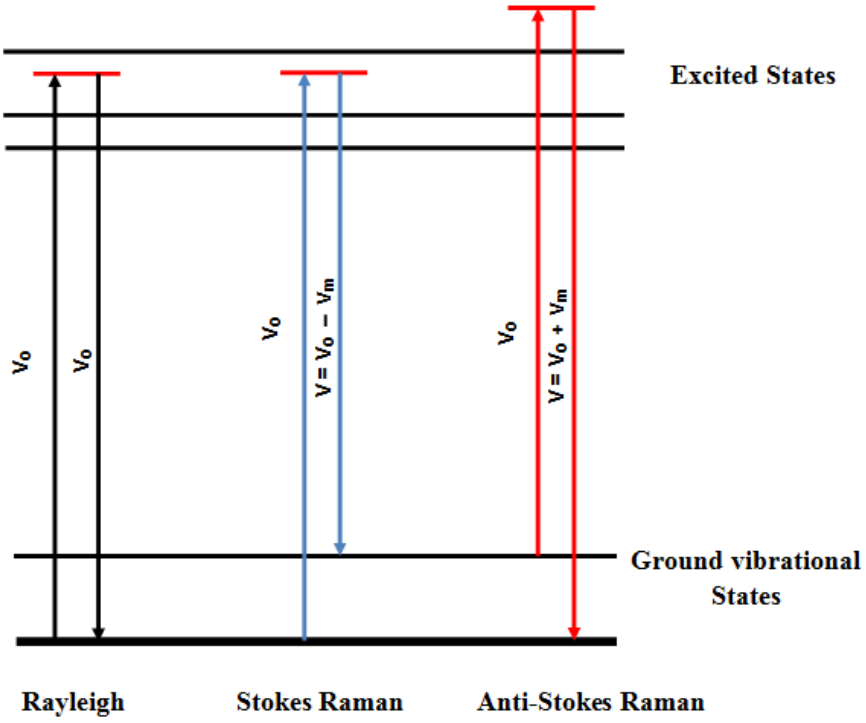

Figure 4.10: *Shows the three different forms of laser scattering.*

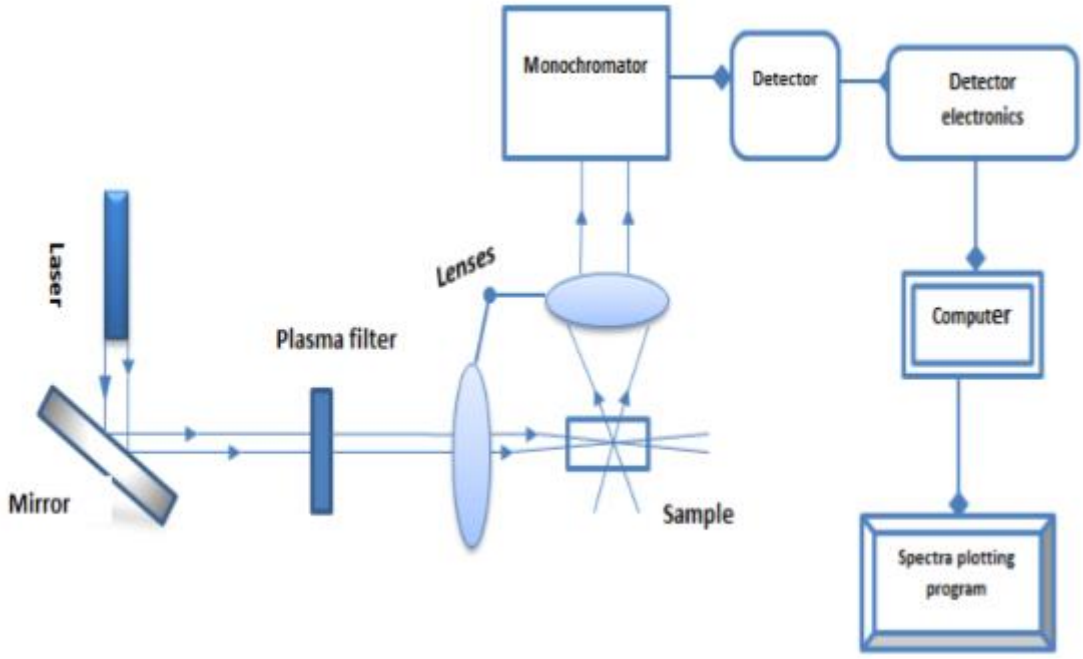

Figure 4.11: *Schematic diagram showing the different components of a Raman instrument. Taken from [Odu17].*

In this study, Raman analyses was done using a T64000 series II triple spectrometer system from HORIBA Scientific, Jobin Yvon Technology. The 514.3 nm laser line of a coherent

Innova® 70C series Ar^+ laser (spot size ~ 2 µm) with a resolution of 2 cm^{-1} in the range of 200 cm^{-1} – 1800 cm^{-1} was used. The measurements were obtained in a backscattering configuration with an Olympus microscope attached to the instrument (using an LD 50x objective). The laser power was set at 1.7 mW. An integrated triple spectrometer was used in the double subtractive mode to reject Rayleigh scattering and dispersed the light onto a liquid nitrogen cooled Symphony CCD detector. The Raman spectra were recorded under these conditions and normalized to have the same scale. The Raman spectra SiC before and after ion implantation, swift heavy ion irradiation and annealing are presented in chapter 6.

4.4 References

[Cha86] S. K. Chapman, Working with a scanning electron microscope. Lodgemark, London. (1986) 79-86.

[Chr12] C. Scheu and W. D. Kaplan, Introduction to scanning electron microscopy. Wiley-VCH Verlag GmbH & Co. KGaA. (2012).

[Chu78] W. Chu, J. W. Mayer and M. Nicolet, Backscattering spectrometry. Academic Press. (1978).

[Gol96] F. Golgberg and É. J. Knystautas, NiTi thin film characterization by Rutherford backscattering spectrometry. Mater. Sci. Eng. B. 40 (1996) 185-189.

[Jia11] I. Jain and G. Agarwal, Ion beam induced surface and interface engineering. Surf. Sci. Rep. 66 (2011) 77- 172.

[Ken12] K. Mizohata, Progress in elastic recoil detection analysis. HELSINKI. (2012).

[Oat02] C. W. Oatley, The early history of the scanning electron microscope. J. Appl. Phys. 53 (1982) 1-13.

[Odu17] O. S. Odutemowo, Modification of glassy carbon under strontium ion implantation. PhD thesis, University of Pretoria. (2017).

[Tab12] A. Tabbakha, A fresh look at thermal field emission from tungsten tip. Turk. J. Phys. 36 (2012) 271 – 278.

[www1] http://www.lbl.gov/abc/wallchart/chapters/11/2.html, 11 September 2012.

[www2] Scanning electron microscopy (SEM) lecture with animations and real measurement. YouTube, https://www.youtube.com/watch?v=Mr9-1Sz_CK0 .

[Zha09] S. Zhang, L. Li and A. Kumar, Materials characterization techniques. 1th Edition. Taylor and Francis. (2008).

CHAPTER 5
EXPERIMENTAL PROCEDURE

The migration behaviour of silver and strontium, structural changes of 3C-SiC and its surface modification after ion implantation, swift heavy ion irradiation and annealing have been investigated. A set of samples were implanted with low energy ions (i.e. in order of hundred keV), and the other set of samples were both implanted and then irradiated with swift heavy ions (i.e. in order of hundred MeV) in order to study the material behaviour in this environment. The sample analysis was done using Rutherford backscattering spectroscopy (RBS), scanning electron microscopy (SEM) and Raman spectroscopy techniques. This chapter discusses the sample preparation processes.

5.1 Sample preparation

The starting materials for this study were polycrystalline 3C-SiC wafers from *Valley Design Corporation*® (made up of predominantly 3C-SiC crystallites). Before implantation and swift heavy ion irradiation of the SiC wafers, the SiC was chemically cleaned. The SiC wafer was sequentially cleaned using acetone, methanol, trichloroethylene, 10% hydrochloric (HCl) acid and 10% dilute hydrofluoric (HF) acid, after each step the samples were rinsed in de-ionised water. The de-ionised water was blown away using nitrogen gas. Acetone removes most of the oils and organic residues, which appear on SiC surface. Unfortunately, acetone itself leaves its own residue. Therefore, after cleaning by acetone, the SiC was immersed in methanol for 10 minutes to remove the acetone residue. Trichloroethylene was used to remove the fingerprints or other heavy residue on the SiC wafer surface and acts as a further cleaning solvent. 10% HCl acid was used to remove ionic and metallic contamination from the surface of SiC. 10% HF was used remove the natural oxide layer from SiC wafer. Then, the cleaned SiC wafers were sent for implantation.

After implantation, discussed in section 5.2, the wafer was cut into 5×5 mm^2 samples with a rotary diamond saw, and cleaned with acetone to remove contamination on the surfaces that was introduced during the cutting process. The size of the samples was chosen to suit the RBS and SEM analyses experiments. Some of the implanted samples were irradiated with swift heavy ions, discussed in section 5.3. After irradiation with swift heavy ions the samples were also cleaned with acetone, de-ionized water and methanol to wash off the glue used to fix the

samples to the sample holder (i.e. the glue was used during the process of ion irradiation- see section 5.3). The samples, both as-implanted and irradiated, were analysed using RBS, SEM and Raman spectroscopy techniques before and after annealing. Figure (5.1) depicts the typical processes of sample preparation and analysis.

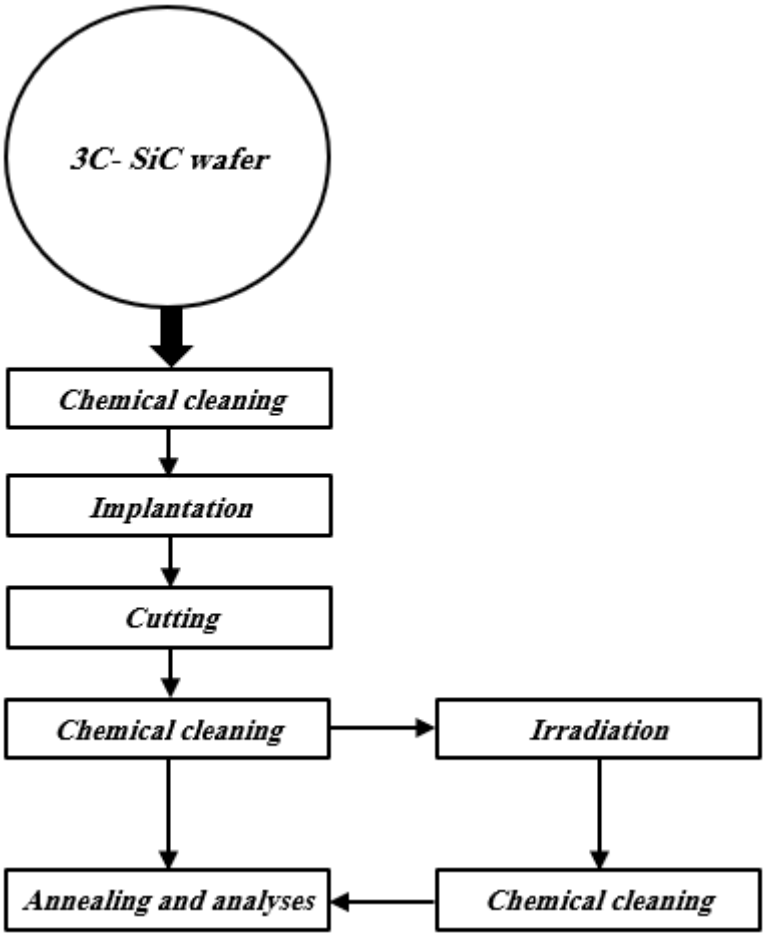

Figure 5.1: *A diagram showing the typical process of sample preparation and analysis.*

5.2 Ion implantation

Implantation of two radiologically significant fission product elements namely silver and strontium in SiC were performed for the various investigations in this study. These investigations included near-surface recrystallization of the amorphous implanted layer (3C-SiC) and the diffusion behaviour of silver and strontium in 3C-SiC at vacuum annealing temperature above than 1000 ˚C.

The implantations for this study were done at the Institut für Festkörperphysik, Friedrich-Schiller-Universität, Jena, Germany using 400 kV implanter Romeo. The ion beam setup of all the accelerators and beam lines are shown in Figure (5.2).

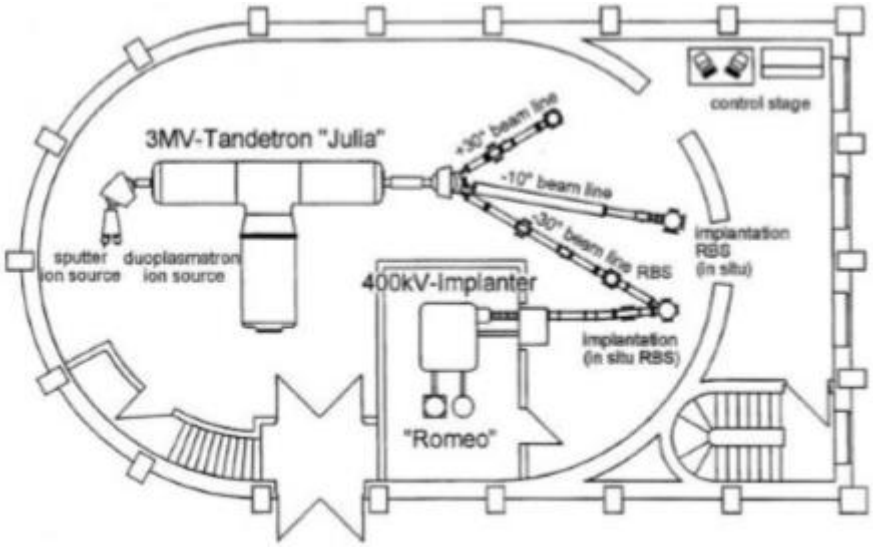

Figure 5.2*: Illustration of the ion beam laboratory at the Institute of Solid State Physics, Friedrich-Schiller-Universität, Jena, Germany. Taken from [www1].*

The silver ($^{109}Ag^{+}$) and strontium ($^{88}Sr^{+}$) ions were implanted separately into two 3C-SiC wafers. This implantation was done at an energy of 360 keV with a fluence of 2×10^{16} cm^{-2} at room temperature. The flux was kept below 10^{13} cm^{-2} s^{-1} to avoid beam induced target heating of the sample. Reducing the heating of the sample during the implantation will reduces the probability of simultaneously annealing some of the induced damage. Since polycrystalline samples were used, the channelling effect during the implantation can be neglected due to the different orientations of the crystals. Thus, the samples can be orientated at any angles. In this study, the angle of incidence of the ions was set at an angle of 7˚ relative to the normal. All the implantations were done at an average vacuum of 10^{-4} Pa.

5.3 Ion irradiation

The irradiation of swift heavy ions in this study was performed at The Joint Institute for Nuclear Research, Dubna, Russia using IC-100 FLNR cyclotron. The xenon ions (Xe^{+26}) were irradiated at room temperature with fluences of 3.4×10^{14} cm^{-2} and 8.4×10^{14} cm^{-2} with an energy of 167 MeV into the implanted 3C-SiC samples. To reduce heating, the ion current was kept at 0.5 μA and the samples were fixed with a heat-conductive glue to the sample holder. Ion beam homogeneity over the samples, surfaces was achieved by use of a 2-dimensional beam scanning

system. The irradiations with swift heavy ions (SHIs) were performed to investigate the structural changes for room temperature SHIs irradiated polycrystalline SiC compared to un-irradiated (i.e. only implanted) SiC. Raman spectroscopy and scanning electron microscopy were used to study the structural changes and surface modification of both samples before and after thermal annealing process. The effects of the SHIs and annealing on the migration behaviour of silver and strontium implanted in SiC were also investigated using RBS. The annealing conditions of the samples are discussed in section 5.4 below.

5.4 Annealing of the samples

For the annealing cycles, the implanted and irradiated 3C-SiC samples were placed inside glassy carbon crucibles. In this study, all samples were subjected to isochronal vacuum annealing from 1100 ˚C to 1500 ˚C in steps of 100 ºC for 5 hours at a pressure of the order of 10^{-6} mbar. The annealing was performed in a high temperature vacuum computer-controlled *Webb 77*® graphite furnace with a maximum temperature of 2300 ˚C. The implanted samples were annealed in separate crucibles. This was done to prevent cross contamination. Also, the crucibles were covered with lids made in glassy carbon to avoid contamination of the samples with any contaminant in the oven. The contamination of the annealing samples with any other elemental residues that may be stuck in the furnace walls is very possible since the furnace is used by different researchers for various studies. The *Webb 77*® temperature is controlled by a Eurotherm 2704 controller which is connected to a thermocouple as well as a pyrometer. The thermocouple can measure the temperature up to 1475 ˚C, while the pyrometer is used to measure the temperature above 1525 ˚C. An average value of the pyrometer and thermocouple readings is taken for a temperature ranging from 1475 ˚C to 1525 ˚C, e.g. for the 1500 °C annealing.

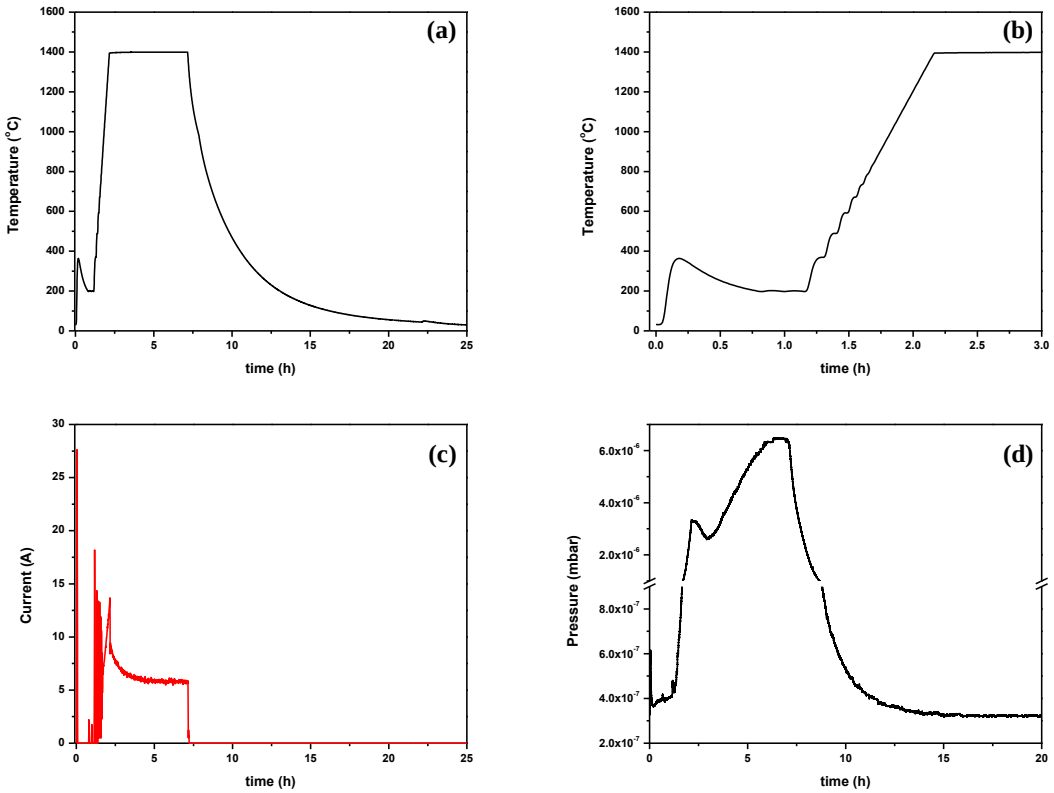

Figure 5.3: *(a) Heating and cooling curves for samples annealed at 1400 ˚C for 5 hours. (b) The heating curve shows overshoot in first 30 min. (c) Current curve during annealing. (d) Vacuum pressure during annealing.*

Figure 5.3 shows the current, vacuum pressure and a typical heating and cooling curves for the furnace as a function of time. Before each annealing cycle, the oven was evacuated to a pressure in the 10^{-7} mbar range – see Figure 5.3 (d). As shown in Figure 5.3 (a) and (b), degassing was performed at 200 ˚C for one hour to ensure that the maximum pressure during annealing is kept at or below the 10^{-6} mbar region as well as to reduce the total pumping time. The degassing temperature overshot from 200 ˚C to 370 ˚C (Figure 5.3 (a) and (b)). This was due to temperature controlling set-up by the manufacturer, which resulted in the initial large current and fluctuations as shown in Figure 5.3 (c). During the annealing process the vacuum pressure increases from 10^{-7} to 10^{-6} mbar due to the increased degassing by the high initial current. The heating rate of the oven was programmed at 20 ˚C/min. After switching on the heating element, it heated up to a selected temperature (i.e. 1400 ˚C as seen in figure 5.3 (a) and (b) at 2.25 hours) and then stayed there for the set annealing time, i.e. 5 hours. A current of about 28 A was measured in the beginning of the heating process (seen Figure 5.3 (c)), which later dropped to 0 A. The current was dropped to 0 A to reduce the overshooting above the set temperature

(as mentioned above, temperature overshoot from 200 ˚C to 370 ˚C). After degassing, which was performed at 200 ˚C, the current increased again up to 18 A to increase the temperature inside the oven to the selected temperature (i.e. 1400 ˚C). The current was dropped to 8 A during the desired annealing temperature for 5h. At the end of annealing time, the current was turned off and the system cooled down (see Figure 5.3 (a) and (c)). The Webb oven cooling is approximately given by Newton's cooling law

$$T(t) = F\,exp(-Zt) \tag{5.1}$$

Since the cooling rate can be found by the time derivative of the decrease in temperature, then the equation (5.1) can be written as:

$$\frac{dT}{dt} = -FZ\exp(-Zt) \tag{5.2}$$

where T and t represents the temperature and time respectively, F and Z are constants. For the our *Webb77* furnace system, the *F* and *Z* has been determined by fitting data of the cooling curve which can be found in Haltshwayo [Hal10].

To remove the samples from the oven, after the oven completely cooled down and reach room temperature, the vacuum was brought down by switching off the turbo pump (i.e. high vacuum pump), still pumping with the fore pump. Argon gas was leaked into the chamber to break the vacuum completely and bring the pressure to atmospheric pressure.

5.5 Measurement conditions

The samples were characterized by RBS, Raman spectroscopy and SEM in order to investigate the migration behaviour of Ag and Sr and the structural changes of SiC before and after annealing. The measurement conditions of RBS, Raman spectroscopy and SEM are discussed in this section.

5.5.1 RBS measurement conditions

The irradiated and un-irradiated but implanted SiC samples were analysed using Rutherford backscattering spectroscopy after every annealing. The RBS spectrum of the samples was obtained using 1.6 MeV α-particles in the Van de Graaff accelerator at the University of Pretoria. Throughout this study, counts versus channel number were obtained by collecting a total charge of 8 μC per run. The sample tilt angle was kept at 5˚ while the surface barrier detector was placed at a scattering angle of 165˚ for the detection of backscattered α- particles. The analysing beam was collimated to a spot of 1mm in diameter and the beam current was

kept at 15 nA to avoid pile-up effect and overheating of the target sample. Pile-up occurs during the process of detecting backscattered particles when the time response of the detector system is not fast enough to separate the individual events in the detector due to the high rate of encountered events. Therefore, in the pile-up effect, two events may end up being recorded as one event, which will falsify the measurements by giving high current from the detector.

5.5.2 Raman spectroscopy measurement conditions

The structural changes of SiC samples as a result of ion implantation, swift heavy ion irradiation and annealing were studied using Raman spectroscopy. The resulting Raman spectra of SiC samples after ion implantation, SHIs and annealing were obtained at a visible wavelength (514.3 nm). The Raman spectrometer was a T64000 series II triple spectrometer system from HORIBA Scientific, Jobin Yvon Technology (Villeneuve d'Ascq, France). The 514.3 nm laser line of a coherent Innova® 70C series Ar^{+} laser (spot size ~ 2 µm) with a resolution of 2 cm^{-1} in the range of 200 cm^{-1} – 1800 cm^{-1} was used. The measurements were obtained in a backscattering configuration with an Olympus microscope attached to the instrument (using an LD 50x objective). The laser power was set at 1.7 mW in order to avoid sample heating. An integrated triple spectrometer was used in the double subtractive mode to reject Rayleigh scattering and dispersed the light onto a liquid nitrogen cooled Symphony CCD detector. To ensure a true representation of the irradiated and un-irradiated but implanted SiC, multiple spectra were taken at different spots on the sample.

5.5.3 SEM measurement conditions

Surface modifications of the silicon carbide samples as a result of ion implantation, SHIs and annealing were investigated by high-resolution Zeiss Ultra 55 field emission scanning electron microscopy (FESEM) at the University of Pretoria. The analysis of the surface for the irradiated and un-irradiated but implanted SiC was done with beam energy of 2 kV. In-lens SEM images of the sample were taken before implantation, after implantation, after implantation and SHI and after every heat treatment to investigate all surface changes due to these treatments. The working distance was kept between 2.2 - 3.1 mm throughout this work. Magnifications of 1µm, 10 µm and 200 nm respectively were used, and their resulting micrographs were compared.

5.6 References

[www1] http://www.physik2.uni-jena.de/inst/exphys/ionen/accessed July2014.

[Hal10] T. T. Hlatshwayo, Diffusion of silver in 6H-SiC. PhD thesis, University of Pretoria. (2010).

CHAPTER 6
RESULTS AND DISCUSSION

The effect of ion implantation and swift heavy ion (SHI) irradiation on the polycrystalline 3C-SiC structure was investigated using Raman spectroscopy, Rutherford backscattering spectrometry (RBS) and scanning electron microscopy (SEM) techniques. Silver and strontium were implanted in separate polycrystalline 3C-SiC samples. Some of these samples (i.e. SiC implanted by Ag and Sr) were irradiated with SHIs. All samples were then annealed under vacuum to temperatures above the melting point of silver and strontium. The samples before and after annealing were then analysed using RBS to study the diffusion behaviour of Sr and Ag, SEM and Raman was used to analyse the near surface structural changes induced by implantation, irradiation and annealing.

6.1 Effect of Ag ion implantation, Xe ion irradiation and annealing on the structure of polycrystalline SiC and the effect of these structures on the migration behaviour of Ag

The results in section 6.1 will be discussed in detail in subsequent sections. The effect of 360 keV Ag^+ and 167 MeV Xe^+ bombardment on silicon carbide structure was investigated using SEM and Raman spectroscopy and reported in section 6.1.1. Section 6.1.2 will discuss the effect of annealing on the structure of irradiated and un-irradiated but Ag implanted SiC. The effect of swift heavy ion irradiation and annealing on the migration behaviour of Ag in SiC will be discussed in section 6.1.3. Lastly, section 6.1.4 will compare the migration behaviour of Ag in irradiated and un-irradiated implanted SiC with the previous results.

6.1.1. Effect of Ag and Xe ions bombardment on the structure of polycrystalline SiC

Figure 6.1 (a) shows a comparison between the depth profile of 360 keV silver implanted into SiC at room temperature and the SRIM [Zie13] simulated profile. The reason for performing SRIM simulations was to compare the theoretical and experimental results and showing that the projected range (R_p) value from the experimental results is almost in agreement with that from the SRIM program.

The other reason for performing SRIM simulations was to calculate the displacement per atom (dpa) caused by Ag ion implantated in SiC at an energy of 360 keV. The ion fluence was converted into displacements per atom (dpa) using equation (6.1) below [Hal17]:

$$dpa = \frac{\frac{v_{ac}}{ion\ Å}\times 10^{8}}{\rho_c(atomscm^{-3})} \times \emptyset\ (ionscm^{-2}) \qquad (6.1)$$

where $\emptyset$ is the ion fluence, ρ_c is the theoretical atomic density of silicon carbide (9.641×10^{22} atoms/cm^3) and $\frac{v_{ac}}{ion\ Å}$ is the vacancy per ion ratio from SRIM [Zie13].

Figure 6.1 (a) shows the displacement per atom (dpa) produced as a result of Ag ion implantation at an energy of 360 keV and fluence of 2×10^{16} cm^{-2}. The SRIM simulation was carried out considering the silicon carbide density of 3.21 g/cm^3, equivalent to 9.641×10^{22} atoms/cm^3. As was discussed in chapter 3 (i.e. section 3.4), in order to extract the four moments (i.e. projected range R_p, range straggling ΔR_p, skewness γ and kurtosis β) of the experimental profile, an Edgeworth function was fitted to the as-implanted profile. A comparison between the four moments of the two Ag profiles was given in Table 3.1 showed in chapter 3. The as-implanted profile was significantly broader than the SRIM profile, as also shown by the range straggling values. The experimental projected and range straggling values for the room temperature implanted silver were 114.6 nm and 43 nm, respectively. While the R_p and ΔR_p values calculated by SRIM were 109 nm and 28 nm, respectively. There is a discrepancy between the R_p and ΔR_p values calculated by SRIM and those obtained from the experimental data. The discrepancy in the projected ranges was about 5% (the experimental R_p was larger than the one by SRIM). The two projected range values are effectively in agreement with each other because the experimental error (about 5-10%) for depth profile. The reason for the difference in the experimental and theoretical (obtained by SRIM) values can be attributed to some assumptions made in the SRIM program which were discussed in chapter 3.

Figure 6.1 (b) shows the Xe depth profile calculated by SRIM and the dpa profile due to Xe ions irradiation with energy of 167 MeV. Displacement energies of 35 and 20 eV for Si and C respectively were used in the simulation [Web04]. If one assumes the minimum dpa to cause amorphization SiC is 0.3 dpa [Web98], it is quite clear that the implantation of Ag will result in an amorphous layer of about 160 nm and that the Xe ions did not amorphized SiC. The as-implanted SiC samples were then irradiated with 167 MeV Xe ions. From Figure 6.1 (b), it is clear that the amorphous region in as-implanted SiC will be extensively exposed to large amounts of energy deposition (~20 keV/nm) due to electronic energy loss of the penetrating Xe ions.

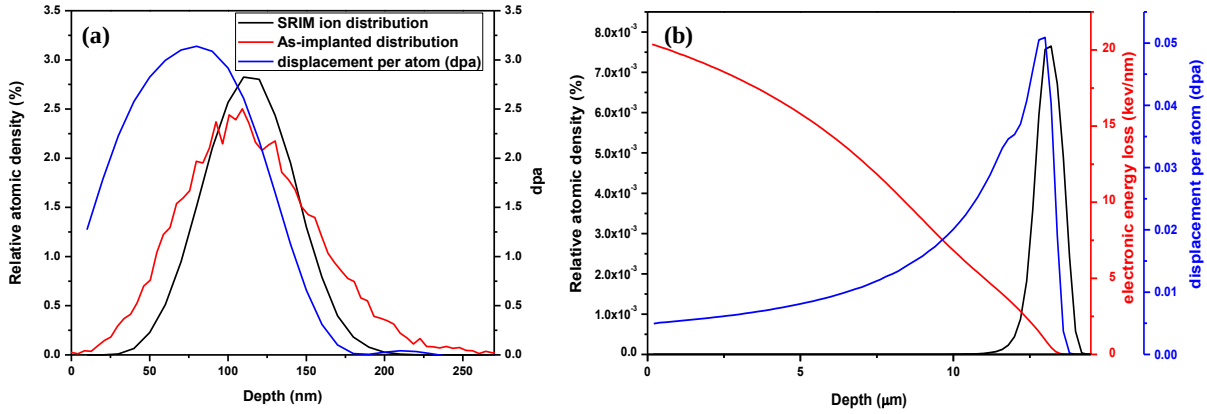

***Figure 6.1**: Depth profiles of (a) 360 keV Ag ions implanted in silicon carbide at room temperature compared with SRIM ion distribution and displacement per atom. (b) SRIM simulated profiles of Xe ions of 167 MeV irradiated into SiC, the relative atomic density is shown in black, displacement per atom (dpa) in blue and electronic energy loss in red.*

Relative atomic density shown in Figure 6.1 (a) above is the ratio of the density of silver inside SiC to the density of the SiC substrate. For this study the density of 3C-SiC was taken to be 3.21 g.cm^{-3}, equivalent to 9.641×10^{22} atoms/cm^3. The counts of Ag atoms inside SiC obtained by RBS were converted into relative atomic density (%) by first calculating the silver density inside SiC. This was achieved by taking into consideration the implanted fluence (Ø) in cm^{-2} unit, the total silver counts (*N*) in counts unit, count per channel (*dn*) in counts unit and the depth resolution (*D*) in cm/channel unit [Hal10].

$$\rho_{Ag} = \frac{\emptyset dn}{ND} \tag{6.2}$$

Thereafter the relative atomic density (RAD) % was determined by taking the ratio:

$$RAD(\%) = \frac{\rho_{Ag}}{\rho_{SiC}} \times 100 \tag{6.3}$$

where ρ_{SiC} is the atomic density of SiC (i.e. 9.641×10^{22} atoms/cm^3).

The Raman spectra of the un-implanted (virgin) SiC, 360 keV Ag implanted and SHI (i.e. 167 MeV Xe ions) irradiated samples, obtained at 514.3 nm laser wavelength are shown in Figure 6.2. For the virgin sample, sharp and well resolved peaks of the signature transverse optical (TO) (wavenumber 794 cm $^{-1}$) and longitudinal optical (LO) (wavenumber 964 cm $^{-1}$) 3C-SiC peaks at positions are observed. In addition, peaks of high wave numbers (>1000 cm^{-1}) also appear with weak intensity. Two peaks at ~1520 cm^{-1} and ~1710 cm^{-1}, respectively, are second order peaks of TO [Tal15, Win94], which further indicate the good crystalline quality

of 3C-SiC films. Implantation of Ag into the SiC at room temperature resulted in the disappearance of characteristic SiC Raman peaks between 700 to 1000 cm^{-1} and appearance of a broad peak due to Si-Si vibrations at around 510 cm^{-1}. This was accompanied by the damaged SiC band at around 800 cm^{-1} and C-C vibrations around 1425 cm^{-1}. These changes indicate the amorphization of SiC layer after Ag implantation. As shown in Figure 6.1 (a), the calculated amount of dpa due to Ag implantation is higher than the minimum dpa required to cause amorphization of SiC (i.e. 0.3 dpa), therefore amorphization of SiC was expected.

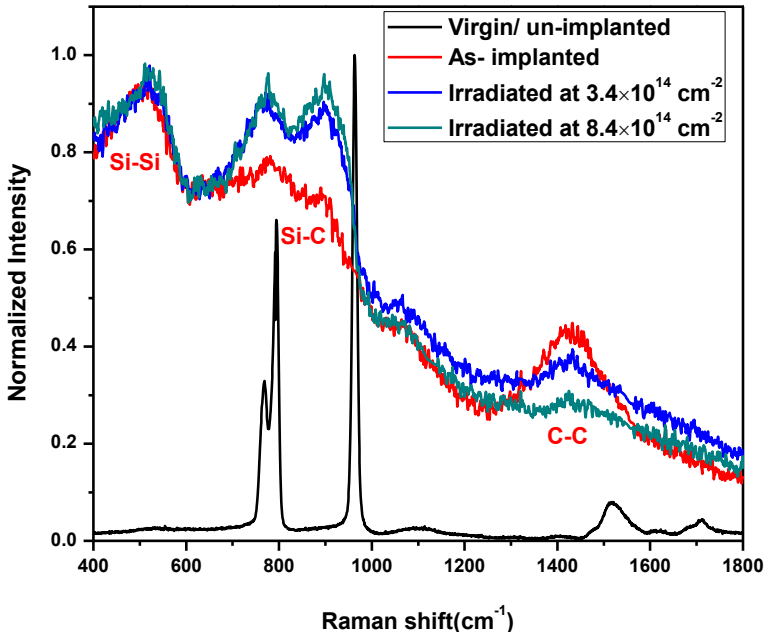

***Figure 6.2**: Raman spectra of the virgin SiC (virgin), implanted with 360 keV Ag ions (as-implanted), implanted with Ag then irradiated with 167 MeV Xe ions to fluences of 3.4×10^{14} cm^{-2} and 8.4×10^{14} cm^{-2}.*

Irradiation of Ag implanted SiC with Xe (167 MeV) ions at room temperature to fluences of 3.4×10^{14} cm^{-2} and 8.4×10^{14} cm^{-2} caused the partial reappearance of broad SiC Raman characteristic peaks at around 775 and 895 cm^{-1} with the Si-Si (around 525 cm^{-1}) and C-C (around 1433 cm^{-1}) peaks still present. The lower intensity of C-C peak for irradiated samples at 8.4×10^{14} cm^{-2} is probably due to increased absorption of the Raman scattered light which is caused by the highly damaged C-C bonds [Sor06]. This indicates that the irradiation at fluence of 8.4×10^{14} cm^{-2} caused more damage in C-C bonds. The appearance of the broad characteristic SiC peaks after Xe irradiation indicates some recrystallization of the initially amorphous SiC layer. Similar recrystallization of SiC implanted with different ions after SHIs irradiation has been reported previously [Hal15, Hal16]. This partial recrystallization of the initially

amorphous SiC layer is caused by the high electronic energy deposited by Xe ions irradiation at 167 MeV (see Figure 6.1 (b)), which induces some nucleation and growth of SiC nanocrystallites within the amorphous/damaged layer [Hal15]. During the bombardment process the SHIs transferred their energy into the target electrons which cause thermal spikes depending on the energy transferred i.e. electronic stopping power (Se). The thermal spike model in SiC layer was explained extensively before [Ben08, Deb12].

Toulemonde *et al.* [Tou00] showed that a penetrating ion induces transient lattice heating (i.e., thermal spikes), which may exceed the melting/sublimation point of the host material. This occurs mainly during swift heavy ion (SHI) irradiation events, where inelastic interactions with the host material can locally produce "hot electrons" with temperatures on the order of 10^4 K. Empirical data and models have shown that such electron temperatures couple to the atomic system to produce exceedingly high lattice temperatures [Tou06]. For SiC in particular, the recrystallization of the amorphous SiC after SHI irradiation was reported in several studies [Ben09, Zha15]. Multiple studies have demonstrated SHI-induced annealing in SiC for electronic energy depositions exceeding 10 keV/nm, and some as large as 33 keV/nm [Ben09, Bac13]. Moreover, Zhang *et al.* [Zha15], reported a threshold value of 1.4 keV/nm, whereby defect annihilation in SiC was observed. In this study, as shown in Figure 6.1 (b), the electronic energy depositions by SHI was exceeding 20 keV/nm which is much higher than the threshold value reported by Zhang [Zha15]. Therefore, the annealing of initially amorphous SiC layer resulting from the high electronic energy depositions induced by 167 MeV Xe ions, caused a partial recrystallization of this amorphous layer as shown in Figure (6.2).

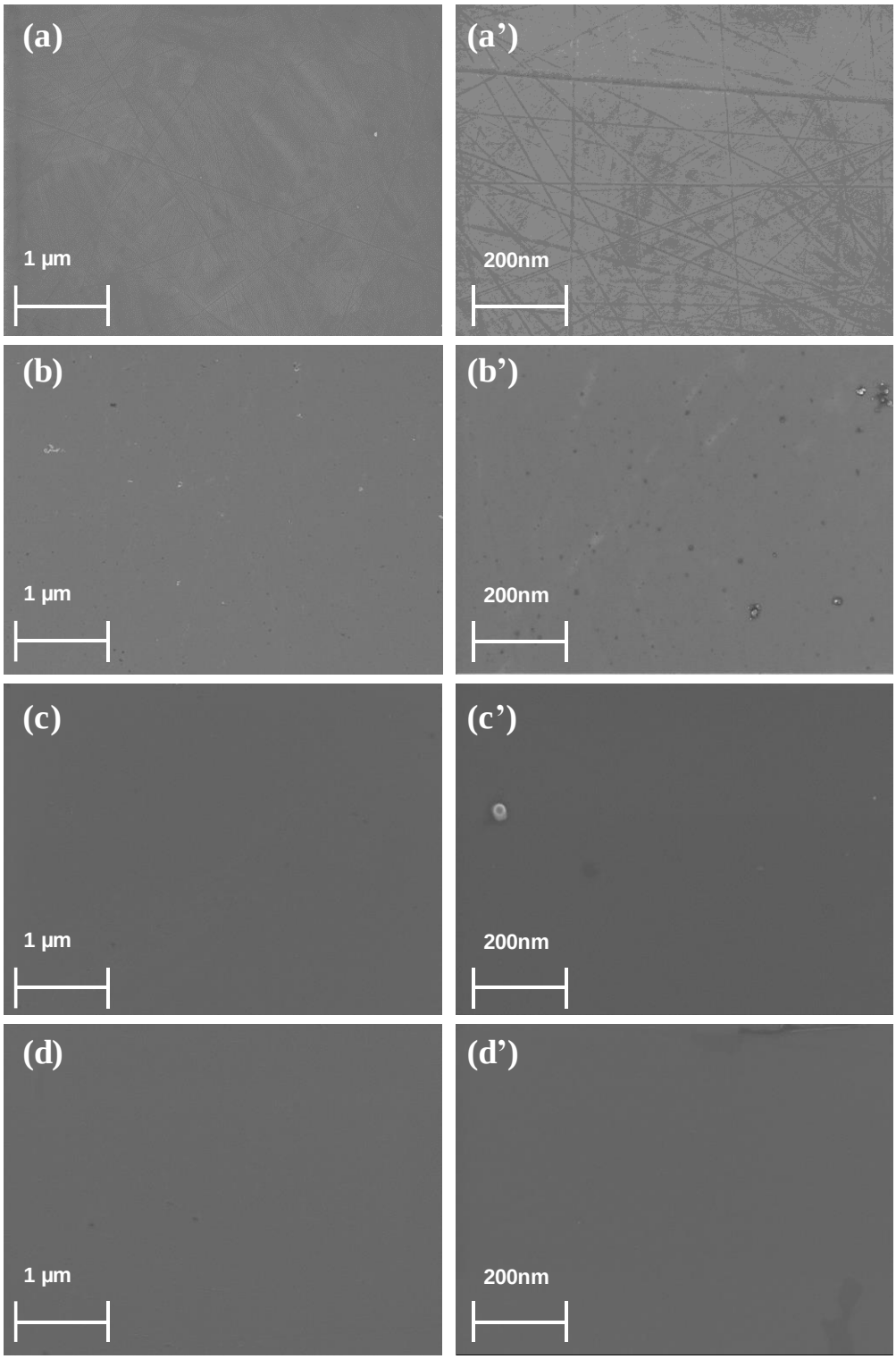

***Figure 6.3**: SEM micrographs of the SiC surface. Low magnification images of (a) the as-received, (b) as-implanted with Ag, (c) implanted with Ag then irradiated with 167 MeV Xe ions to a fluence of 3.4×10^{14} cm^{-2} and (d) implanted with Ag then irradiated with 167 MeV Xe ions to a fluence of 8.4×10^{14} cm^{-2}. (a'), (b'), (c') and (d') are the corresponding high magnifications SEM images.*

The SEM micrographs of the un-implanted, Ag implanted and irradiated Ag implanted samples are shown in Figure 6.3. The SEM image of the as-received sample showed polishing marks (Figure 6.3 (a) and (a')), which disappeared after Ag implantation at room temperature as seen in Figure 6.3 (b) and (b'). The surface of the RT as-implanted SiC was featureless compared to the virgin sample, which exhibited polishing marks. The disappearance of polishing marks in RT as-implanted SiC surface is due to swelling of the SiC caused by the formation of amorphization [Sne98]. This confirmed the amorphization of SiC as revealed by SRIM and Raman analysis in Figure 6.1 and 6.2.

Irradiating the Ag implanted samples at room temperature with Xe to fluences of 3.4×10^{14} cm^{-2} and 8.4×10^{14} cm^{-2} shows no major changes on the samples surface compared to the as-implanted as seen in Figure 6.3 (c and c') and (d and d'). As the Raman spectra for irradiated SiC samples in Figure (6.2) showed partial recrystallization of the RT as-implanted SiC, one would expect to see some crystallinity in SEM images of the irradiated SiC surface. The inability to see changes in the irradiated samples compared to as-implanted sample means that the random crystallites in irradiated samples are below the SEM detection limit.

6.1.2 Effect of annealing on the structure of SHI irradiated and un-irradiated SiC

The SHI irradiated and un-irradiated but Ag implanted samples were sequentially annealed in vacuum from 1100 to 1500 ^{o}C in steps of 100 ^{o}C. Raman spectra of the samples annealed at 1100 ^{o}C are shown in Figure (6.4). In order to analyse the obtained Raman spectra, the baseline of the spectral lines was corrected using a linear background correction. Raman spectra of the samples annealed at 1100 ^{o}C showed the reappearance of the characteristic SiC peaks which were not present before annealing – (see Figure (6.2)). The un-irradiated but Ag implanted sample showed full recrystallization (which was amorphous before annealing at 1100 ^{o}C – (see Figure (6.2)) resulting in the appearance of Raman characteristic peaks of SiC as shown in the virgin SiC – (see Figure (6.2)). This was due to the annealing out of radiation damage (i.e. radiation damage which produced by Ag implantation at room temperature) after annealing at 1100 ˚C. For the irradiated SiC samples, the transverse optical (TO) phonon mode at approximately 794 cm^{-1} and the longitudinal optical (LO) phonon mode at 964 cm^{-1} appeared in the same positions as the virgin SiC and un-irradiated but Ag implanted samples. Both irradiated samples showed poor recrystallization with a abroad Si-Si peak at about 545 cm^{-1}, the C-C peak at 1520 cm^{-1} for the sample irradiated at 3.4×10^{14} cm^{-2}, while the irradiated

sample at 8.4×10^{14} cm^{-2} showed highly disordered C-C peaks at 1100–1800 cm^{-1}. This poor recrystallization of the irradiated samples is due to the amount of impurity (i.e. concentration of Ag atoms) within the substrate (i.e. irradiated SiC) after annealing at 1100 ˚C, which will be discussed later in this section. Furthermore, the Si-Si peak at about 545 cm^{-1} in the SHI irradiated SiC samples indicate that these samples contain free silicon atoms [Ech95], which can be one of the impurities. As mentioned above Figure 6.2, before annealing, the irradiation at high fluence (i.e. at 8.4×10^{14} cm^{-2}) caused high damage in C-C bonds as compared to the irradiation at low fluence (i.e. at 3.4×10^{14} cm^{-2}) which showed less damaged C-C bonds. After annealing at 1100 ˚C, the samples irradiated up to the fluence of 3.4×10^{14} cm^{-2} showed more recovery in the damaged C-C bonds as compared to the one irradiated to fluence of 8.4×10^{14} cm^{-2}. The highly damaged C-C peaks (1100-1800 cm^{-1}) for the sample irradiated at 8.4×10^{14} cm^{-2} shown in Figure (6.4) have disappeared after further annealing at higher temperatures of 1200 ºC, 1300 ˚C and 1400 ˚C and showed one C-C peak. This was accompanied by a regular decrease in Si-Si peaks as a result of the formation of more Si-C bonds. Therefore, annealing the irradiated sample at temperatures of 1200 ºC, 1300 ˚C and 1400 ˚C caused more recovery (i.e. less defects) of the SiC crystalline structure. The SiC structure studied by Raman after annealing at 1200 ˚C, 1300 ˚C and 1400 ˚C will be discussed in more details later in this chapter.

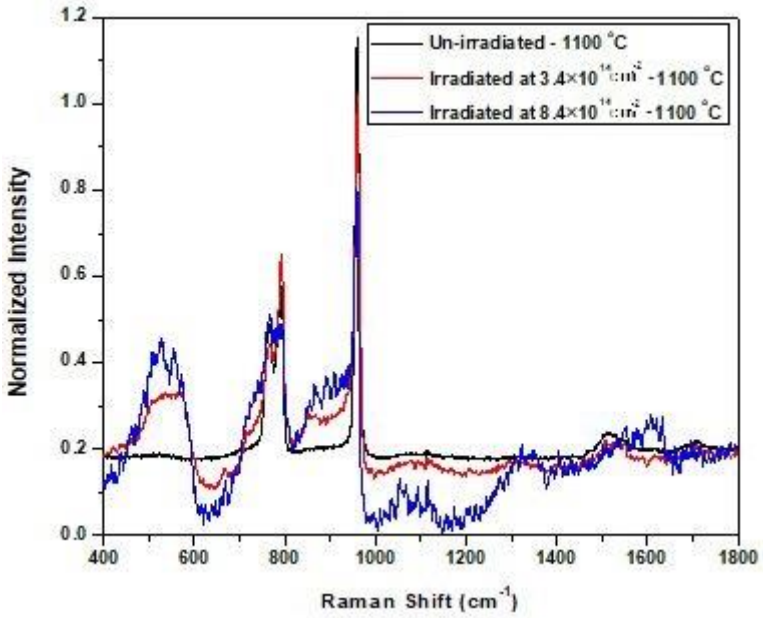

***Figure 6.4**:Raman spectra of SiC implanted with Ag at room temperature then annealed at 1100 °C (un-irradiated - 1100 ºC), implanted and then irradiated with 167 MeV Xe ions to fluences of 3.4×10^{14} cm^{-2} and 8.4×10^{14} $cm^{-2}$and finally annealed at 1100 ºC.*

Liu *et al.* [Liu10] studied the 3C–SiC nanocrystal (NC) solid films by using transmission electron microscopy (TEM) and Raman spectroscopy. They found that, as the NC average size increases, the LO phonon intensity increases in the Raman spectra (i.e. LO mode property of SiC is strongly crystal size dependent). From Figure (6.4), the LO mode of SiC for the un-irradiated but Ag implanted sample at about 964 cm^{-1} had a significantly higher intensity compared to that of the SHI irradiated samples. This suggests that the un-irradiated but Ag implanted sample has average larger crystals compared to the irradiated samples. These variations in Raman intensities were accompanied by an increase in the FWHM of the SiC Raman prominent peak (i.e. LO mode at around 964 cm^{-1}) from 9.4 cm^{-1} (virgin) to 10.6 cm^{-1} for un-irradiated but Ag implanted, 14.5 cm^{-1} and 18.8 cm^{-1} for irradiated samples to fluences of 3.4×10^{14} cm^{-2} and 8.4×10^{14} cm^{-2}, respectively. Feng *et al.* [Feg16] found that the structural defects in SiC reduced the phonon lifetime, and hence caused a broadening of phonon Raman bands. Thus, the increase in the FWHM of the SiC Raman prominent peak indicates the existence of some kind of disordering. Oiang *et al*. [Oia13] suggested that the broadening in the full width at half maximum (FWHM) of the SiC characteristic peaks is due to the decrease in crystal size of SiC. The FWHM of the un-irradiated but Ag implanted samples was narrower compared to the irradiated samples after annealing. This suggests that annealing of the un-irradiated samples at 1100 °C resulted in larger crystallites or less structural defects in SiC compared to irradiated samples. The (LO) mode in the irradiated SiC samples to a fluence of 8.4×10^{14} cm^{-2} has the lowest intensity and largest FWHM which indicates that this sample has the smallest crystal size compared to the samples irradiated to a fluence of 3.4×10^{14} cm^{-2} and un-irradiated but Ag implanted samples. This is rather surprising, since the irradiated samples had already partially recrystallized after irradiation while the un-irradiated sample (i.e. the sample implanted with Ag) was fully amorphous. Therefore, the recrystallization due to the annealing at 1100 °C in irradiated and un-irradiated but Ag implanted samples was different. This might be due to the difference in impurity concentrations (i.e. concentration of Ag atoms) in the irradiated and un-irradiated but Ag implanted samples.

The un-irradiated but Ag implanted samples retained more than 98% of Ag (i.e. from the initial Ag concentration) after annealing at 1100 ˚C. Annealing the SHI irradiated samples at 1100 ºC resulted in less Ag retention of about 58% and 46% of the implanted Ag in the irradiated samples at fluences of 3.4×10^{14} cm^{-2} and 8.4×10^{14} cm^{-2}, respectively (see Figure 6.11). As mentioned earlier, the Si-Si peak in the SHI irradiated SiC samples annealed at 1100 ˚C indicated that these samples contain free silicon atoms [Ech95]. The presence of the free Si

atoms might be one of the impurities inhibiting the recrystallization of the SHI irradiated samples. In general, impurities usually retard the recrystallization process and inhibit crystal growth [But51, Hir60]. However, it has been reported that Ag assists the recrystallization of SiC in the TRISO particle [Gen14]. In a study by Geng *et al*. [Gen14], TRISO particles that had a thin film of silver trapped between two SiC layers were used to investigate the driving force for silver migration through a SiC coating. Also, both thermodynamic calculation of the SiC–Ag system and wetting behavior of Ag on SiC have been examined to explain the chemical reaction between SiC and Ag. Their study shows that silver penetrates through the SiC coating in the TRISO particle, which was thermally treated at 1800 °C. Silver was found to wet SiC grain boundaries, and large recrystallization of SiC took place at the reaction interface between silver and SiC. Moreover, silver was found inside the newly formed SiC grains.

The results presented by Geng *et al*. [Gen14] are in agreement with our observations, where the un-irradiated but Ag implanted samples (which retained more than 98% of Ag after annealing at 1100 ˚C) showed large recrystallization SiC as compared to irradiated samples annealed in the same conditions (which show poor Ag retention – mentioned above). Since the microstructure of SiC can have an influence on the diffusion of the implanted fission products in SiC [Mal13, Hon11], studying the structure of irradiated and un- irradiated but Ag implanted SiC after annealing is very important.

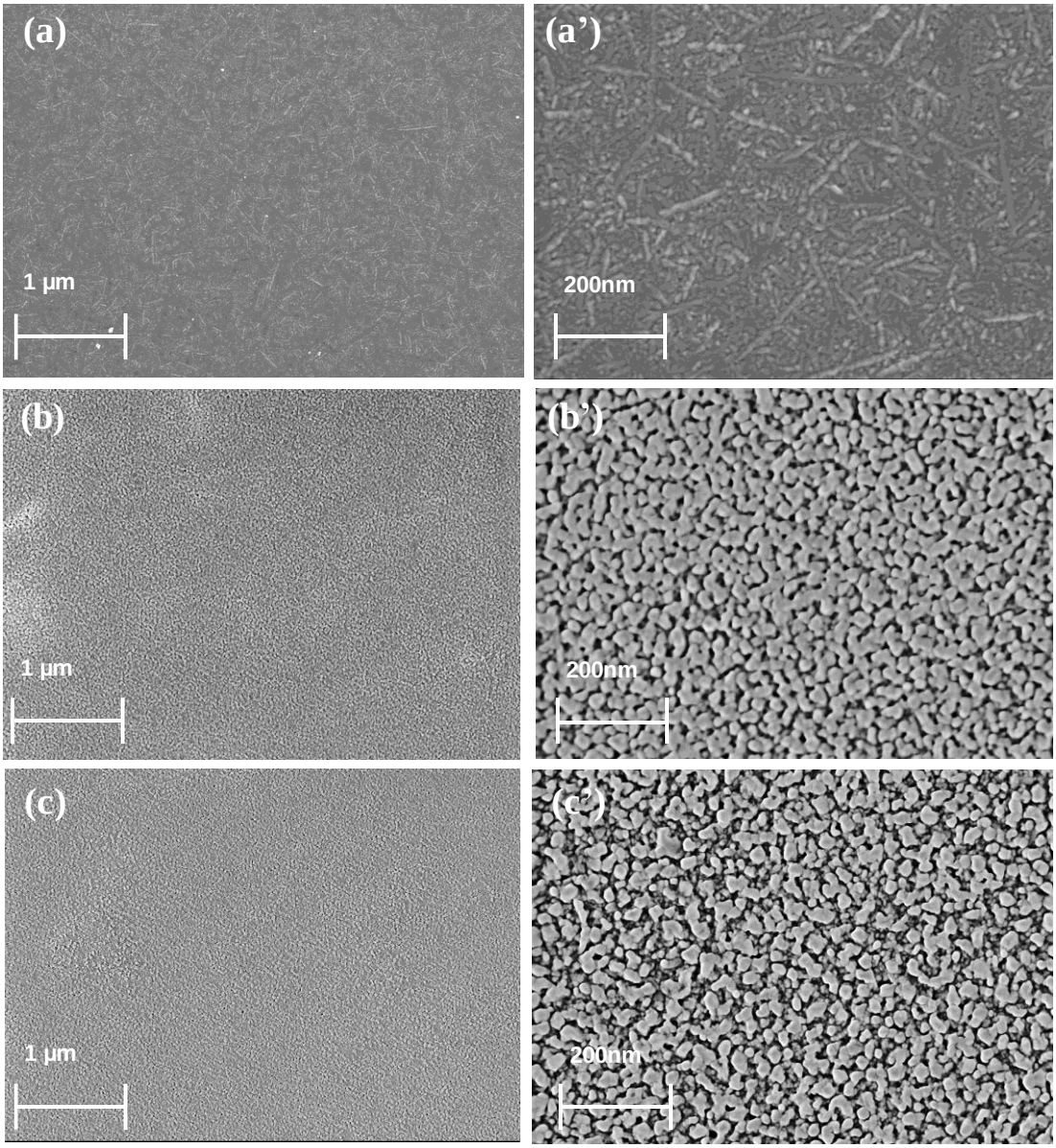

***Figure 6.5**: SEM micrographs of samples annealed at 1100 °C. Low magnification images are shown of (a) un-irradiated samples, (b) samples irradiated with 167 MeV Xe ions to a fluence of 3.4×10^{14} cm^{-2} and (c) samples irradiated with 167 MeV Xe ions to a fluence of 8.4×10^{14} cm^{-2}. The corresponding high magnification images are shown in (a'), (b') and (c').*

The crystallization observed by Raman spectroscopy in Figure 6.4 was also evident in the SEM images shown in Figure 6.5. After implantation the surfaces were featureless, as is typical of bombardment induced amorphous SiC layers – see Figure (6.3). As can be seen in Figure 6.5 (a) and (a'), annealing of the un-irradiated but Ag implanted samples resulted in long thin crystals growing in random directions. However, this micrograph also shows smaller and

randomly shaped crystals present on the surface. The surfaces of the irradiated samples (Figure 6.5 (b), (b') and (c), (c')) consisted of pores and irregular-shaped crystals. The difference in the surfaces structure between the irradiated and un-irradiated but Ag implanted samples is due to the difference in the recrystallization mentioned above. Comparison between the SEM results in Figures (6.3) and (6.5), and the Raman results in Figures (6.2) and (6.4), clearly shows that annealing the irradiated and un-irradiated but Ag implanted samples at 1100 ˚C results in recrystallization of amorphous SiC.

In this study, the average crystal sizes were determined from the SEM images in Figure (6.5) which were obtained from the irradiated and un-irradiated but Ag implanted samples, all annealed at 1100 ˚C. To ensure that the crystals were selected randomly, five straight lines were drawn randomly across the images in Figure (6.5) and the sizes of individual crystals along these lines were determined and averaged. The crystal size was measured with respect to the scale of the SEM image (i.e. 200 nm). Since the surface of un-irradiated but Ag implanted samples showed long thin crystals growing in random directions (Figure 6.5 (a), (a')), the average length and width of the long thin crystals were measured and are shown in Table (6.1). The surfaces of the irradiated samples (Figure 6.5 (b), (b') and (c), (c')) contained pores, so, the average pore sizes were also determined with respect to the scale of the SEM image (i.e. 200 nm) and shown in Table 6.1. From Table 6.1, the crystals in the un-irradiated but Ag implanted samples (i.e. long thin crystals) had an average length of about 220 nm with average width of about 40 nm. Both the irradiated samples had average crystal sizes of less than 90 nm. The samples irradiated to a fluence of 3.4×10^{14} cm^{-2} showed a larger average crystals size (i.e. 82 nm) compared to the samples irradiated to a fluence of 8.4×10^{14} cm^{-2} which had a smaller average crystals size of 59 nm. The difference in average crystal size between samples irradiated at different fluences is believed to be significant, as the +/- in the Table 6.1 refers to the distribution of the crystal sizes and not to the uncertainty in the average. The average pore size of the samples irradiated to a fluences of 8.4×10^{14} cm^{-2} (i.e. 27 nm) was little bit larger compared to the average pore size in irradiated samples at fluences of 3.4×10^{14} cm^{-2} (25 nm). The difference in average pore size between samples irradiated at different fluences is clearly not significant due to a larger uncertainty value (±16) given in Table 6.1. Comparison between the results in Table (6.1) with the Raman results (in Figures (6.4)) clearly showed that a sample irradiated to at fluence of 8.4×10^{14} cm^{-2} had smallest average crystal size after annealing at 1100 ˚C compared to the irradiated samples at fluences of 3.4×10^{14} cm^{-2} and un-irradiated but Ag implanted samples annealed in the same conditions. The differences in the average crystal

sizes between irradiated and un-irradiated but Ag implanted samples as shown in Table 6.1 could be due to the difference in the recrystallization of these samples after annealing them at 1100 ˚C as showed in Figure (6.4).

Table 6.1: *Average crystal and pores sizes determined from SEM images for irradiated and un-irradiated SiC annealed at 1100 ˚C.*

Sample	**Average crystals size (nm)**	
Un-irradiated – 1100 ˚C	**Average crystal length (nm)**	**Average crystal width (nm)**
	229±140	41±10
	Average crystal size (nm)	**Average pore size (nm)**
Samples irradiated at 3.4×10^{14} cm^{-2} – 1100 ˚C	82±38	25±16
Samples irradiated at 8.4×10^{14} cm^{-2} – 1100 ˚C	59±36	27±16

This difference in the grains size between un-irradiated and irradiated samples can be explained by the final grain size equation below [Sub98]:

$$A_G = \frac{\left[\frac{\pi}{3}\right]^{\frac{1}{3}}}{\Gamma\left[\frac{4}{3}\right]}\left[\frac{\nu_g}{\in r_n}\right]^{\frac{2}{3}} \tag{6.4}$$

where A_G is the final grain size, Γ is Euler's gamma function, ν_g is the phase growth rate and $\in r_n$ is rate of nucleation per unit amorphous area where $\in$ is the thickness of the amorphous layer and r_n is the steady-state nucleation rate. Equation 6.4 provides a quantitative relationship between grain size, nucleation, and grain growth. From this equation, it is apparent that the intuitive argument that grain growth can be maximized by minimizing the nucleation rate is correct (i.e. large grain size (A_G) will be formed when nucleation rate ($\in r_n$) is minimized). The final grain size (A_G) is inversely proportional to the rate of nucleation per unit amorphous area $\in r_n$. Since the un-irradiated but Ag implanted samples were amorphous before annealing as shown in Figure (6.2) and (6.3), the final grain size (A_G) would be larger compared to the irradiated samples which were composed of crystallites that were randomly orientated in an

amorphous matrix before annealing [Hal15, Hal16]. Therefore, these differences in the average crystal sizes were due to the fact that the initial surfaces/layers were in different states before annealing, i.e. the un-irradiated samples were amorphous while the irradiated samples were composed of crystallites that were randomly orientated in an amorphous matrix [Hal15, Hal16].

The SiC structure studied by SEM and Raman after annealing at 1200 ˚C, 1300 ˚C and 1400 ˚C will be discussed later in this chapter.

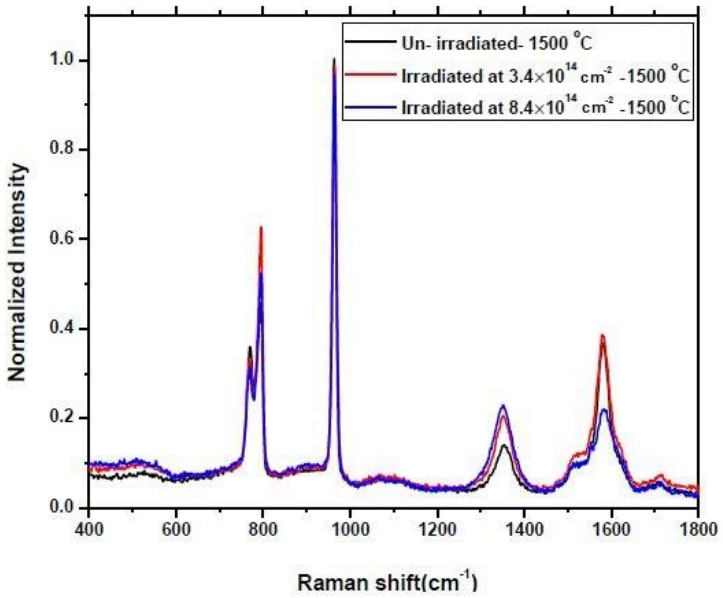

***Figure 6.6**: Raman spectra of SiC implanted with Ag at room temperature and then sequentially annealed up to 1500 °C. The spectra a the SiC samples initially implanted with Ag and then irradiated with 167 MeV Xe ions to fluences of 3.4×10^{14} cm^{-2} and 8.4×10^{14} cm^{-2} and then sequentially annealed up to 1500 °C.*

The Raman spectra of the Ag implanted SiC samples with and without SHI irradiation after sequential annealing up to 1500 ^{o}C are shown in Figure (6.6). In both the un-irradiated and irradiated samples, the two peaks appeared at 1350 and 1580 cm^{-1} corresponding to the D and G bands which are more dominant in all the carbon materials. The C-C peak at 1520 cm^{-1} (which represent the second-order Raman lines of crystalline SiC [Sor06]) in the un-irradiated and irradiated samples annealed at temperatures from 1200 to 1400 ^{o}C is still present after annealing at 1500 ˚C, but it partially merged with G peak at 1580 cm^{-1}. The presence of the D and G peaks indicates the presence of a carbon layer on the sample surfaces after annealing at 1500 ^{o}C. This result of decomposition of SiC leaving a thin carbon layer on the surface is in agreement with vacuum annealing of polycrystalline SiC at 1800 ^{o}C [Ber12]. The difference in the D and G peak intensities shown in the Raman spectra of the un-irradiated but Ag

implanted and irradiated (which implanted first then irradiated by SHI) samples after annealing at 1500 ˚C is due to the defect density in a carbon layer formed on the surfaces of these samples [Sai11]. The LO mode of SiC for the un-irradiated but Ag implanted sample at about 964 cm^{-1} had a slightly higher intensity compared to that of the SHI irradiated samples. This suggests that the un-irradiated sample has on average larger crystals compared to the irradiated samples. The FWHM of the un-irradiated but Ag implanted samples was narrower compared to the irradiated samples (10 cm^{-1} for un-irradiated but Ag implanted, 10.4 cm^{-1} and 10.6 cm^{-1} for irradiated samples to fluences of 3.4×10^{14} cm^{-2} and 8.4×10^{14} cm^{-2} respectively). Based on the discussion on Figure 6.4, this suggest that annealing the un-irradiated samples at 1500 °C resulted in larger crystallites or less structural defects in SiC compared to irradiated samples annealed under the same conditions. The difference in the average crystals size between the irradiated and un-irradiated but Ag implanted samples after annealing sequentially up to 1500 ˚C can be proven by calculating the average crystals size from the SEM images. However, it is very difficult to measure the average crystal sizes from the SEM images because these samples are mostly covered by the carbon layer after annealing at 1500 ˚C (especially for the irradiated samples at high fluence - see Figure 6.7 (c) below).

The SEM micrographs of both irradiated and un-irradiated samples after sequentially annealing up to 1500 ^{o}C are shown in Figure 6.7. The un-irradiated surface was composed of larger crystals while the irradiated was composed of finer crystals. A comparison between Figures 6.5(b') and 6.7(b') shows that the crystallites have increased in size with the increase in annealing temperature. The increase in temperature increases the mobility of atoms leading to the increase in average crystal size, in line with crystal growth theory [But51, Hir60]. Some of the crystallites were protruding more than others. Obviously, this effect was more visible on the un-irradiated samples with their larger crystals. This can be explained in terms of Wulff's law (i.e. the preferential growth of a crystal surface with a lower surface energy compared to another surface with a higher surface energy) [Wul01, Ber12].

In addition, thermal etching can play a contributing role at this temperature for all the samples [Ber12]. As can be seen from Figure 6.7 (b, b') and (c, c'), the surface morphology of the irradiated sample after annealing at 1500 °C shows fewer and smaller pores as compared to those annealed at lower temperatures (see Figure 6.5(b, b') and (c, c') and Table (6.1). The same explanations for crystal growth as used above for the un-irradiated but Ag implanted samples are applicable here. Figure 6.7(a) and (a') shows thin strands of carbon material

between the SiC crystallites and clusters with few and very small pores on the surface after annealing at 1500 °C. This carbon material on the surface of SiC after sequentially annealing up to 1500 ^{o}C was also observed in Raman and RBS spectra in Figures 6.6 and 6.8 respectively.

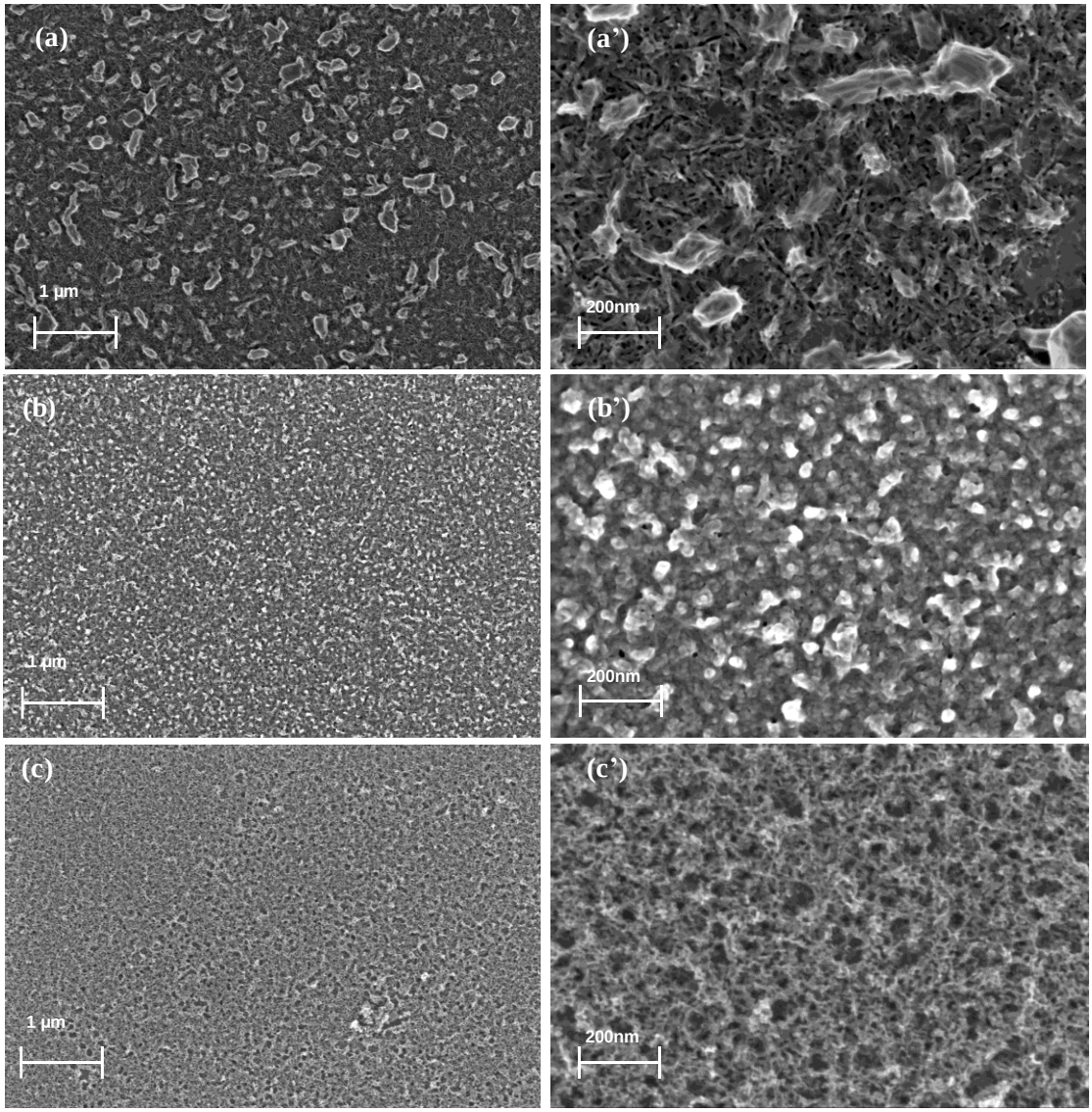

***Figure 6.7**: SEM micrographs of irradiated and un-irradiated samples after sequentially annealing up to 1500 ^{o}C, Low magnification images are shown of samples (a) un-irradiated, (b) irradiated with 167 MeV Xe ions to a fluence of 3.4×10^{14} cm^{-2} and (c) irradiated with 167 MeV Xe ions to a fluence of 8.4×10^{14} cm^{-2}. The corresponding high magnification images are shown in (a'), (b') and (c').*

Figure 6.8 shows the RBS spectra of SiC (both irradiated and un-irradiated but Ag implanted samples) after sequentially annealing from 1100 to 1500 ^{o}C for 5 hours in steps of 100 ^{o}C. The Ag peaks are not shown in the three spectra. Arrows in Figure 6.8 indicate the Si and C surface

channel positions. Spectra look the same before and after implantation, irradiation and annealing from 1100 to 1400 ^{o}C. Annealing these samples at 1500 ^{o}C resulted in the accumulation of carbon on the SiC sample surface where the RBS spectra showed a higher (than normal) count on the edge corresponding to the carbon surface. This was accompanied by the shift of the Si surface energy channel positions to lower energy channel positions indicating the presence of a carbon layer on the SiC surfaces. The free carbon on the surfaces was due to thermal decomposition of SiC causing the sublimation of silicon thus leaving a free carbon layer on the surface. The decomposition of implanted SiC layers has been reported previously [Fri09, Hal12, Ber12] to occur at temperatures above 1400°C. The decomposition of SiC observed after RBS analysis at 1500 ^{o}C correlates with Raman results (Figure 6.6) which showed the appearance of the D and G peaks at this temperature and with the SEM image shown in Figure 6.7 (a) and (a').

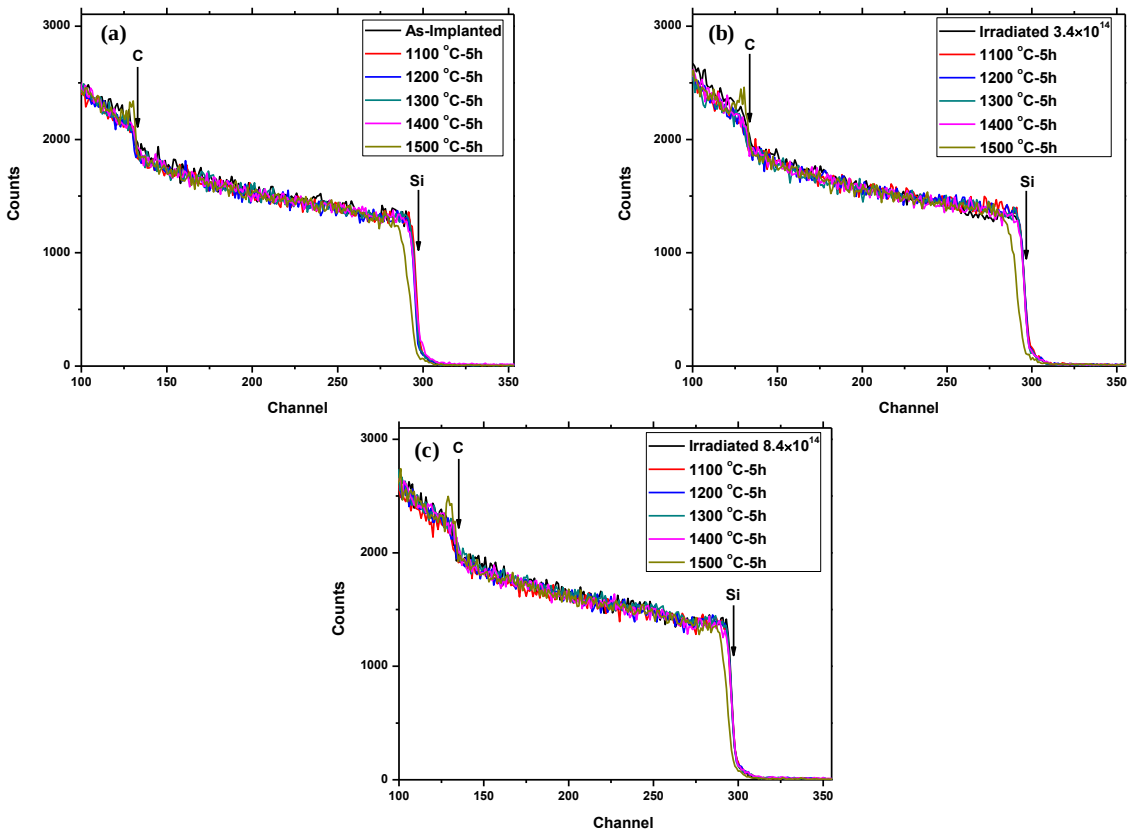

Figure 6.8: *SiC RBS spectra of irradiated and un-irradiated samples before and after sequentially annealing up to 1500 ^{o}C. (a) Un-irradiated, (b) Implanted with Ag then irradiation with 167 MeV Xe ions at room temperature to a fluence of 3.4×10^{14} cm^{-2}. (b) Implanted with Ag then irradiation with 167 MeV Xe ions at room temperature to a fluence of 8.4×10^{14} cm^{-2}.*

6.1.3. Effect of SHI irradiation on the migration behaviour of Ag in SiC

Migration behaviour of Ag implanted into SiC was investigated after irradiation and sequential annealing using RBS. As shown in Figure 6.9, no migration of implanted Ag was observed after SHI irradiation. Similar results have been reported for other implanted fission products and SHIs irradiations [Aud08, Hal15 and Hal16].

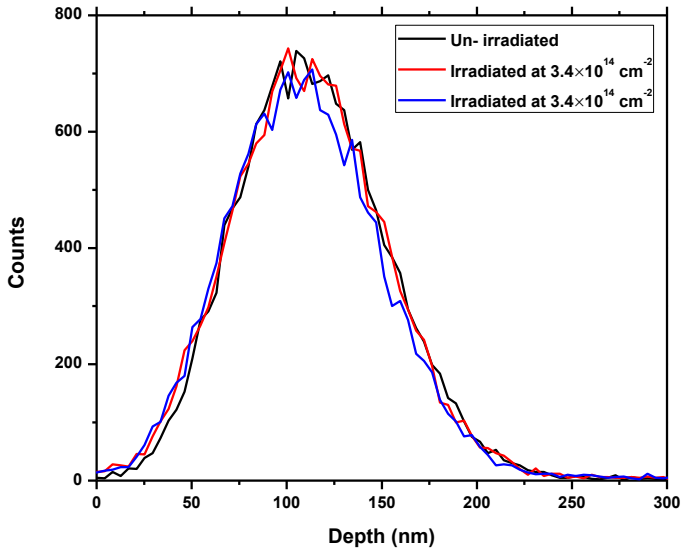

Figure 6.9: *Ag depth profile from un-irradiated and irradiated samples.*

Silver depth profiles of irradiated and un-irradiated samples after sequential annealing at temperatures ranging from 1100 to 1500 ^{o}C for 5 hours are shown in Figure 6.10. Figure 6. 11 shows the retained ratio of Ag which was calculated from the total counts/yield of Ag after annealing, divided by the counts of the as-implanted sample. From Figure 6.11, it can be observed that annealing the SHI irradiated samples at 1100 ^{o}C resulted in significant loss of about 42% and 54% of implanted Ag in both the SHI irradiated samples at fluences of 3.4×10^{14} cm^{-2} and 8.4×10^{14} cm^{-2}, respectively. This was due to the presence of pores in the surface of the SHI irradiated samples as shown in Figure 6.5 (b') and (c'). The loss of Ag through the pores in SiC have been reported in previous works [Hal12, Mac04]. The work by MacLean *et al.* indicated that silver moves through nano-pores in SiC as the possible migration path [Mac02, Mac03, Mac04]. Further loss of Ag was observed in the irradiated samples after annealing at temperatures from 1200 to 1400 ^{o}C. This was due to small pores as showed in Figure 6.13 and 6.14. The Ag peak shifted towards the surface after annealing at 1400 ^{o}C, probably due to thermal etching of the SiC surface [Hal12]. At 1500 ˚C, further loss of silver accompanied by a further shift of the Ag peak – see Figure 6.10 (b) and (c) towards the surface.

This shift is due to the thermal etching of SiC which studied by van der Berg *et al.* [Ber12] who found that the thermal etching of SiC started at 1200 °C and increase when annealed at 1500 °C.

The un-irradiated but Ag implanted samples showed small loss of Ag of about 3% (see Figure 6.11) due to the very few and small pores that appeared on the surface (see Figure 6.5 (a and a')). Therefore, the different amounts of retained silver in the irradiated and un-irradiated but Ag implanted samples after annealing at 1100 ˚C were due to the difference in surface morphology of the samples. These results agree with the work done by Kim *et al.* [Kim15] who found that Ag transport depends on the microstructure of SiC (such as SiC grain size and shape, the presence of free silicon, nano-cracks, etc.).

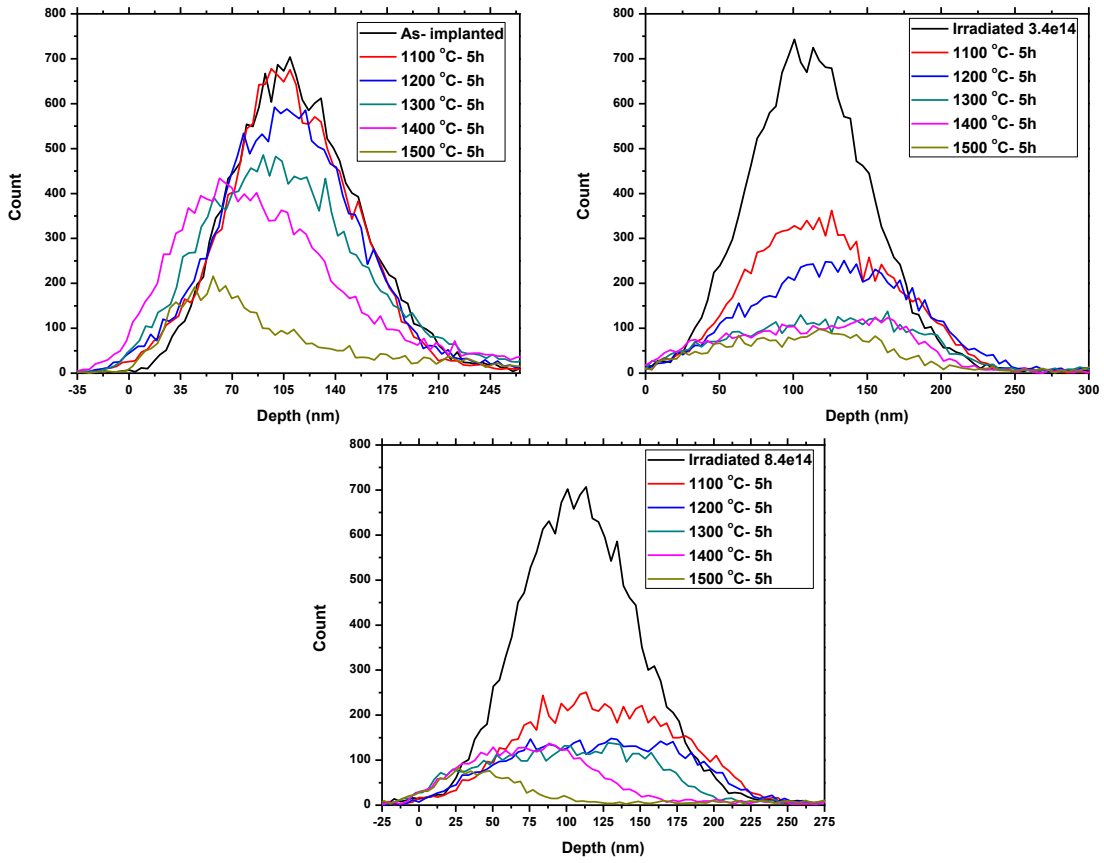

Figure 6.10: *RBS Ag depth profiles for irradiated and un-irradiated samples before and after annealing. (a) Ag depth profiles for un-irradiated samples. (b) Ag depth profiles for irradiated samples with Xe at room temperature to a fluence of* 3.4×10^{14} cm^{-2}. *(c) Ag depth profiles for irradiated samples with Xe at room temperature to a fluence of* 8.4×10^{14} cm^{-2}.

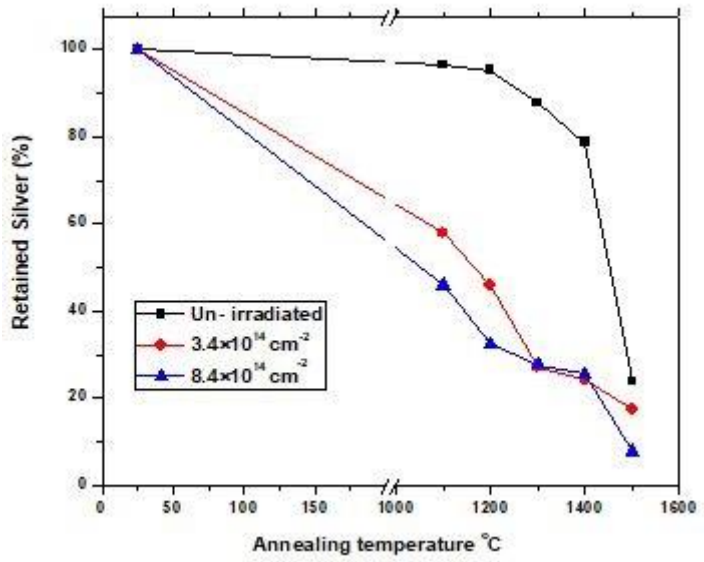

Figure 6.11: *The retained ratio of silver in irradiated and un-irradiated samples before and after sequential annealing up to 1500 ^{0}C.*

Slight migration of implanted Ag toward the surface (see Figure 6. 10(a)), accompanied by a loss of Ag (see Figure 6.11) was observed after annealing at 1100 ^{o}C for un-irradiated samples. After annealing at 1200 ^{o}C, the Ag profile in the un-irradiated but Ag implanted sample broadened and there was loss of about 5% of the Ag. Such symmetric broadening of an implanted species is characteristic of Fickian diffusion [Mal17]. This broadening became more pronounced at 1300 ^{o}C and about 12% of implanted Ag was lost from the initial Ag concentration implanted in SiC. After annealing at 1400 ^{o}C, the Ag profile peak shifted towards the surface by about 30 nm (without any broadening) from the Ag profile peak position in un-irradiated samples annealed at 1300 ˚C. This shift was accompanied by loss of about 22% of implanted Ag from the initial Ag concentration implanted in SiC due to the small pores observed on the SiC surface (see Figure 6.12 (c)). The shift of Ag profile peak after annealing at 1400 ^{o}C might be due to thermal etching of SiC. More than 76% of Ag was lost compared to as-implanted Ag concentration after annealing sequentially up to 1500 ^{o}C. The significant loss of Ag is attributed to the escape of Ag via pores in the surfaces of the un-irradiated but Ag implanted samples (see Figures 6.5, 6.7 and 6.12) aided by sublimation into the vacuum during annealing [Hal13, Mac04]. At 1500 ˚C, the shift of the silver profile towards the surface and subsequent loss of Ag is due to material (SiC) being removed from the surface (i.e. thermal etching) as a result of annealing. The Ag profile peak further shifted towards the surface by 20 nm from the Ag profile peak position in un-irradiated samples annealed at 1400 ˚C. At 1500 ˚C, the shifting of the Ag profile peak towards the surface caused an asymmetric peak. The

asymmetric peak of Ag in the sample annealed at 1500 ^{o}C (see Figure 6.10 (a)) which is due to substantial loss of silver from the SiC substrate through the surface. This will reduce the concentration on the surface side of the silver profile.

The small loss of Ag in the un-irradiated samples and the high loss of Ag in the irradiated samples after annealing at 1100 ^{o}C were due to different structures in the annealed un-irradiated and irradiated samples. Annealing the un-irradiated samples at this temperature led to the formation of rather large grains with the presence of very small pores while annealing the irradiated samples produced fine grained structures with the presence of large pores- (see Figure 6.5). The presence of large pores in the surface of the irradiated samples led in high amount of Ag loss. From these results, it is quite clear that Ag releasing is favoured in the irradiated SiC structure.

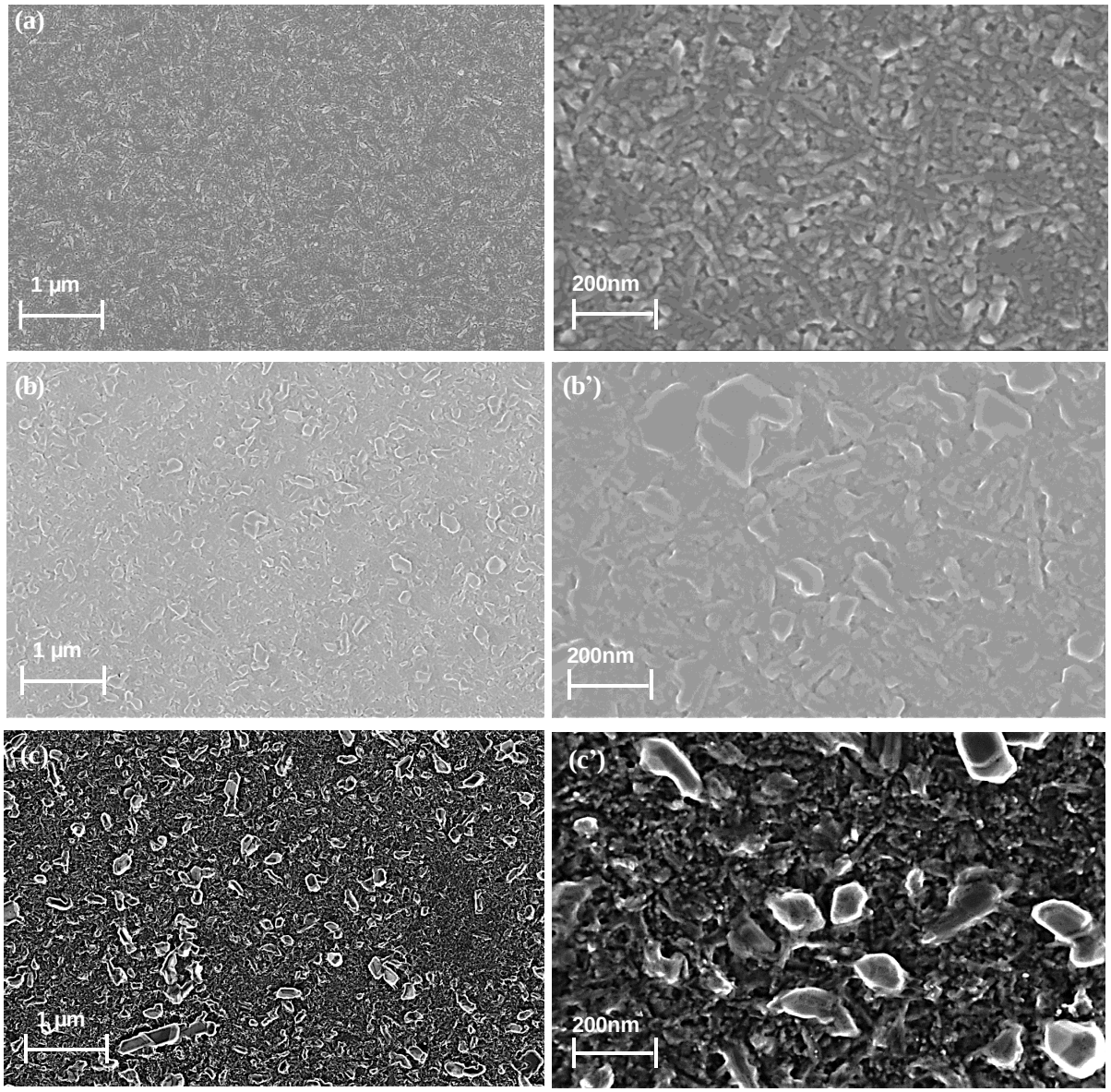

Figure 6.12: *SEM micrographs of un-irradiated samples sequentially annealed at 1200 ^{o}C, 1300 ^{o}C and 1400 ^{o}C. (a), (b) and (c) low magnification of un-irradiated samples annealed at 1200 ^{o}C, 1300 ^{o}C and 1400 ^{o}C respectively. The corresponding high magnification images are shown in (a'), (b') and (c').*

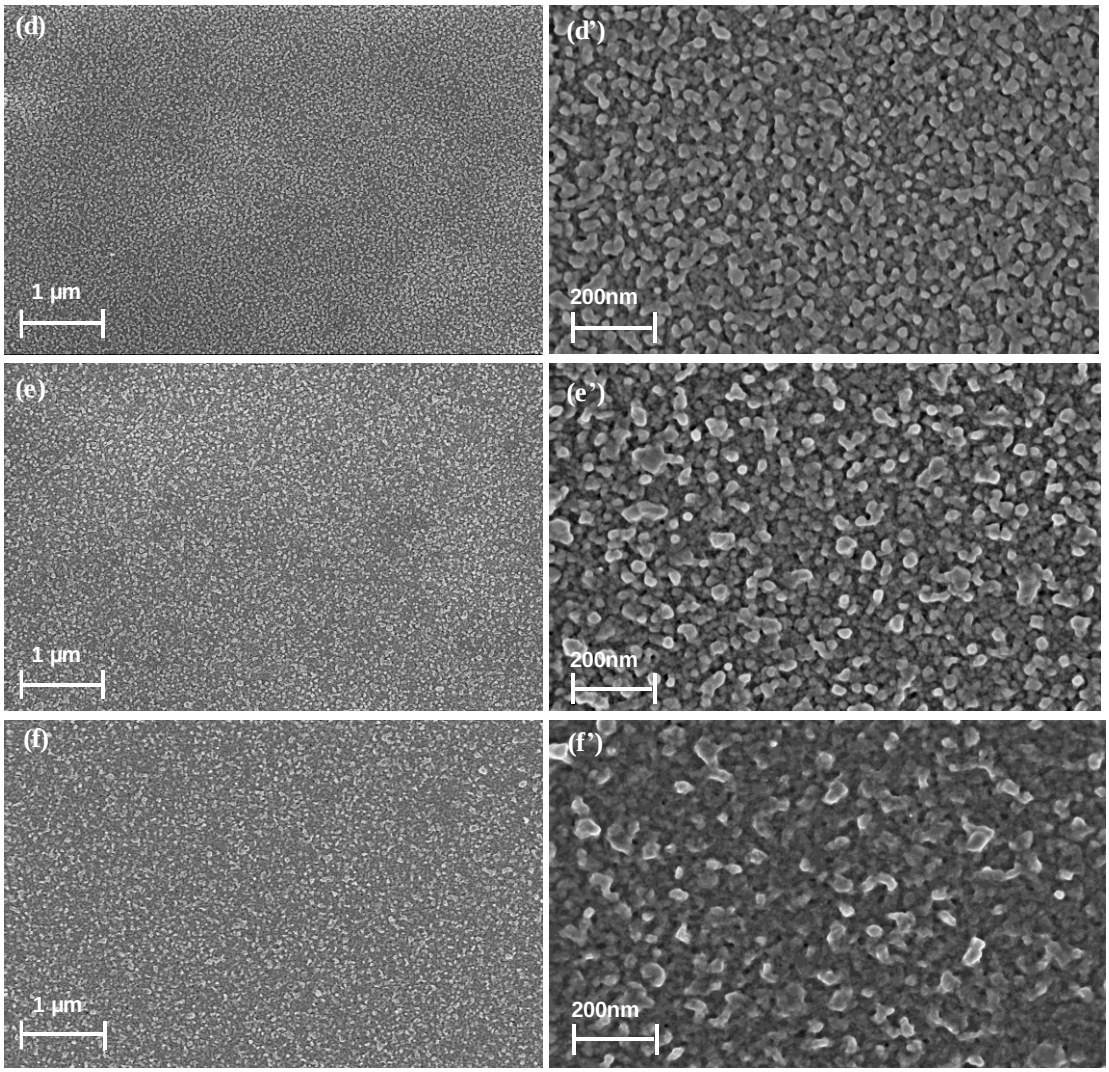

Figure 6.13: *SEM micrographs of irradiated samples at 3.4×10^{14} cm^{-2} and sequentially annealed at 1200 ^{o}C, 1300 ^{o}C and 1400 ^{o}C. (a), (b) and (c) low magnification of irradiated samples at 3.4×10^{14} cm^{-2} annealed at 1200 ^{o}C, 1300 ^{o}C and 1400 ^{o}C respectively. The corresponding high magnification images are shown in (a'), (b') and (c').*

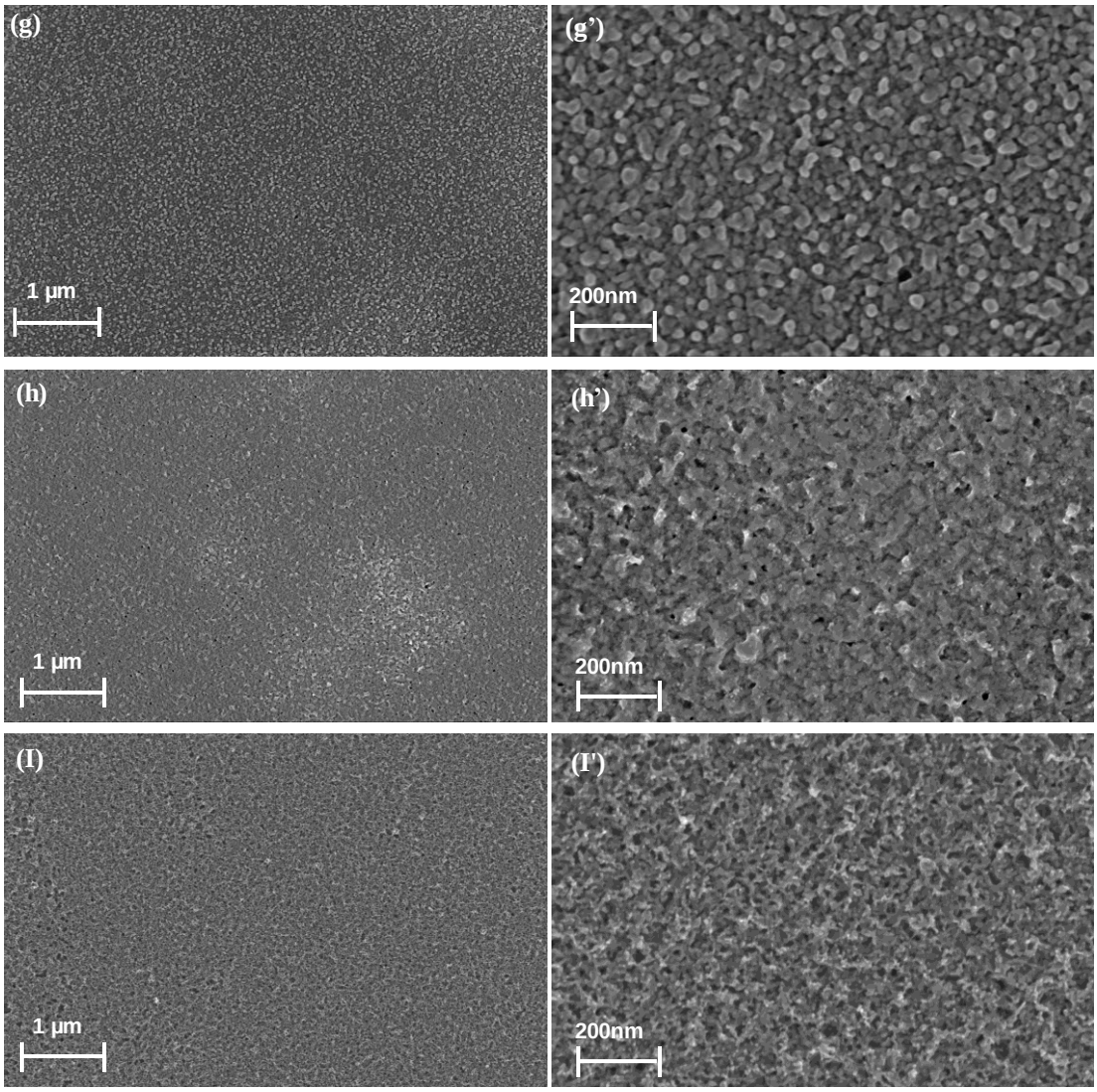

Figure 6.14: *SEM micrographs of irradiated samples at 8.4×10^{14} cm^{-2} and sequentially annealed at 1200 ^oC, 1300 ^oC and 1400 ^oC. (a), (b) and (c) low magnification of irradiated samples at 8.4×10^{14} cm^{-2} annealed at 1200 ^oC, 1300 ^oC and 1400 ^oC respectively. The corresponding high magnification images are shown in (a'), (b') and (c').*

Raman spectra of the un-irradiated and irradiated samples after sequential annealing at 1200 ^oC, 1300 ^oC and 1400 ^oC are shown in Figure 6.15 (a), (b) and (c) respectively. The Raman spectra shows further narrowing of the TO and LO modes for all the samples. This narrowing of FWHM indicates more recovery of the SiC crystalline structure is due to annealing at 1200 ^oC, 1300 ^oC and 1400 ^oC. Furthermore, the LO mode of SiC for the un-irradiated but Ag implanted sample at about 964 cm^{-1} had a significantly higher intensity compared to that of the SHI irradiated samples annealed at 1200 ^oC, 1300 ^oC and 1400 ^oC – see Figure 6.15 (a), (b)

and (c), respectively. This suggests that the un-irradiated but Ag implanted sample has an average larger crystal compared to the irradiated samples.

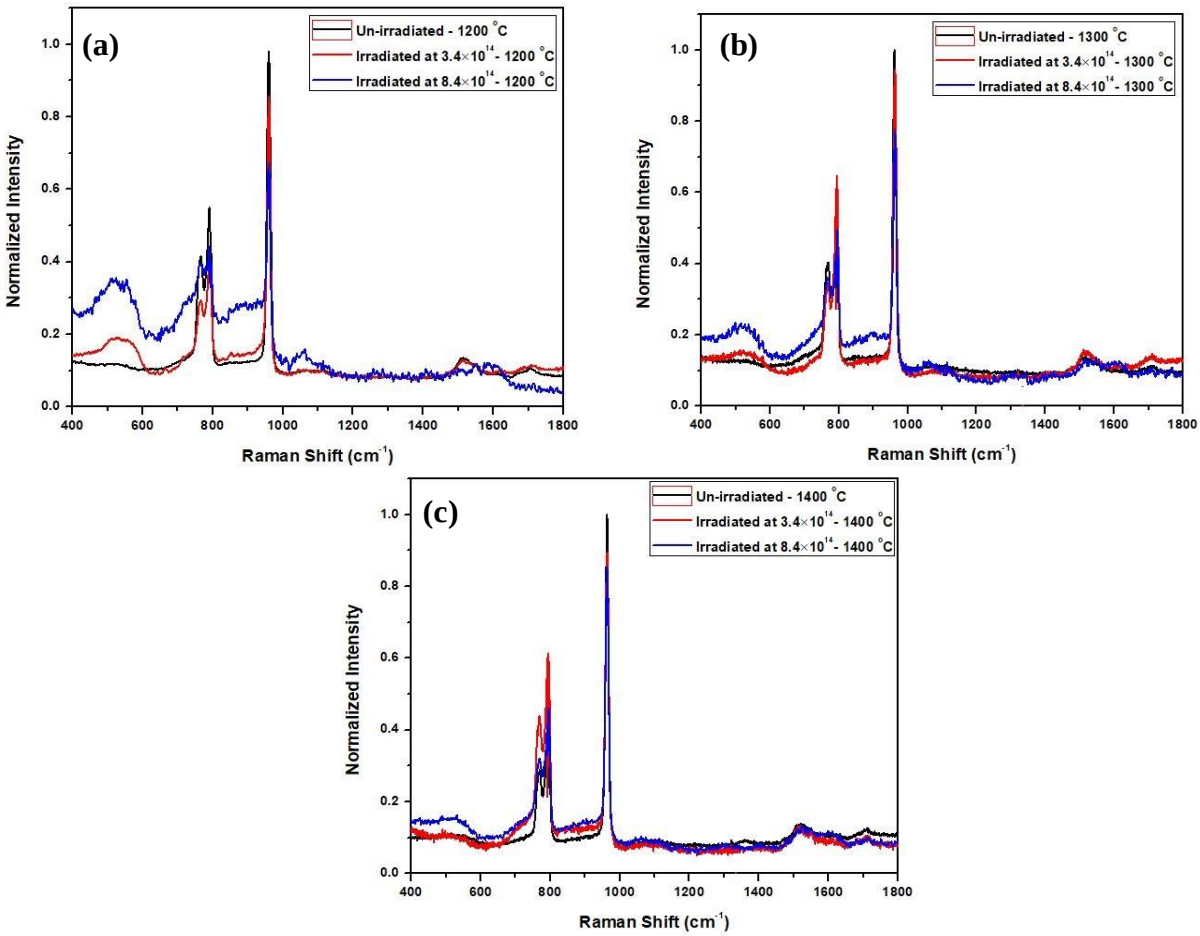

Figure 6.15: *Raman spectra of un-irradiated but Ag implanted and irradiated SiC sequentially annealed up to (a) 1200 °C, (b) 1300 °C and (c) 1400 °C.*

The average crystal sizes were determined from the SEM images in Figure 6.12, 6.13 and 6.14 which were obtained from the irradiated and un-irradiated with Ag implanted samples annealed at 1200 ˚C, 1300 ºC and 1400 ºC. Since the surface of un-irradiated but Ag implanted samples annealed at 1200 ˚C showed long thin crystals growing in random directions (Figure 6.12 (a), (a')), the average length and width of the long thin crystals were measured and reported in Table (6.2). The surfaces of the irradiated samples (Figure 6.13 and 6.14) contained pores, so, the average pore sizes were also determined with respect to the scale of the SEM image (i.e. 200 *nm*) and shown in Table 6.2. From Table 6.2, the crystals in the un-irradiated but Ag implanted samples annealed at 1200 ˚C (i.e. long thin crystals) had an average length of about 317 nm with average width of about 51 nm. The average crystals size in un-irradiated but Ag implanted samples annealed at 1200 ˚C is larger than the average crystal size in un-irradiated

but Ag implanted samples annealed at 1100 ˚C (see Table 6.1 and 6.2). The increase in annealing temperature increases the mobility of atoms leading to an increase in average crystal size, in line with crystal growth theory [But51, Hir60]. The average crystal sizes were not determined from the un-irradiated but Ag implanted samples annealed at 1300 ˚C and 1400 ºC because of the unclear crystals and presence of some crystal clusters on the surfaces – see Figure 6.12 (b) and (c).

The irradiated samples had average crystals sizes of less than 90 nm. The samples irradiated to a fluence of 3.4×10^{14} cm^{-2} showed a larger average crystal size (i.e. 86 *nm*) as compared to the samples irradiated to a fluence of 8.4×10^{14} cm^{-2} which had a smaller average crystals size of 77 nm (all annealed at 1200 ˚C). The results in Table (6.2) agrees with those obtained using Raman techniques (in Figures (6.15 (a)) which showed that the irradiated samples at fluences of 8.4×10^{14} cm^{-2} with low intensity of LO mode indicates a smaller average crystal size. After annealing at 1300 ˚C, the samples irradiated to a fluence of 3.4×10^{14} cm^{-2} showed a larger average crystals size (see Table 6.2) and high intensity for LO mode (see Figure 6.15 (b)) as compared to the samples irradiated to a fluence of 8.4×10^{14} cm^{-2} and annealed in the same conditions. Therefore, as the average crystal size increases, the LO phonon intensity increases in the Raman spectra.

Table 6.2: *Average crystal and pores sizes determined from SEM images for irradiated and un-irradiated SiC annealed at 1200 ˚C and 1300 ˚C.*

Annealing Temperatures	Un-Irradiated		Irradiated samples at 3.4×10^{14} cm^{-2}		Irradiated samples at 8.4×10^{14} cm^{-2}	
	Average crystals length (nm)	**Average crystals width (nm)**	**Average crystal size (nm)**	**Average pores size (nm)**	**Average crystal size (nm)**	**Average pores size (nm)**
1200 ˚C	317±89	51±12	86±37	22±5	77±34	21±9
1300 ˚C	-	-	88±30	22±9	84±33	20±8

6.1.4. The migration behaviour of Ag in SiC as compared to previous results

The diffusion coefficient (*D*) of Ag in irradiated and un-irradiated SiC was estimated from fitting the depth profiles (after annealing) to a solution of the Fick diffusion equation for an initially Gaussian profile [Mal17]. The diffusion coefficient of Ag in SiC was calculated for the irradiated samples annealed at 1100 ˚C and un-irradiated samples annealed from 1200 to

1300 ˚C, as shown in the Figure 6.16. The diffusion coefficients of Ag in the irradiated samples annealed from 1200 to 1500 ˚C could not be determined. This is due to the fast migration of implanted Ag out of the surface leaving a too low concentration of Ag after annealing at 1200 ˚C. Also, the diffusion coefficient of Ag was not determined in un-irradiated samples annealed at 1400 and 1500 ˚C due to asymmetric profiles (i.e. not Gaussian).

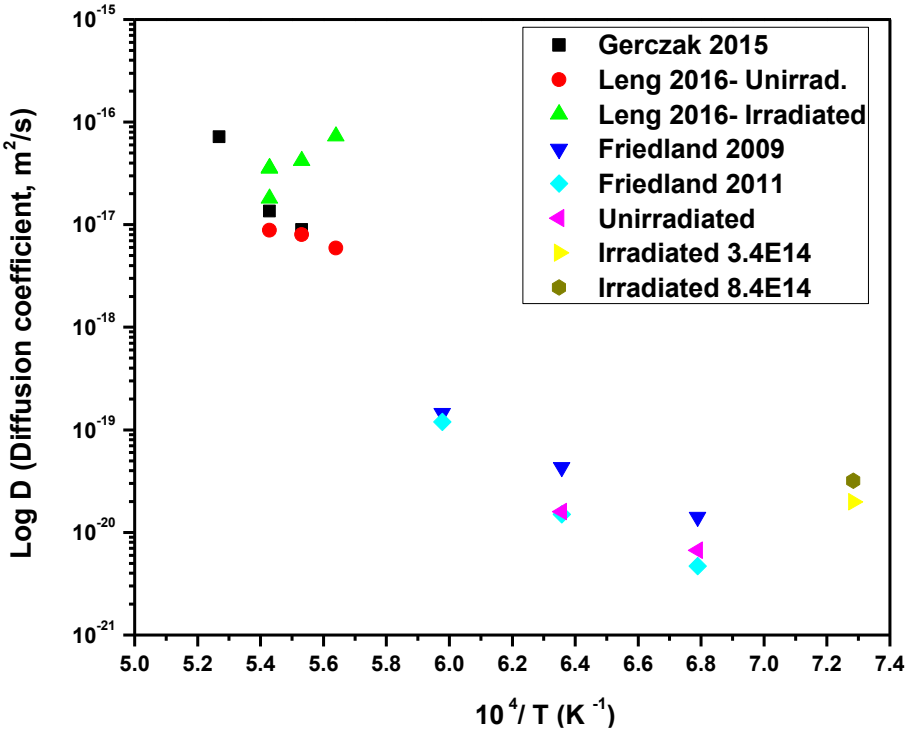

Figure 6.16: *A compilation of reported diffusion coefficients of silver implanted into polycrystalline SiC. The references of the data are given in the text.*

The diffusion coefficients determined in this study are shown in Figure 6.16 and compared with previous studies on diffusion of Ag in SiC [Fri09, Fri11, Ger15 and Len16]. The diffusion coefficients of 6.7×10^{-21} m^2/s and 1.6×10^{-20} m^2/s were obtained for the un-irradiated but Ag implanted sample after annealing at temperatures of 1200 ˚C and 1300 ˚C respectively, for 5 hours. These data agree with the work of Friedland and co-workers [Fri11]. The authors investigated the diffusion of silver in polycrystalline 3C-SiC and reported the diffusion coefficients of Ag after annealing at the temperatures of 1200, 1300 and 1400 °C was 4.7×10^{-21} m^2/s, 1.5×10^{-20} m^2/s and 1.2×10^{-19} m^2/s, respectively. The agreement in our work with Friedland's [Fri11] is reflecting the same mechanism of diffusion which is the grain boundary diffusion as described by Fickian diffusion equation adapted in Malherbe code [Mal17] used to calculate diffusion coefficient in this study. The effect of swift heavy ion irradiation was evident as the diffusion coefficients obtained for the irradiated sample is higher than the un-

irradiated but Ag implanted sample. At 1100 ˚C, the irradiated samples at fluences of 3.4×10^{14} cm^{-2} and 8.4×10^{14} cm^{-2} has diffusion coefficients of 2×10^{-20} m^2/s and 3.2×10^{-20} m^2/s, respectively. However, after annealing at 1100 ˚C, there was no determinable diffusion coefficient for Ag in un-irradiated but Ag implanted samples. The two sets of data reported by Leng *et al*. [Len16] are particularly interesting in the context of this study. They investigated the diffusion of 400 keV Ag^+ implanted at 300 °C to a fluence of $5\times10^{14}cm^{-2}$. Some of the implanted samples were pre-irradiated at 950 °C with 3.15 MeV C^{+2} ions to a fluence of 1.1×10^{17} cm^{-2} and the diffusion coefficients for the irradiated and un-irradiated but implanted samples were also measured. This temperature of 950 °C is above the threshold amorphization temperature for SiC bombarded with heavy ions in the energy range of 100 – 400 keV [Mal13]. As can be seen from Figure 6.16, diffusion coefficients for the latter samples were also higher than the Ag implanted samples (i.e. un-irradiated samples). This is in agreement with the results of this study and indicates that bombardment with swift heavy ions enhances the diffusion of Ag in SiC.

6.2 Effect of Sr ion implantation, Xe ion irradiation and annealing on the structure of polycrystalline SiC and the effect of these structures on the migration behaviour of Sr

The results in section 6.2 will be discussed in detail in subsequent sections. The effect of 360 keV Sr^+ and 167 MeV Xe^+ bombardment on silicon carbide structure was investigated using SEM and Raman spectroscopy and reported in section 6.2.1. Section 6.2.2 will discuss the effect of annealing on the structure of irradiated and un-irradiated SiC implanted with Sr. Lastly, the effect of swift heavy ion irradiation and annealing on the migration behaviour of Sr in SiC was investigated using RBS and discussed in section 6.2.3.

6.2.1. Effect of Sr and Xe ions bombardment on the structure of polycrystalline SiC

Figure 6.17 (a) shows a comparison between the 360 keV strontium implanted depth profile and the SRIM [Zie13] simulated profile. The as-implanted profile in Figure 6.17 (a) is slightly broader than the SRIM profile, as also shown by the range straggling values. The experimental projected and straggling range for strontium implanted into SiC at room temperature were 146 nm and 40 nm, respectively. While the R_p and ΔR_p values for Sr implanted into SiC calculated by SRIM were 138 nm and 38 nm, respectively. The difference in the projected range was about 5% (the experimental R_p was larger than the one by SRIM). Also, the discrepancy in the straggling range was about 5%. The projected and straggling ranges calculated by SRIM and

the one obtained from the experimental data are effectively in agreement with each other because the experimental error (about 5-10%) for depth profile.

Figure 6.17 (a) also shows the displacement per atom (dpa) produced as a result of Sr ion implantation at an energy of 360 keV and fluence of 2×10^{16} cm^{-2}. The dpa was calculated by using equation (6.1). Figure 6.17 (b) shows the Xe depth profile calculated by SRIM and the dpa profile due to Xe ions irradiation with energy of 167 MeV. Displacement energies of 35 and 20 eV for Si and C respectively were used in the simulation [Web04]. Assuming that the minimum displacement per atom (dpa) of about 0.3 dpa is enough to amorphize SiC [Web98], it is quite clear that implantation of Sr will result in an amorphous layer of about 205 nm from the surface and that the Xe ions did not amorphize SiC. The as-implanted SiC samples were then irradiated with 167 MeV Xe ions. From Figure 6.17 (b), it's clear that the amorphous region in the as-implanted SiC will be extensively exposed to large amounts of energy deposition (~20 keV/ nm) due to electronic energy loss of the penetrating Xe ions. This SRIM simulation will help in the explanation of the Raman results in Figure (6.18) below.

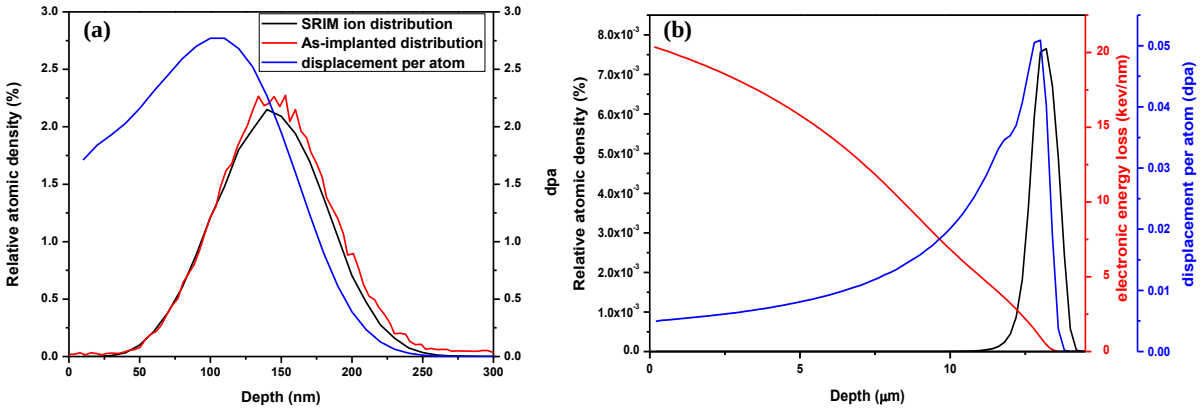

Figure 6.17: *Depth profiles of (a) 360 keV Sr ions implanted in silicon carbide at room temperature compared with SRIM ion distribution and displacement per atom. (b) SRIM simulated profiles of Xe ions of 167 MeV irradiated into SiC, the relative atomic density is shown in black, displacement per atom (dpa) in blue and electronic energy loss in red.*

Relative atomic density shown in Figure 6.17 above is the ratio of the density of strontium inside SiC to the density of the SiC substrate. For this study the density of 3C-SiC was taken to be 3.21 $g.cm^{-3}$, equivalent to 9.641×10^{22} $atoms/cm^3$. The counts of Sr atoms inside SiC obtained by RBS were converted into relative atomic density (%) by first calculating the silver

density inside SiC. This was achieved by taking into consideration the implanted fluence (φ) in cm^{-2} unit, the total strontium counts (*N*) in counts unit, count per channel (*dn*) in counts unit and the depth resolution (*D*) in cm/channel unit.

$$\rho_{Sr} = \frac{\varphi dn}{ND} \tag{6.5}$$

Thereafter the relative atomic density (RAD) % was determined by taking the ratio:

$$RAD(\%) = \frac{\rho_{Sr}}{\rho_{SiC}} \times 100 \tag{6.6}$$

where ρ_{SiC} is the atomic density of SiC (i.e. 9.641×10^{22} atoms/cm^3)

The Raman spectra of the SiC surface after Sr implantation and after SHI irradiation to different fluences are shown in Figure 6.18 where the un-implanted (virgin) sample has been included for comparison. The Raman spectrum of the un-implanted SiC shows the characteristic main Raman peaks of SiC which discussed in a previous section (see Figure 6.2). Implantation of Sr into SiC at room temperature resulted in the disappearance of the characteristic SiC Raman peaks (i.e. the transverse optical (TO) phonon mode at approximately 794 cm^{-1} and the longitudinal optical (LO) phonon mode at 964 cm^{-1}) and the appearance of a broad peak due to Si-Si vibrations at around 525 cm^{-1}. This was accompanied by the damaged SiC band at around 800 cm^{-1} and C-C vibrations at around 1425 cm^{-1}. These changes indicate the amorphization of the near surface region of the SiC substrate after Sr implantation. As shown in Figure 6.17 (a), the calculated amount of dpa due to Sr implantation is higher than the minimum dpa required to cause amorphization SiC (i.e. 0.3 dpa), therefore amorphization of SiC was expected.

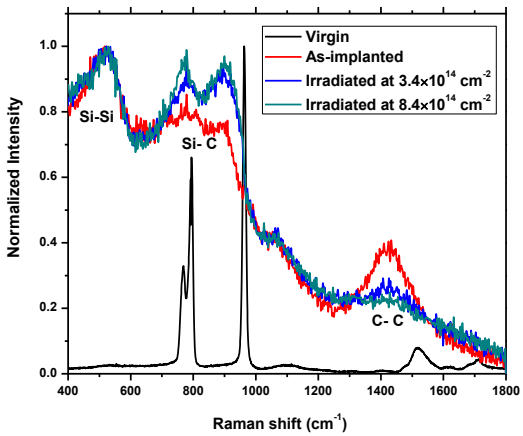

***Figure 6.18**: Raman spectra of the virgin SiC (virgin), implanted with 360 keV Sr ions (as-implanted), implanted with Sr then irradiated with 167 MeV Xe ions to fluences of 3.4×10^{14} cm^{-2} and of 8.4×10^{14} cm^{-2}.*

Irradiation of the implanted SiC with Xe (167 MeV) ions at room temperature to fluences of 3.4×10^{14} cm^{-2} and 8.4×10^{14} cm^{-2} caused the partial reappearance of broad SiC characteristic Raman peaks at around 780 and 900 cm^{-1} with the Si-Si (around 525 cm^{-1}) and C-C (around 1425 cm^{-1}) peaks still present. The appearance of broader characteristic SiC peaks indicates some limited recrystallization of the initially amorphous SiC layer. Similar recrystallization of SiC implanted with different implanted ions after SHIs irradiation has been reported previously [Hal15, Hal16]. In those previous studies, transmission electron microscopy (TEM) and Raman spectroscopy were used to study the structural changes of the as-implanted SiC after SHIs irradiation. They found that, the recrystallization of the initially amorphous SiC was due to SHI irradiation causing the formation of randomly oriented crystallites embedded in amorphous SiC. The similarities of the reported Raman results with our current Raman results suggest that our irradiated amorphous SiC layer was also composed of randomly oriented crystallites embedded in amorphous SiC.

Figure 6.19 (a) and (a') shows SEM micrographs of the as-received (i.e. un-implanted) SiC wafer. The surface had only some polishing marks (labelled P) observed on it. Figure 6.19(b and b') shows the as-implanted SiC surface (un-irradiated). The as-implanted sample surface was featureless apart from some dirt (bubbles) with the polishing marks (less pronounced). The reduction in the visibility of polishing marks in RT as-implanted SiC surface is due to swelling of the SiC which occurred by amorphization [Sne98]. This result is in agreement with SRIM and Raman analyses in Figure 6.17 and 6.18 respectively. The polishing marks are faintly visible in both the irradiated samples (to a fluence of 3.4×10^{14} cm^{-2} and 8.4×10^{14} cm^{-2}) shown in Figure 6.19 (c and c') and (d and d') respectively. As the Raman spectra for irradiated SiC samples in Figure (6.18) showed partial recrystallization of the RT as-implanted SiC, one would expect to see some crystallinity in SEM images of the irradiated SiC surface. The inability to see changes in the irradiated samples compared to as-implanted sample means that the random crystallites in irradiated samples are below the SEM detection limit.

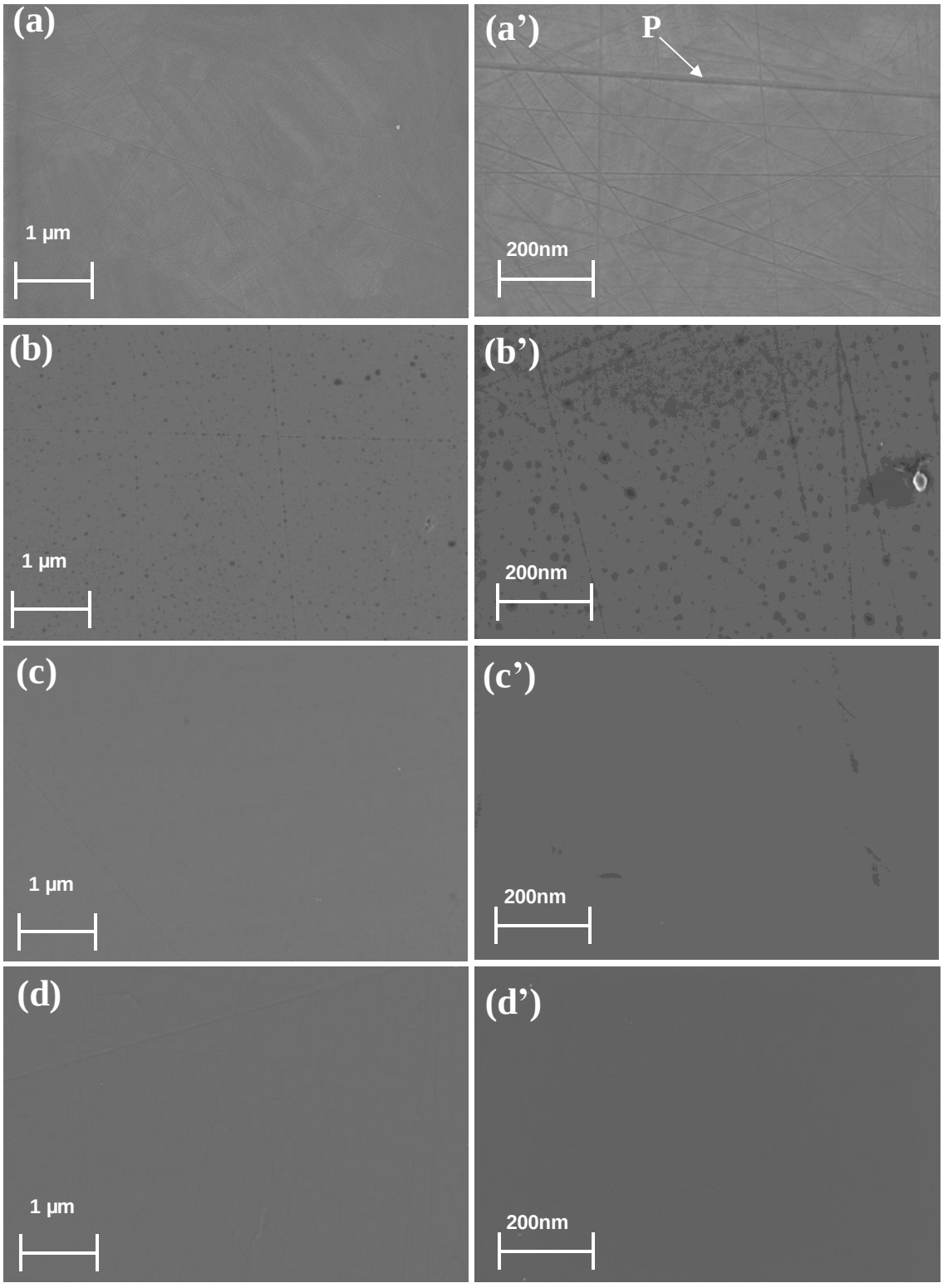

Figure 6.19: *SEM micrographs of the CVD-SiC surface. Low magnification images of (a) the as-received, (b) as-implanted with Sr, (c) implanted with Sr then irradiated with Xe ions to a fluence of 3.4×10^{14} cm^{-2} and (d) implanted with Sr then irradiated with Xe ions to a fluence of 8.4×10^{14} cm^{-2}. (a'), (b'), (c') and (d') are the corresponding high magnifications SEM images.*

6.2.2 Effect of annealing on the structure of irradiated and un-irradiated SiC

Raman spectra of irradiated and un-irradiated but Sr implanted samples after annealing at 1100 ^{o}C are shown in Figure 6.20. In order to analyse the Raman spectra obtained, the baseline of the spectral lines was corrected using a linear background correction. Annealing the samples at 1100 ^{o}C resulted in the reappearance of Raman characteristic peaks of SiC. The un-irradiated but Sr implanted samples fully recrystallized resulting in the disappearance of Si-Si and C-C peaks. The irradiated samples poorly recrystallized resulting in the appearance of Raman SiC characteristic peaks with a broad Si-Si peak (at about 545 cm^{-1}) and a C-C peak (at 1520 cm^{-1}) still present.

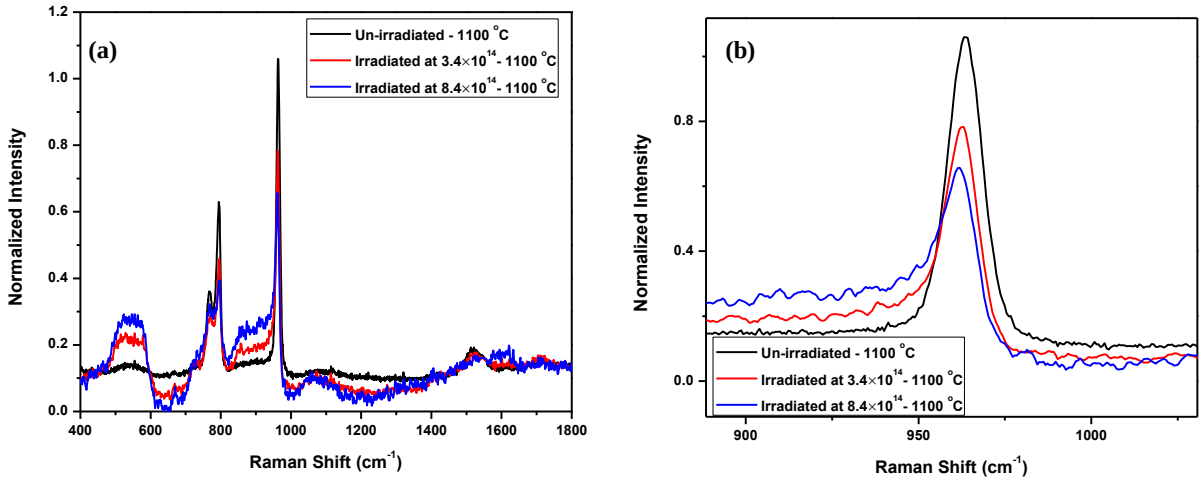

Figure 6.20: *(a) Raman spectra of SiC implanted with Sr at room temperature and annealed at 1100 °C (un-irradiated - 1100 °C), implanted and then irradiated with Xe (167 MeV) ions to fluences of 3.4×10^{14} cm^{-2} and 8.4×10^{14} cm^{-2} and finally annealed at 1100 °C, (b) longitudinal optic (LO) phonon peaks for all samples.*

Un-implanted (i.e. virgin) SiC gives Raman scattering from a transverse optic (TO) phonon at approximately 794 cm^{-1} and a longitudinal optic phonon (LO) at 964 cm^{-1} (see Figure 6.18). At 1100 ^{o}C, the observed TO and LO peaks positions for un-irradiated sample were in the same positions as those of the virgin SiC. For the SHI irradiated samples, it can be observed that two distinct TO and LO peaks of SiC were both quite broad and had lower intensities compared to the un-irradiated but Sr implanted samples. Feng *et al.* [Feg16] found that the structural defects in SiC reduced the phonon lifetime, and hence caused a broadening of phonon Raman bands.

Thus, the increase in the FWHM indicates the existence of some kind of disordering. Furthermore, Oiang *et al*. [Oia13] suggest that the broadening in the full width at half maximum (FWHM) of the SiC characteristic peaks is due to the decrease in crystal size of SiC. From Figure (6.20), the LO mode of SiC for the un-irradiated but Sr implanted sample at about 964 cm^{-1} had a significantly higher intensity compared to that of the SHI irradiated samples. This suggests that the un-irradiated sample has on average larger crystals compared to the irradiated samples. The LO phonon at 964 cm^{-1} shifted down to 962 cm^{-1} and 961 cm^{-1} for the samples irradiated to fluences of 3.4×10^{14} cm^{-2} and 8.4×10^{14} cm^{-2} respectively, which was probably due to the tensile stress caused by the defects in lattice atoms [Wen12]. Generally, the tensile stress increases with decreasing the grain size [Sch91]. Richter *et al.* [Ric81] suggested that the phonon confinement model is correlated to the observed changes in the crystal size. They also found that the shift in the Raman peaks toward lower wavenumbers is due to the small crystal size in the investigated material. Therefore, for irradiated samples, shift in the LO Raman peaks towards lower wavenumbers is due to the small crystallites which formed within the amorphous region of SiC. A larger shift toward lower wavenumbers appeared in the irradiated sample to a higher fluence (8.4×10^{14} cm^{-2}) indicating smaller crystallites as shown in Figure 6.20(b). These variations in Raman peak shifts were accompanied by an increase in the full width at half maximum (FWHM) of the SiC Raman prominent peak (i.e. LO mode) from 9.4 cm^{-1} (virgin) to 11.6 cm^{-1} for un-irradiated, 11.8 cm^{-1} and 19.6 cm^{-1} for irradiated samples at fluences of 3.4×10^{14} cm^{-2} and 8.4×10^{14} cm^{-2} respectively. The FWHM of the un-irradiated sample was narrower compared to the irradiated samples. This confirms that annealing the un-irradiated but Sr implanted samples at 1100 °C resulted in larger crystallites compared to irradiated samples annealed in the same conditions. This is rather surprising, since the irradiated samples had already partially recrystallized after irradiation while the un-irradiated sample was fully amorphous. Therefore, the recrystallization in these samples are different. This is due to the difference in impurity concentrations in the irradiated and un-irradiated but Sr implanted samples.

Annealing the un-irradiated but Sr implanted samples at 1100 ^{o}C resulted in poor Sr retention of about 75%. SHI irradiated samples retained more than 97% of Sr (i.e. from the initial Sr concentration) after annealing at 1100 ˚C. In general, impurities can usually retard the recrystallization process and inhibit crystal growth [But51, Hir60]. The impurity can be Sr. The irradiated samples (which retained more than 97% of Sr after annealing at 1100 ˚C) showed

poor recrystallization compared to the un-irradiated but Sr implanted samples annealed at same conditions (which shows poor Sr retention – mentioned above).

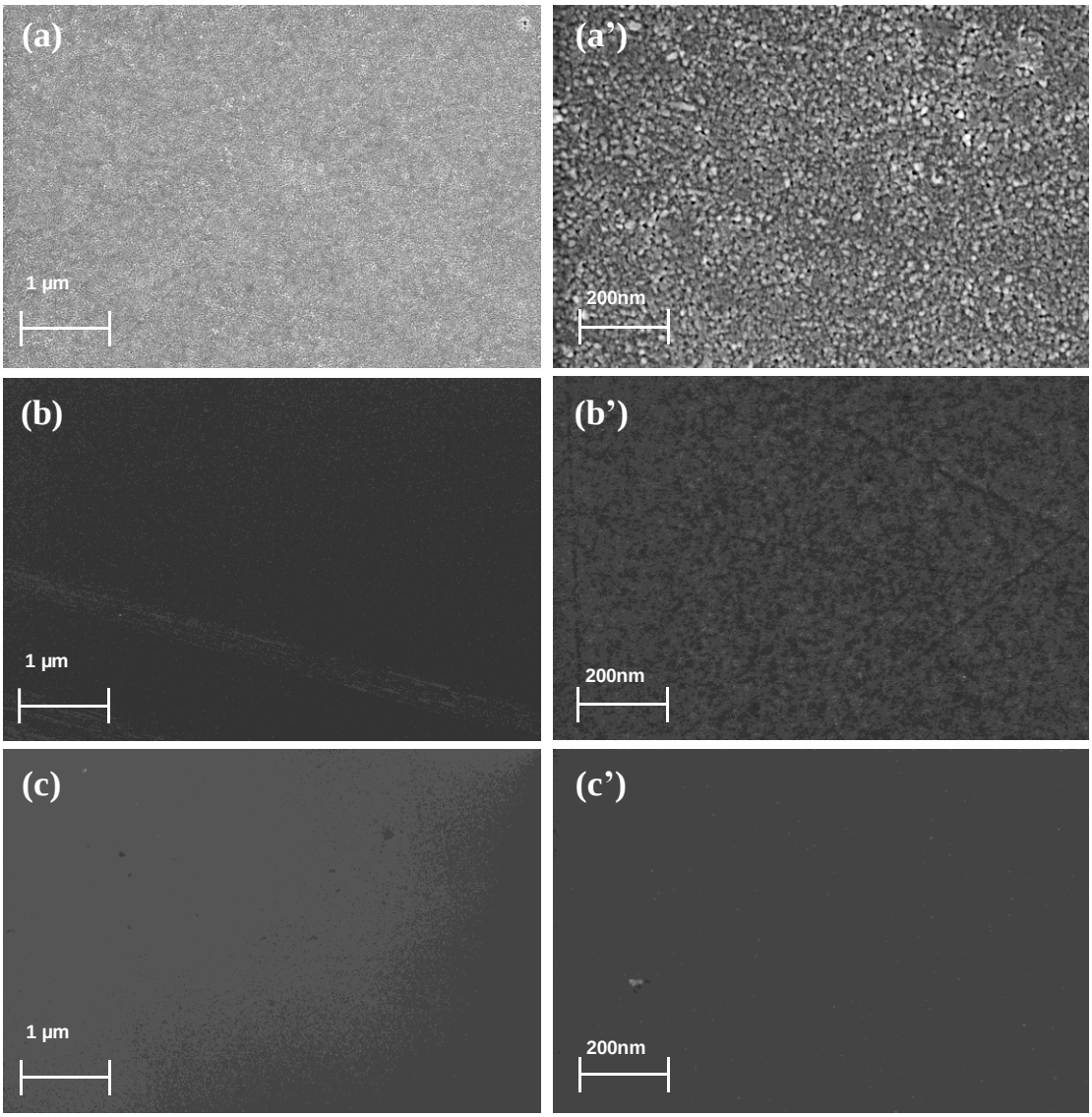

Figure 6.21: *SEM micrographs of samples annealed at 1100 ^{o}C. Low magnification images are shown of (a) un-irradiated, (b) irradiated with Xe to a fluence of 3.4×10^{14} cm^{-2} and (c) irradiated with Xe to a fluence of 8.4×10^{14} cm^{-2}. The corresponding high magnification images are shown in (a'), (b') and (c').*

The crystallization observed by Raman spectroscopy in Figure 6.20 is also evident in the SEM images shown in Figure 6.21. After implantation the surfaces were featureless, as it is typical of bombardment induced amorphous SiC wafers [Mal13]. As can be seen from Figure 6.21 (a and a'), annealing of the un-irradiated but Sr implanted samples resulted in crystal regrowth

and recrystallization competing with each other, eventually resulting in a polycrystalline surface layer with pores in it. There are some changes on the surface of the irradiated sample at low fluence (i.e. 3.4×10^{14} cm^{-2}) after annealing at 1100 ˚C while there are no major changes on the surface of the sample irradiated at higher fluence (i.e. 8.4×10^{14} cm^{-2}) after annealing at the same temperature (see Figure 6.19 ((c') and (d')) and Figure 6.21 ((b') and (c'))). The featureless surface of the samples irradiated at higher fluence (i.e. 8.4×10^{14} cm^{-2}) after annealing at 1100 ˚C indicates that we have smaller crystallites on the surface as compared to samples irradiated to lower fluence. This in agreement with the Raman results in Figure 6.20, where LO peak in the irradiated samples at fluence of 8.4×10^{14} cm^{-2} has larger shift toward lower wavenumber and increase in the FWHM which indicating smaller crystallites.

This difference in the grains size between un-irradiated and irradiated samples after annealing (showed in Raman and SEM results in Figures (6.20 and 6.21)) can be explained by the final grain size equation (see equation 6.4). Equation 6.4 shows that the final grain size (A_G) is inversely proportional to the rate of nucleation per unit amorphous area $\in r_n$. Since the un-irradiated but Sr implanted samples were amorphous before annealing (see Figure 6.18), the final grain size (A_G) will be larger compared to the irradiated samples which were composed of crystallites that were randomly orientated in an amorphous matrix before annealing [Hal15, Hal16].

The nano-crystallites in the irradiated samples in Figure 6.21 (b and b') and (c and c'), are more clearly visible after annealing these samples at 1200 ºC as can be seen in Figure 6.22 (b and b') and (c and c'). Also, more pores appeared on the surface. A comparison of the results in Figure 6.21 (b and b') and (c and c') and Figure 6.22 (b and b') and (c and c') shows that the increase in temperature which increases the mobility of atoms led to the increase in average crystal size, in line with crystal growth theory [But51, Hir60].

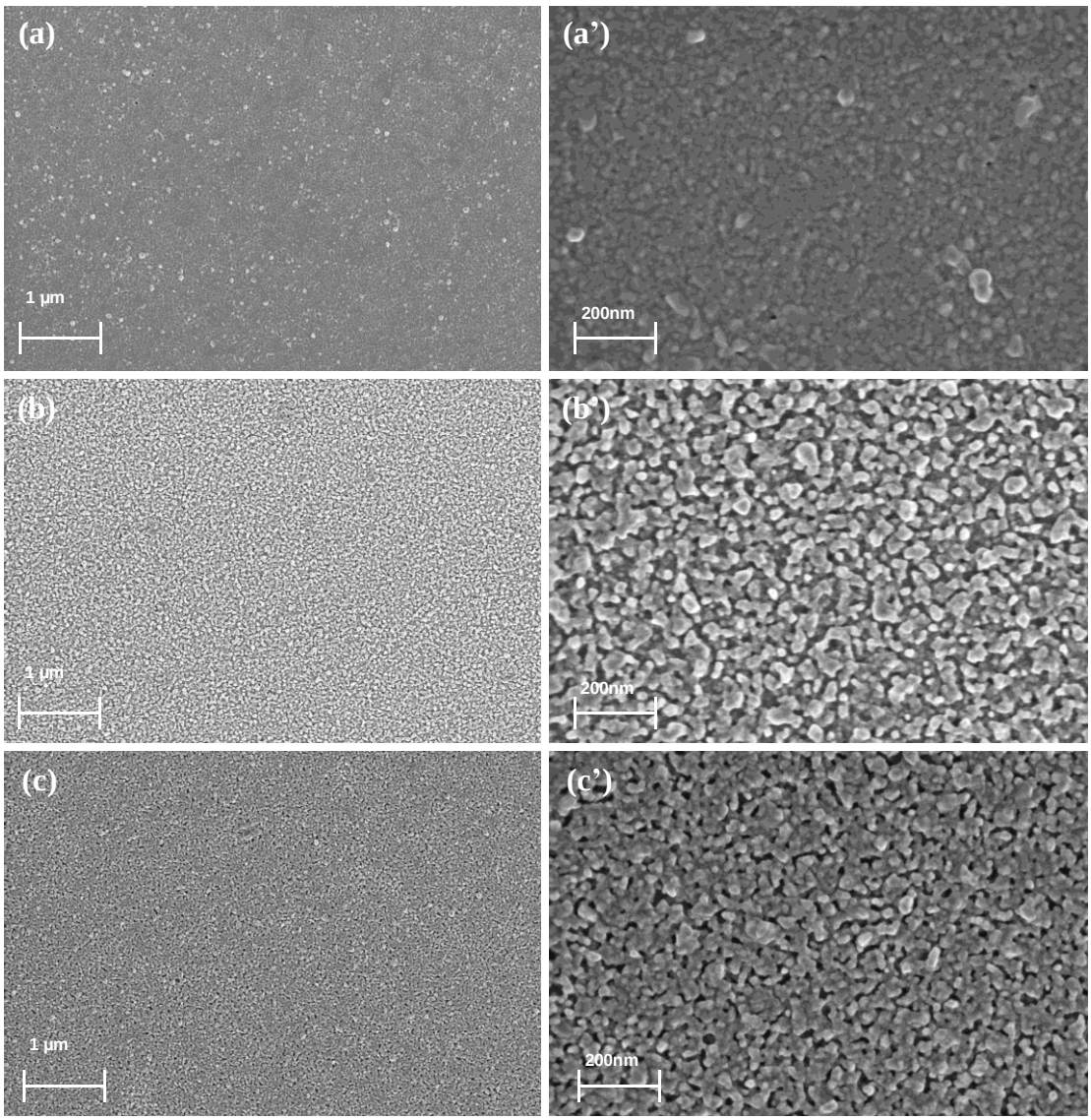

Figure 6.22: *SEM micrographs of samples annealed at 1200 ^{o}C. Low magnification images are shown of (a) un-irradiated, (b) irradiated with Xe to a fluence of 3.4×10^{14} cm^{-2} and (c) irradiated with Xe to a fluence of 8.4×10^{14} cm^{-2}. The corresponding high magnification images are shown in (a'), (b') and (c').*

The average crystal size of the un-irradiated sample annealed at 1100 ˚C and irradiated samples annealed at 1200 ˚C were determined from the SEM images in Figures 6.21 and 6.22 respectively. To ensure that the crystals were selected randomly, five straight lines were drawn randomly across the images in Figures (6.21 and 6.22) and the sizes of individual crystals along these lines were determined. The crystal size was measured with respect to the scale of the SEM image (i.e. 200 *nm*). Since the surface of irradiated and un-irradiated samples (Figure

6.21 (a and a') and Figure 6.22 ((b, b') and (c, c')) contain pores, the average pore size was also determined with respect to the scale of the SEM image (i.e. 200 *nm*). The average crystal and pore size for the irradiated and un-irradiated samples are listed in Table (6.3). From Table (6.3), at 1100 ˚C, the un-irradiated samples have larger crystals (around 44 *nm*) as compared to the crystals in the irradiated samples which cannot be measured from Figure 6.21 (b, b') and (c, c')) due to the inability of SEM to detect them at the specified scale (i.e. 200 *nm*). These nano-crystallites on the samples irradiated to fluences of 3.4×10^{14} cm^{-2} and 8.4×10^{14} cm^{-2} clearly appeared after annealing at 1200 ˚C (see Figure 6.22 ((b, b') and (c, c')) and have average crystal size of about 67 and 56 nm respectively - see Figure 6.22 and Table 6.3. The differences in the average crystal sizes between irradiated and un-irradiated but Sr implanted samples as shown in Table 6.3 is due to the difference in the recrystallization of these samples as mentioned above in Figure (6.20). Furthermore, these differences in the average crystal sizes it also could be due to the fact that the initial surfaces/layers were in different states before annealing, i.e. the un-irradiated samples were amorphous while the irradiated samples were composed of crystallites that were randomly orientated in an amorphous matrix [Hal15, Hal16].

Table 6.3: *Average crystal and pore sizes determined from SEM images for un-irradiated SiC annealed at 1100 ˚C and irradiated SiC annealed at 1200 ˚C.*

Name of the sample	**Average crystals (nm)**	
Un-irradiated – 1100 ˚C	**Average crystal size (nm)**	**Average pore size (nm)**
	44±22	19±8
Irradiated samples at 3.4×10^{14} cm^{-2} – 1200 ˚C	67±35	28±15
Irradiated samples at 8.4×10^{14} cm^{-2} – 1200 ˚C	56±26	31±18

After annealing the irradiated samples at 1200 ^{o}C, the Raman spectra showed increased narrowing of the TO and LO mode peaks of SiC indicates more recovery (i.e. recrystallization) of the SiC crystalline structure due to annealing at 1200 ^{o}C as seen in Figure 6.23. At 1200 ˚C, the samples irradiated to a fluence of 3.4×10^{14} cm^{-2} had a large average crystals size (see Table 6.3) and high intensity for LO mode (see Figure 6.23) as compared to the samples irradiated to a fluence of 8.4×10^{14} cm^{-2} and annealed in the same conditions. Thus, as the average crystal size increases, the LO phonon intensity increases in the Raman spectra.

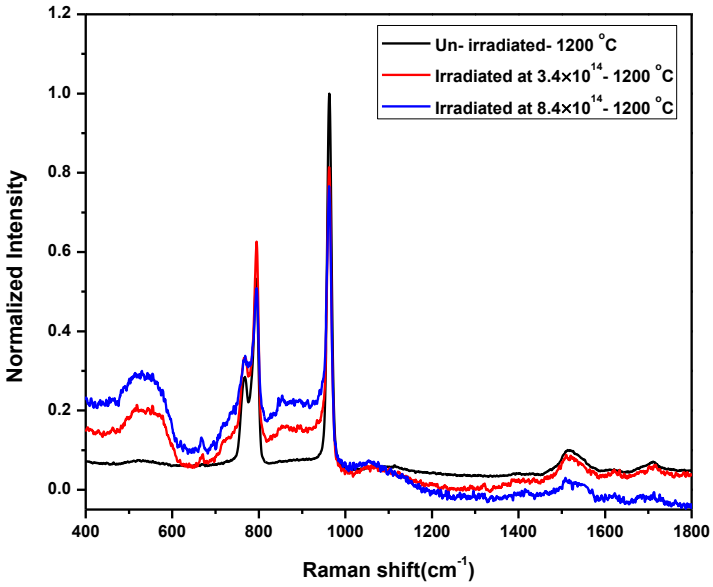

Figure 6.23: *Raman spectra of SiC implanted with Sr at room temperature then annealed at 1200 °C (un-irradiated - 1200 °C), implanted and then irradiated with Xe ions to fluences of 3.4×10^{14} cm^{-2} and 8.4×10^{14} cm^{-2} and finally annealed at 1200 °C.*

The SEM micrographs of both irradiated and un-irradiated but Sr implanted samples after sequentially annealing up to 1300 °C and 1400 °C are shown in Figure 6.24 and Figure 6.25 respectively. The micrographs show that the SiC crystallites increased in size with the increase in annealing temperature, in line with crystal growth theory [But51, Hir60]. The crystal growth leads to coalescence of crystals as shown in Figure 6.25 (b and b') and (c and c'). More pores/openings appeared in the SHI irradiated samples as seen in Figure 6.24(b') and (c'). In Figure 6.25 (i.e. annealed at 1400 °C) the average crystallite size became slightly larger with fewer and smaller pores compared to the samples annealed at lower temperatures. In contrast, these pores were larger and clearly visible in the un-irradiated but Sr implanted samples annealed at 1100 °C (Figure 6.21(a and a')) and in the irradiated samples annealed at 1300 °C (Figure 6.24 (b and b') and (c and c')). The same explanation of crystal growth used above is also applicable here.

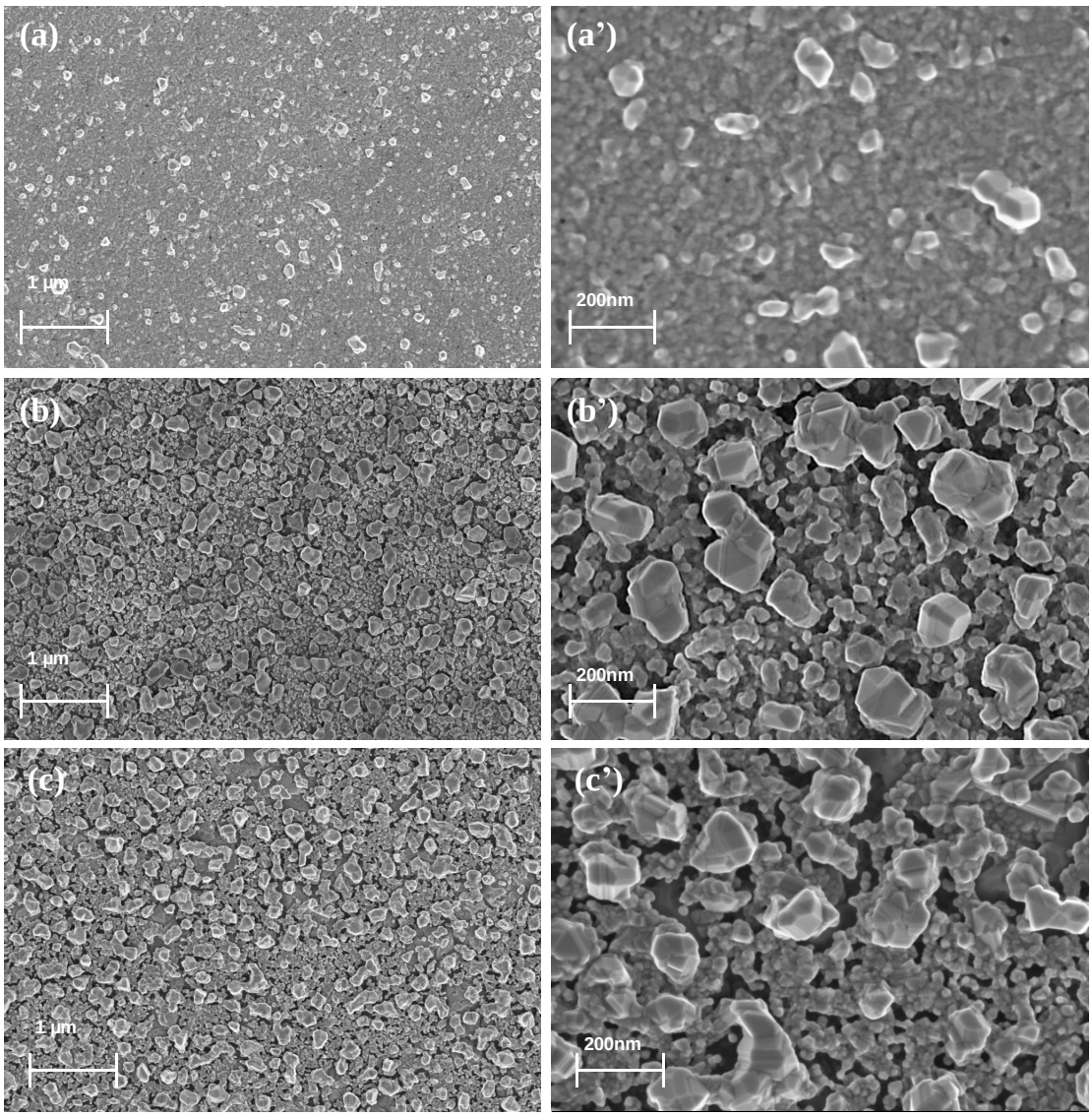

Figure 6.24: *SEM micrographs of samples annealed at 1300 ^{o}C. Low magnification images are shown of (a) un-irradiated, (b) irradiated with Xe to a fluence of 3.4×10^{14} cm^{-2} and (c) irradiated with Xe to a fluence of 8.4×10^{14} cm^{-2}. The corresponding high magnification images are shown in (a'), (b') and (c').*

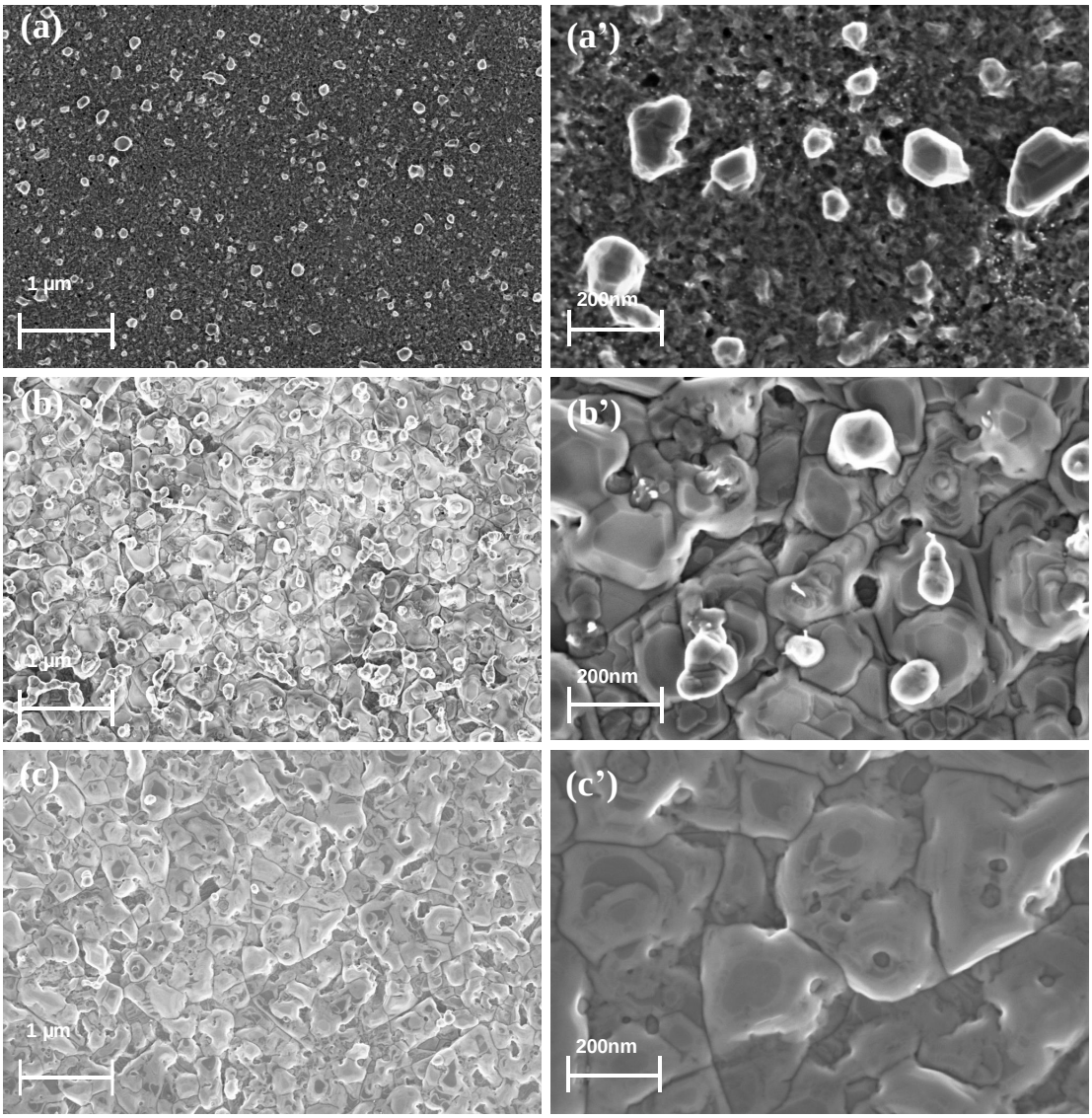

Figure 6.25: *SEM micrographs of samples annealed at 1400 °C. Low magnification images are shown of (a) un-irradiated, (b) irradiated with Xe to a fluence of 3.4×10^{14} cm^{-2} and (c) irradiated with Xe to a fluence of 8.4×10^{14} cm^{-2}. The corresponding high magnification images are shown in (a'), (b') and (c').*

Raman spectra of the un-irradiated and irradiated samples after sequentially annealing up to 1300 °C and 1400 °C are shown in Figure 6.26 (a) and (b) respectively. The Raman spectra shows further narrowing of the TO and LO modes for all the samples. This narrowing of FWHM indicates the recovery of the SiC crystalline structure due to annealing at 1300 °C and 1400 °C.

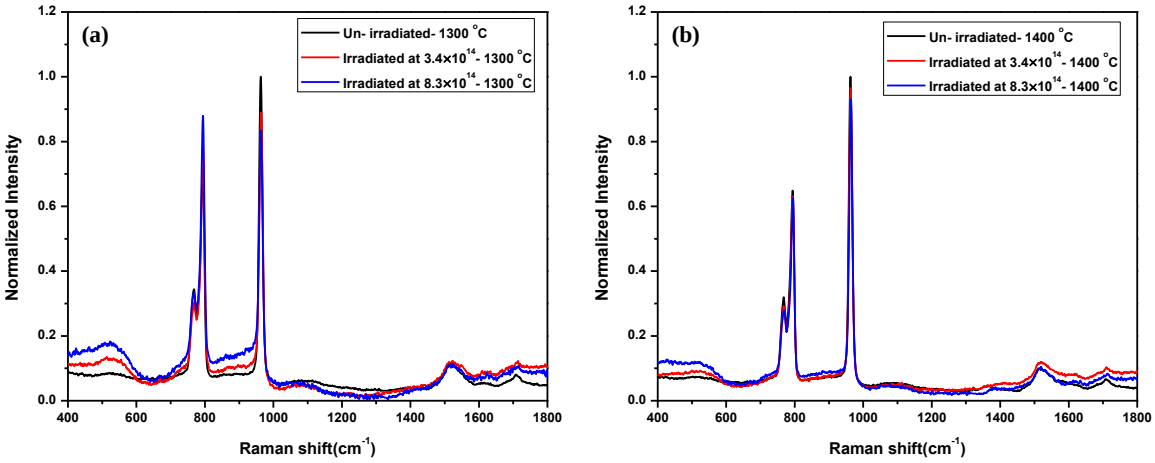

Figure 6.26: *Raman spectra of un-irradiated but Sr implanted and irradiated SiC sequentially annealed up to (a) 1300 and (b) 1400 °C.*

Raman spectra of the un-irradiated but Sr implanted and irradiated samples after sequentially annealing up to 1500 ^{o}C are shown in Figure 6.27. Annealing the un-irradiated but Sr implanted and irradiated samples at 1500 ^{o}C resulted in the appearance of peaks around 1360 cm^{-1} and 1580 cm^{-1} corresponding to D and G peaks respectively. The D and G peaks were found to be the more dominant in all the carbon materials. The C-C peak at 1520 cm^{-1} (which represents the second-order Raman lines of crystalline SiC [Sor06]) in the un-irradiated and irradiated samples annealed at temperatures from 1100 to 1400 ^{o}C (see Figures 6.20, 6.23 and 6.26) was still present after annealing at 1500 ˚C, but it partially merged with G peak at 1580 cm^{-1}. This indicates the presence of a carbon layer on the sample surfaces after annealing at 1500 ^{o}C. This result of decomposition of SiC leaving a thin carbon layer on the surface is in agreement with vacuum annealing of polycrystalline SiC at 1800 ^{o}C [Ber12]. The difference in the D and G peaks intensities shown in the Raman spectra of the un-irradiated but Sr implanted and irradiated (which implanted first then irradiated by SHI) samples after annealing at 1500 ˚C is due to the defect density in a carbon layer formed on the surfaces of these samples [Sai11]. The LO mode of SiC for the un-irradiated but Sr implanted sample at about 964 cm^{-1} had a slightly higher intensity compared to that of the SHI irradiated samples. This suggests that the un-irradiated sample had on average larger crystals compared to the irradiated samples. The difference in the average crystals size between the irradiated and un-irradiated but Sr implanted samples after annealing sequentially up to 1500 ˚C can be proven by calculating the average crystals size from the SEM images in Figure 6.28. However, it is very difficult to measure the average crystal sizes from the SEM images because these samples are mostly covered by the

carbon after annealing at 1500 ˚C (especially for the irradiated samples at high fluence - see Figure 6.28 (c) below).

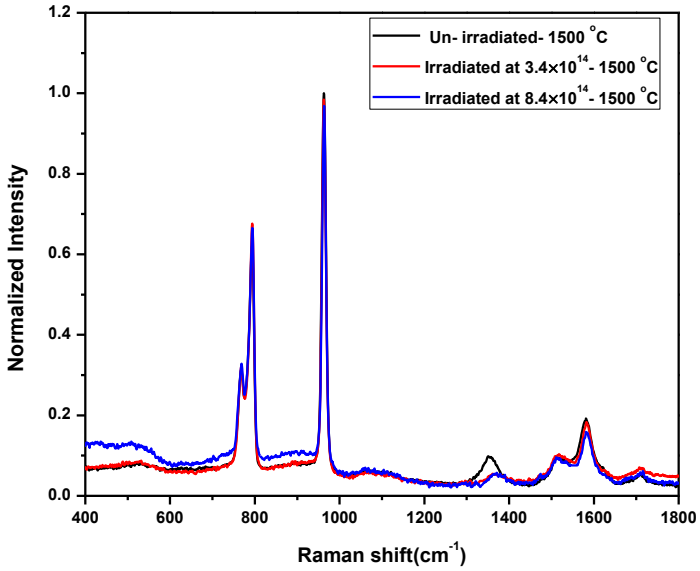

Figure 6.27: *Raman spectra of SiC implanted with Sr at room temperature and then sequentially annealed up to 1500 °C (Un-irradiated - 1500 °C), implanted and then irradiated to fluences of 3.4×10^{14} cm^{-2} and 8.4×10^{14} cm^{-2} and finally sequentially annealed up to 1500 °C.*

The SEM micrographs of both irradiated and un-irradiated samples after sequentially annealing up to 1500 °C are shown in Figure 6.28. Some of the crystallites can be seen to be protruding from the SiC substrate surface. This effect was more visible on the un-irradiated but Sr implanted samples with their larger crystallite sizes. This can be explained in terms of Wulff's law (i.e. the preferential growth of a crystal surface with a lower surface energy compared to another surface with a higher surface energy) [Wul01, Ber12]. In addition, thermal etching of SiC can play a contributing role at this temperature for all samples [Ber12]. Figure 6.28(a) shows thin strands of carbon material between the SiC crystallites and clusters with few and very small pores on the surface after annealing at 1500 °C. This carbon material on the surface of SiC after sequentially annealing up to 1500 °C was also observed in Raman and RBS spectra in Figures 6.27 and 6.29, respectively.

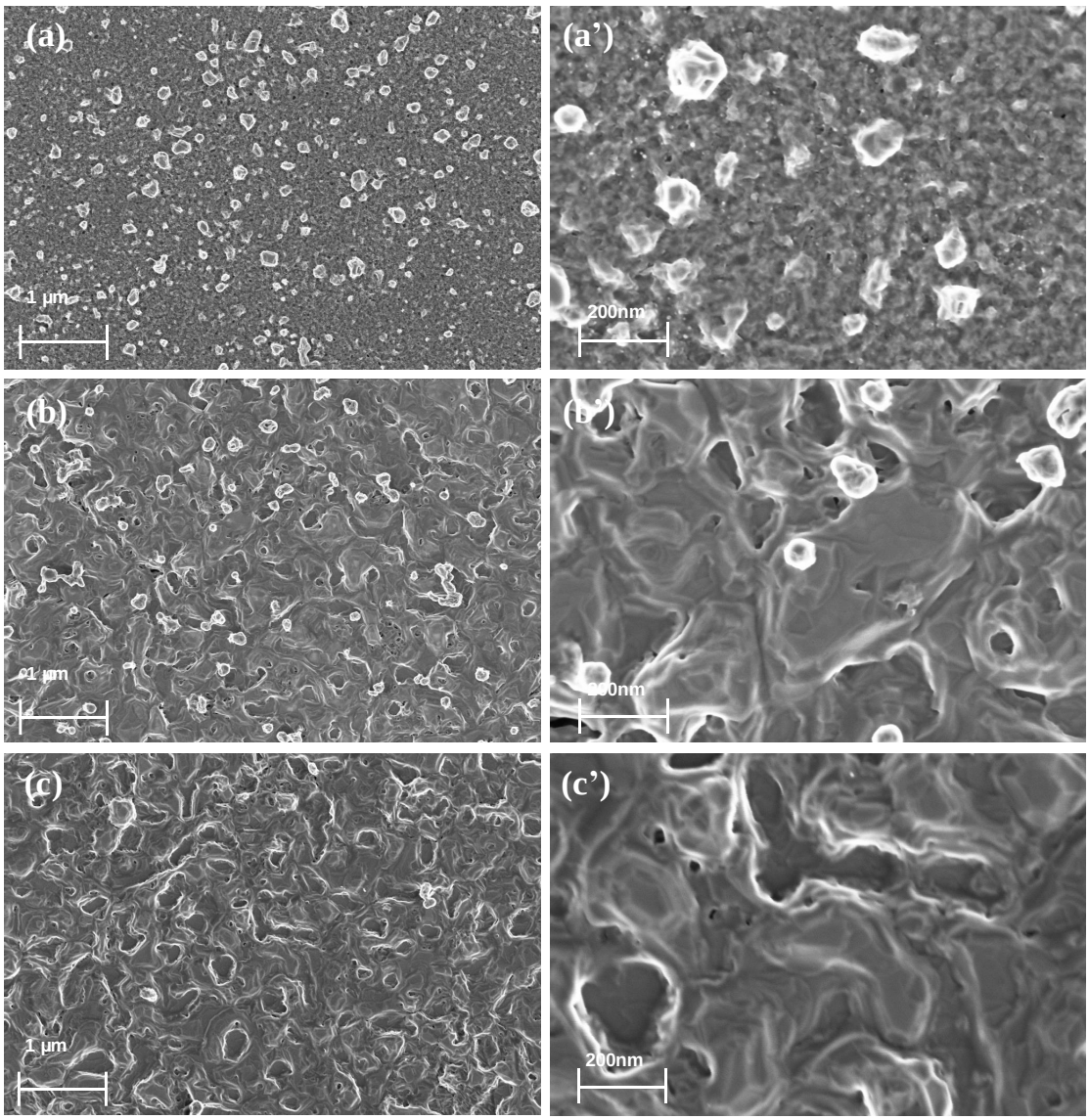

***Figure 6.28**: SEM micrographs of irradiated and un-irradiated samples after sequentially annealing up to 1500 °C, Low magnification images are shown of (a) un-irradiated, (b) irradiated with Xe to a fluence of 3.4×10^{14} cm^{-2} and (c) irradiated with Xe to a fluence of 8.4×10^{14} cm^{-2}. The corresponding high magnification images are shown in (a'), (b') and (c').*

Figure 6.29 shows the RBS spectra of SiC (both un-irradiated and irradiated samples) after sequentially annealing from 1100 to 1500 °C for 5 hours in steps of 100 °C. The Sr profile is not included in Figure 6.29. The arrows in Figure 6.29 indicate the Si and C surface channel positions. Sequential annealing of the samples up to 1500 °C resulted in the accumulation of carbon on the SiC sample surface, where higher (than the normal) counts on the edge corresponding to the carbon surface were observed. This was accompanied by the shift of the

Si surface channel position to lower energy channels indicating the presence of a carbon layer on the SiC surface. The free carbon on the surface was due to thermal decomposition of SiC and sublimation of silicon thus leaving a free carbon layer on the SiC surfaces. The decomposition of implanted SiC layers has been reported to occur at temperatures above 1400 °C [Fri09, Hal12, Ber12]. The decomposition of SiC observed from RBS results at 1500 °C correlates with the Raman results (Figure 6.27) which showed the appearance of the D and G peaks at this temperature indicating the presence of a carbon layer on SiC and with the SEM image shown in Figure 6.28(a).

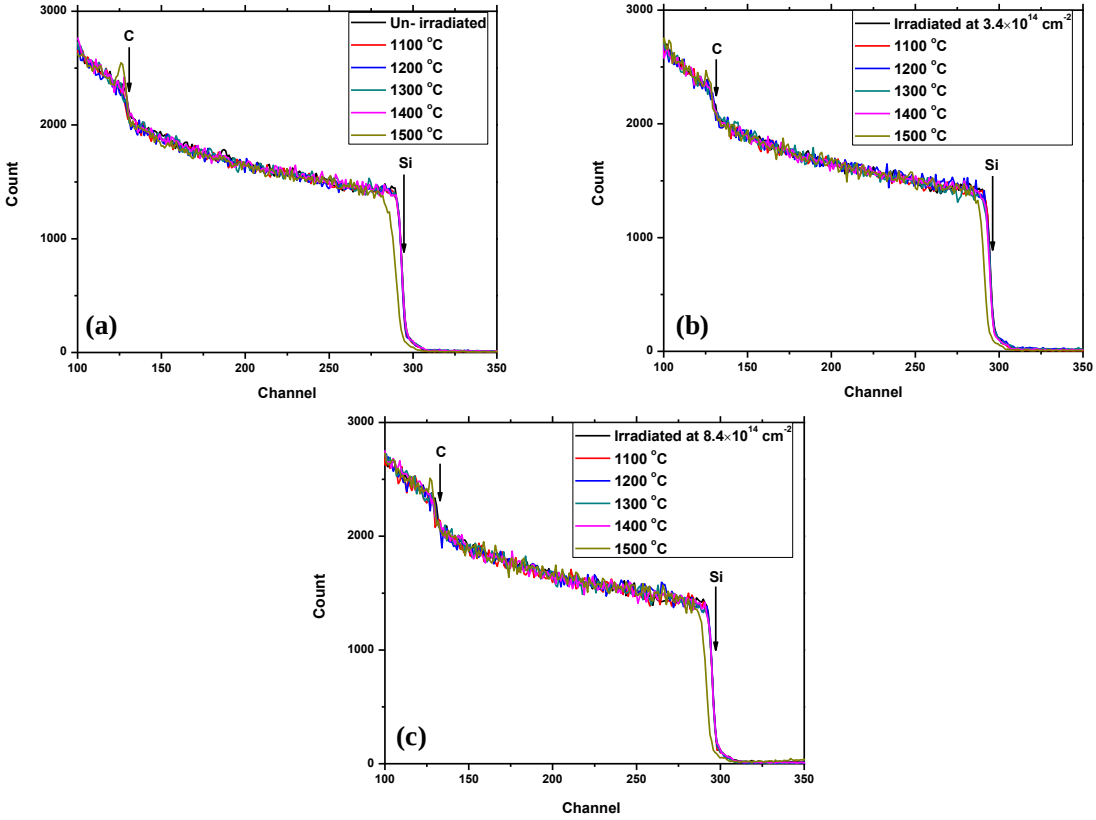

Figure 6.29: *RBS spectra of irradiated and un-irradiated SiC samples but Sr implanted before and after sequentially annealing up to 1500 °C. (a) Un-irradiated but Sr implanted. (b) and (c) Implanted with Sr then irradiation with Xe at room temperature to a fluence of 3.4×10^{14} cm^{-2} and 8.4×10^{14} cm^{-2} respectively.*

6.2.3. Effect of SHI irradiation on the migration behaviour of Sr in SiC

Migration behaviour of Sr implanted into SiC was investigated after SHI irradiation and sequential annealing. As shown in Figure 6.30, no migration of implanted Sr was observed after the SHI irradiation. Similar results have been reported for other implanted fission products after SHIs irradiation [Aud08, Hal15 and Hal16].

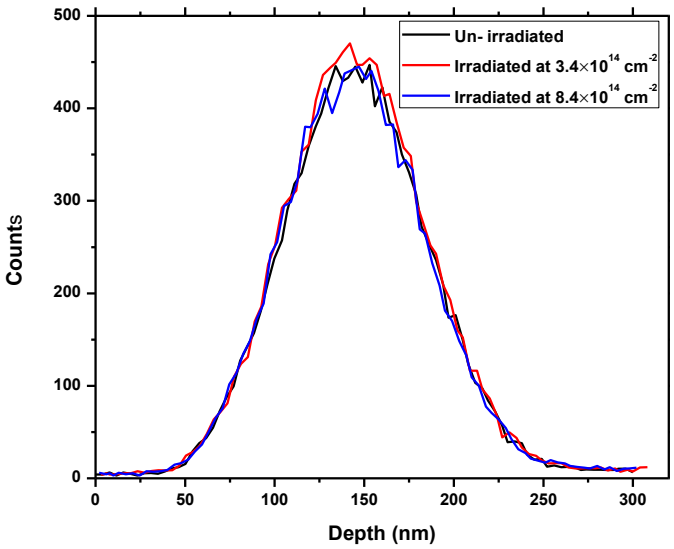

Figure 6.30: *Sr depth profile from un-irradiated and irradiated samples.*

The strontium depth profiles of irradiated and un-irradiated but Sr implanted samples after sequentially annealing at temperatures ranging from 1100 to 1500 ^{o}C for 5 hours are shown in Figure 6.31. Annealing the un-irradiated but Sr implanted samples at 1100 ^{o}C resulted in strong migration of Sr towards the surface accompanied by significant loss (of about 25%) of implanted Sr. This was due to the presence of pores in the surface of the un-irradiated but Sr implanted samples as shown in Figure 6.21 (a'). The ratio of retained strontium was calculated from the total counts/yield of Sr after annealing, divided by the counts of the as-implanted Sr peaks. At temperatures of 1200 °C and above, further loss of Sr through the surface was observed in the un-irradiated but Sr implanted sample - see Figure 6.31 (a) and Figure 6.32. The un-irradiated samples retained about 25% of Sr ions after sequentially annealing up to 1500 ^{o}C. This was due to very small pores as seen in Figure 6.28 (a and a'), compared to the un-irradiated but Sr implanted sample annealed at 1100 ^{o}C in Figure 6.21 (a and a'). In the irradiated samples, Sr migrate towards the surface and into the undamaged bulk after annealing at 1100 ^{o}C as shown in Figure 6.31 (b) and (c). This migration was accompanied by a slight loss of about 3% and no loss of implanted Sr for the samples irradiated at 3.4×10^{14} cm^{-2} and 8.4×10^{14} cm^{-2} respectively. At 1100 ˚C, the un-irradiated but Sr implanted samples which have pores on their surfaces (see Figure 6.21 and Table 6.3) showed high loss of Sr (see Figure 6.32) as compared to the irradiated samples which does not show any pores on their surfaces. Therefore, the different amounts of retained strontium after annealing were due to the difference in surface structure of the samples. Annealing the irradiated samples at 1200 ^{o}C shows significant loss of about 30% and 70% of Sr for the samples irradiated at 3.4×10^{14} cm^{-2}

and 8.4×10^{14} cm^{-2} respectively. This was due to the presence of pores on the surface of irradiated samples as seen in Figure 6.22 (b and b') and (c and c'). No Sr was retained in the 8.4×10^{14} cm^{-2} and 3.4×10^{14} cm^{-2} irradiated samples after annealing at 1300 and 1400 ^{o}C respectively - see Figure 6.32. A previous study by Friedland et al. [Fri12, Fri13] found that the implanted strontium is trapped and released by defect complexes at different temperatures, thereby not exhibiting normal Fickian diffusion which can be analyzed by the conventional equations and methods.

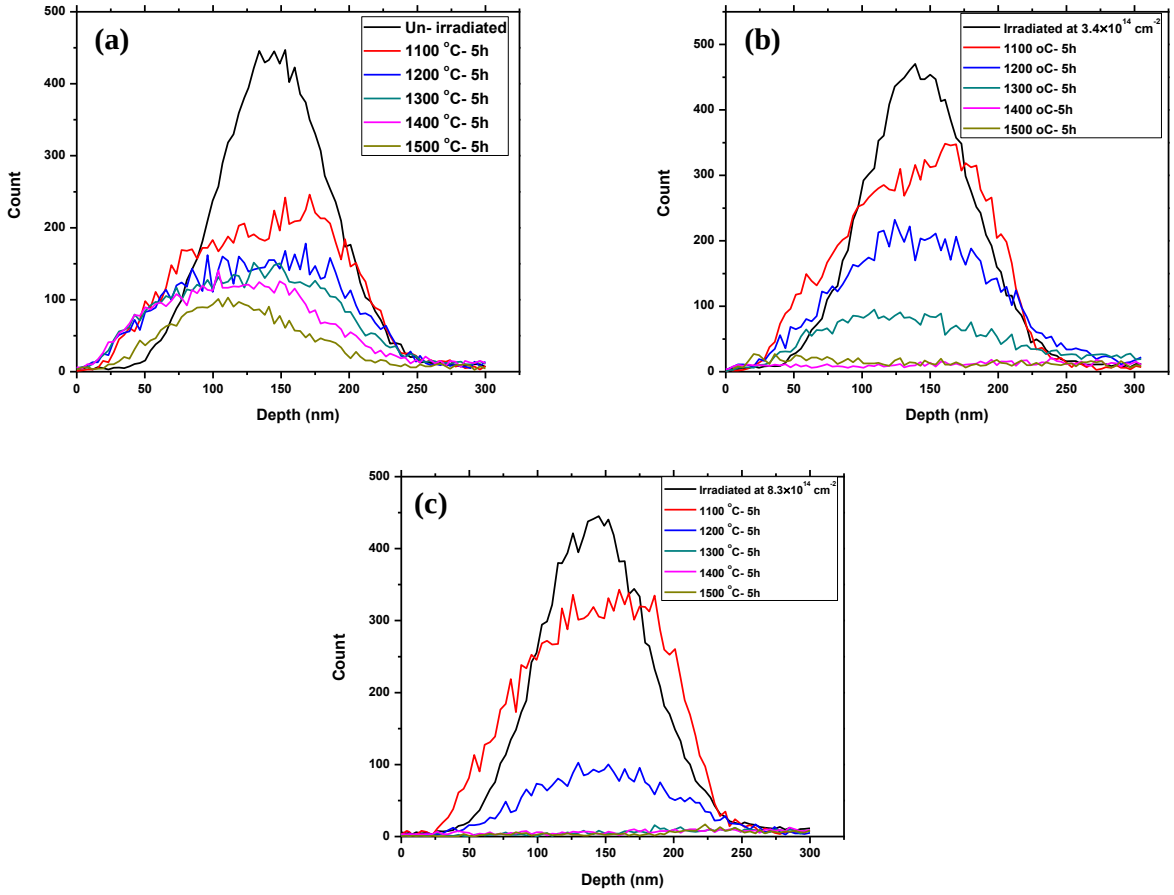

Figure 6.31: *RBS Sr depth profiles for irradiated and un-irradiated samples before and after annealing. (a) Sr depth profiles for un-irradiated samples. (b) and (c) Sr depth profiles for irradiated samples with Xe at room temperature to a fluence of 3.4×10^{14} cm^{-2} and 8.4×10^{14} cm^{-2} respectively.*

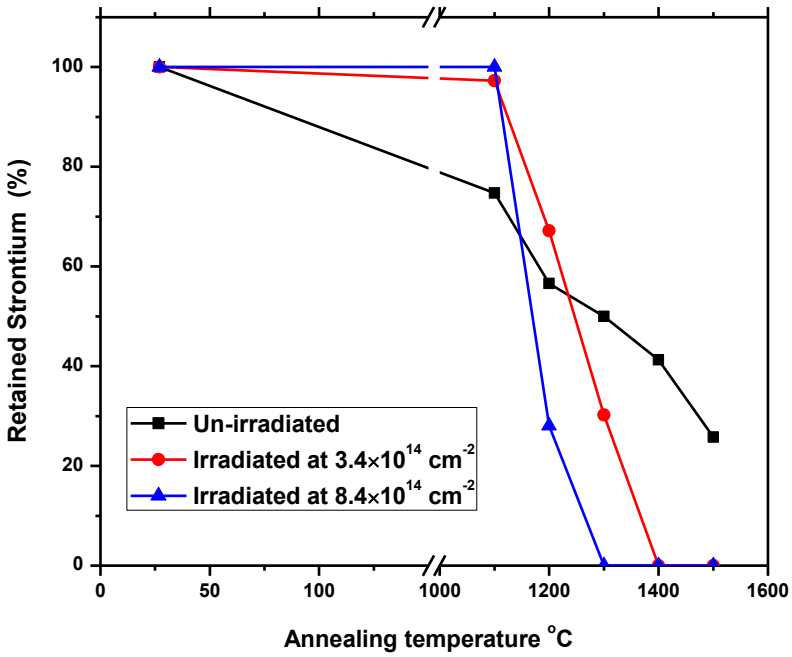

Figure 6.32: *The retained ratio of strontium in irradiated and un-irradiated samples before and after sequential annealing up to 1500 ^{0}C.*

The small loss of Sr in the un-irradiated samples and the high loss of Sr in the irradiated samples after sequentially annealing up to 1400 ^{o}C was due to the different structures in the annealed un-irradiated and irradiated samples. As discussed above in Figure 6.20, Table 6.3 and equation 6.4, annealing the un-irradiated but Sr implanted samples at 1100 ^{o}C led to the formation of rather large grains while annealing the irradiated samples produced fine grained structures. Annealing the un-irradiated but Sr implanted samples at 1200 and 1300 ^{o}C led to the formation of small sized pores on the surface while annealing the irradiated samples produced large sized pores as shown in Figure 6.22 and 6.24. This resulted in high amount of Sr released in the latter samples. From these results, it is quite clear that Sr loss is favoured in the irradiated SiC structure.

The low concentration of impurities in irradiated samples after annealing at 1200, 1300 and 1400 ^{o}C resulted in faster grain growth as shown in Figure 6.22 (b and c), 6.24 (b and c) and 6.25 (b and c) respectively. As discussed above in Figure 6.20, impurities usually inhibit crystal growth [But51, Hir60].

From Figures 6.1 (a), 6.2, 6.17(a) and 6.18, amorphous surface layers were produced by ion implantation of 360 keV ions of silver and strontium into polycrystalline 3C-SiC. The as-implanted SiC samples were then irradiated with 167 MeV Xe ions. From Figures 6.2 and 6.18,

irradiation of the as-implanted SiC samples with Xe (167 MeV) ions at room temperature to fluences of 3.4×10^{14} cm^{-2} and 8.4×10^{14} cm^{-2} caused some recrystallization of the initially amorphous SiC layer. This partial recrystallization of the initially amorphous SiC layer is caused by the high electronic energy deposited (~20 keV/nm – see Figure 6.1 (b)) by Xe ions irradiation at 167 MeV and thermal spikes. As shown in Figures 6.4 and 6.20, annealing the un-irradiated but implanted samples (Ag and Sr implanted separately into SiC) at 1100 °C caused full recrystallization of the silicon carbide resulting in the appearance of Raman characteristic peaks of SiC. However, annealing the SHI irradiated SiC samples at 1100 °C showed poor recrystallization with an abroad Si-Si peak and C-C peak. The differences in the recrystallization between the irradiated and un-irradiated but implanted samples annealed at 1100 ˚C is due to the amount of impurities (i.e. concentration of Ag atoms or Sr atoms) within the substrate – see Figures 6.11 and 6.32. At 1100 ˚C, the samples with high retained ratio of Ag showed full recrystallization (see Figures 6.4 and 6.11), while the samples with high retained ratio of Sr showed poor recrystallization (see Figures 6.20 and 6.32) after annealing in the same conditions. This suggest that Ag enhances the recrystallization of SiC, while Sr inhibit the recrystallization of SiC. The LO modes of SiC implanted with Ag and Sr separately (the un-irradiated samples) and annealed at 1100 ˚C shows the same wavenumber of about 964 cm^{-1} (see Figures 6.4 and 6.20). The LO modes for un-irradiated but implanted SiC samples had a significantly higher intensity compared to that of the SHI irradiated samples after annealing all the samples at 1100 ˚C. This suggests that the un-irradiated sample has average larger crystals compared to the SHI irradiated samples. The average crystal sizes were determined from the SEM images in Figures 6.5, 6.12, 6.13, 6.14, 6.21 and 6.22 and shown in Tables 6.1, 6.2 and 6.3. After annealing at 1100 ˚C and 1200 ˚C, the irradiated samples at high fluence of 8.4×10^{14} cm^{-2} had lowest LO mode as compared to the irradiated samples at lower fluence (3.4×10^{14} cm^{-2}) and un-irradiated samples (see Figures 6.4, 6.15, 6.20 and 6.23). A follow up analysis on the SEM images shows that a smallest average crystal size was estimated for irradiated samples at higher fluence (8.4×10^{14} cm^{-2}) as compared to the lower fluence irradiation (3.4×10^{14} cm^{-2}) and un-irradiated samples (see Tables 6.1, 6.2 and 6.3). This suggests that, as the average crystal size increases, the LO phonon intensity increases in the Raman spectra.

A common feature was seen after annealing sequentially up to 1500 °C, the irradiated and un-irradiated but implanted (Ag and Sr implanted separately into SiC) samples shows a carbon

layer appeared on the surface of all the samples (see Figures 6.6, 6.7, 6.8, 6.27, 6.28 and 6.29). This was due to the sublimation of silicon leaving a free carbon layer on the surface [Ber12]. Annealing the irradiated and un-irradiated but implanted samples sequentially up to 1500 ˚C, a strong release of Ag and Sr in SHIs irradiated samples was observed as compared to the un-irradiated but implanted samples (see Figures 6.11 and 6.32). The enhanced Ag and Sr release in SHIs irradiated samples was explained in terms of the high number of pores in the irradiated samples compared with the un-irradiated samples. The differences in the migration behavior of Ag and Sr is due to the difference in SiC structure and recrystallization in the irradiated and un-irradiated but implanted samples.

From the SEM results in sections 6.1 and 6.2, the crystal shapes and sizes seem to have different temperature dependencies. Porosity has been identified as the key feature that influences the shape and size of crystals [Kap73]. Furthermore, the amount of impurities that is present during crystal growth of SiC can influence the SiC crystal properties like crystal size and shape [Kis86]. Therefore, crystal sizes have different temperature dependences due to the presence of pores (see Figures 6.5, 6.7, 6.12, 6.13, 6.14, 6.21, 6.22, 6.24, 6.25 and 6.28) and different types and amounts of impurities (such as Ag atoms or Sr atoms) in the irradiated and un-irradiated but implanted samples (see Figures 6.11 and 6.32).

6.3 References

[Aud08] A. Audren, A. Benyagoub, L. Thome and F. Garrido, Ion implantation of iodine into silicon carbide: influence of temperature on the produced damage and on the diffusion behaviour. Nucl. Instrum. Methods Phys. Res. B. 266 (2008) 2810–2813.

[Bac13] M. Backman, M. Toulemonde, O. Pakarinen, N. Juslin, F. Djurabekova, K. Nordlund, A. Debelle and W. J. Weber, Molecular dynamics simulations of swift heavy ion induced defect recovery in SiC. Comput. Mater. Sci. 67 (2013) 261-256.

[Ben08] A. Benyagoub, Irradiation effects induced in silicon carbide by low and high energy ions. Nucl. Instrum. Methods Phys. Res. B 266 (2008) 2766-2771.

[Ben09] A. Benyagoub and A. Audren, Mechanism of the swift heavy ion induced epitaxial recrystallization in predamaged silicon carbide. J. Appl. Phys. 106 (2009) 083516.

[Ber12] N. G. van der Berg, J. B. Malherbe, A. J. Botha and E. Friedland, Thermal etching of SiC. Appl. Surf. Sci, 258 (2012) 5561 -5566.

[But51] W. K. Burton, N. Cabrera and F. C. Frank, The growth of crystals and the equilibrium structure of their surfaces. Phil. Trans. Roy. Soc. 243A (1951) 299- 358.

[Deb12] A. Debelle, M. Backman, L. Thome, W. J. Weber, M. Toulemonde, S. Mylonas, A. Boulle, O. H. Pakarinen, N. Juslin, F. Djurabekova, K. Nordlund, F. Garrido, and D. Chaussende, Combined experimental and computational study of the recrystallization process induced by electronic interactions of swift heavy ions with silicon carbide crystals. Physics Review B 86 (2012)100102.

[Ech95] E. Ech-chamikh, E. L. Ameziane, A. Bennouna, M. Azizan, T. A. Nguyen Tan, T. Lopez-Rios, Structural and optical properties of r.f.-sputtered Si_xC_{1-x}:O films. Thin Solid Films. 259 (1995) 18-24.

[Feg16] X. Feng and Y. Zang, Raman scattering properties of structural defects in SiC. Proce. 3rd Inter. Conf. Mech. Inf. Tech. (2016).

[Fel68] D. W. Feldman, J. H. Parker, W. J. Choyke and L. Patrick, Phonon dispersion curves by Raman scattering in SiC, polytypes 3C, 4H, 6H, 15R and 21R. Phys. Rev., 173 (1968) 787.

[Fri09] E. Friedland, J. B. Malherbe, N. G. van der Berg, T. Hlatshwayo, A. J. Botha, E. Wendler, W. Wesch, Study of silver diffusion in silicon carbide. J. Nucl. Mater. 389 (2009) 326–331.

[Fri11] E. Friedland, N. G. van der Berg, J. B. Malherbe, J. J. Hancke, J. Barry, E. Wendler, W. Wesch, Investigation of silver and iodine transport through silicon carbide layers prepared for nuclear fuel element cladding. J. Nucl. Mater. 410 (2011) 24-31.

[Fri12] E. Friedland, N. G. van der Berg, J. B. Malherbe, E. Wendler and W. Wesch, Influence of radiation damage on strontium and iodine diffusion in silicon carbide. J. Nucl. Mater. 425 (2012) 205-210.

[Fri13] E. Friedland, T. Hlatshwayo and N. van der Berg, Influence of radiation damage on diffusion of fission products in silicon carbide. Phys. Stat. Solidi C 10 (2013) 208-215.

[Gen14] X. Geng, F. Yang, N. Rohbeck, and P. Xiao, An original way to investigate silver migration through silicon carbide coating in TRISO particles. J. Am. Ceram. Soc., 97 (2014) 1979–1986.

[Ger15] T. J. Gerczak, B. Leng, K. Sridharan, J. L. Hunter, A. J. Giordani, T. R. Allen, Observations of Ag diffusion in ion Implanted SiC. J. Nucl. Mater. 461 (2015) 314-324.

[Hal10] T. T. Hlatshwayo, Diffusion of silver in 6H-SiC. PhD thesis, University of Pretoria. (2010).

[Hal12] T. T. Hlatshwayo, J. B. Malherbe, N. G. van der Berg, A. J. Botha, P. Chakraborty, Effect of thermal annealing and neutron irradiation in 6H-SiC implanted with silver at 350° C and 600° C. Nucl. Instrum. Methods Phys. Res. B 273 (2012) 61–64.

[Hal15] T. T. Hlatshwayo, J. H. O'Connell, V.A. Skuratov, M. Msimanga, R. J. Kuhudzai, E. G. Njoroge, J. B. Malherbe, Effect of Xe ion (167 MeV) irradiation on polycrystalline SiC implanted with Kr and Xe at room temperature. J. Phys. D: Appl. 48 (2015) 465306.

[Hal16] T. T. Hlatshwayo, J. H. O'Connell, V. A. Skuratov, E. Wendler, E. G. Njoroge, M. Mlambo, J. B. Malherbe, Comparative study of the effect of swift heavy ion irradiation at 500 ^{o}C and annealing at 500 ^{o}C on implanted silicon carbide. RSC Adv, 6 (2016) 68593-68598.

[Hal17] T. T. Hlatshwayo, L. D. Sebitla, E. G. Njoroge, M. Mlambo, J. B. Malherbea, Annealing effects on the migration of ion-implanted cadmium in glassy carbon. Nucl. Instrum. Methods Phys. Res. B 395 (2017) 34-38.

[Hir60] J. P. Hirth and G. M. Pound, Coefficients of evaporation and condensation. J. Phys. Chem. 64 (1960) 619–626.

[Hon11] E. Lo´pez-Honorato, H. Zhang, D. Yang, P. Xiao, Silver diffusion in silicon carbide coatings. J. Am. Ceram. Soc. 94 (2011) 3064–3071.

[Kap73] C.M. Kapadia and M.H. Leipold, The Mechanism of Grain Growth in Ceramics. Department of Metallurgical Engineering and Materials Science, University of Kentucky. (1973).

[Kim15] B. G. Kim, S. Yeo, Y. W. Lee and M. S. Cho, Comparison of diffusion coefficients and activation energies for Ag diffusion in silicon carbide. Nucl. Eng. Tech. 47 (2015) 608-616.

[Kis86] P.A. Kistler-De Coppi, W. Richarz, Phase transformation and grain growth in silicon carbide powders. Int. J. High Technol. Ceram. 2 (2) (1986) 99-113.

[Len16] B. Leng, H. Ko, T. J. Gerczak, J. Deng, A. J. Giordani, J. L. Hunter, D. Morgan, I. Szlufarska, K. Sridharan, Effect of carbon ion irradiation on Ag diffusion in SiC. J. Nucl. Mater. 471(2016)220-232.

[Liu10] L. Z. Liu, J. Wang, X. L. Wu, T. H. Li, and P. K. Chu, Longitudinal optical phonon–plasmon coupling in luminescent 3C–SiC nanocrystal films. Optics Letters 35 (2010) 4024- 4026.

[Mac02] H. J. MacLean and R. G. Ballinger, ANS Annual Winter Meeting, Washington, DC, Nov. (2002).

[Mac03] H. J. MacLean and R. G. Ballinger, ANS Global 2003, New Orleans, LA, Nov. (2003).

[Mac04] H. J. MacLean, Silver Transport in CVD Silicon Carbide. PhD Thesis, MIT, Department of Nuclear Engineering, 2004.

[Mal13] J. B. Malherbe, Topical Review: Diffusion and radiation damage in 6H-SiC. J. Phys. D Appl. Phys. 46 (2013) 473001 (27 pages).

[Mal17] J. B. Malherbe, P. A. Selyshchev, O. S. Odutemowo, C. C. Theron, E. G. Njoroge, D. F. Langa, T. T. Hlatshwayo, Diffusion of a mono-energetic implanted species with a Gaussian profile. Nucl. Instrum. Methods Phys. Res. B 406 (2017) 708-713.

[Oia13] X. Qiang, H. Li, Y. Zhang, S. Tian, J. Wei, Synthesis and Raman scattering of SiC nanowires decorated with SiC polycrystalline nanoparticles. Materials Letters 107 (2013) 315–317.

[Ric81] H. Richter, Z. P. Wang and L. Ley, The one phonon Raman spectrum in microcrystalline silicon. Solid State Commun., 39 (1981) 625.

[Sai11] R. Saito, M. Hofmann, G. Dresselhaus, A. Jorio and M. S. Dresselhaus, Raman spectroscopy of graphene and carbon nanotubes. Advances in Physics, 60 (2011) 413–550.

[Sch91] L. Schafer, X. Jiang and C. P. Klages, Applications of diamond films and related materials. Proceedings of the 1st International Conference. Auburn, AL. (1991) 121-128.

[Sne98] L. L. Snead, S. J. Zinkle, J. C. Hay, M. C. Osborne, Amorphization of SiC under ion and neutron irradiation. Nucl. Instrum. Methods. B 141 (1998) 123-132.

[Sor06] S. Sorieul, J. M. Costantini, L. Gosmain, L. Thome and J. J. Grob, Raman spectroscopy study of heavy-ion-irradiated α-SiC. J. Phys.: Condens. Matter 18 (2006) 1–17.

[Sub98] V. Subramanian, Control of nucleation and grain growth in solid-phase crystallized silicon for high- performance thin film transistors. PhD thesis, Department of electrical engnineering, Stanford University, 1998.

[Tal15] D. N. Talwar, Probing optical, phonon, thermal and defect properties of 3C–SiC/Si (001). Diamond and Related Materials. 52 (2015) 1-10.

[Tou00] M. Toulemonde, Ch. Dufour, A. Meftah and E. Paumier, Transient thermal processes in heavy ion irradiation of crystalline inorganic insulators. Nucl. Instrum. Methods Phys. Res. B 166-167 (2000) 903 – 912.

[Tou06] M. Toulemonde, W. Assmann, C. Dufour, A. Meftah, F. Studer and C. Trautmann, Experimental phenomena and thermal spike description of ion tracks in amorphisable inorganic insulators. Mat. Fys. Medd. 52 (2006) 263–292.

[Web04] W. J. Weber, F. Gao, R. Devanathan, W. Jiang, The efficiency of damage production in silicon carbide. Nucl. Instrum. Methods Phys. Res. B 218 (2004) 68.

[Web98] W. J. Weber, N. Yu, L. M. Wang, Structure and properties of ion-beam-modified (6H) silicon carbide. J. Nucl. Mater. 53 (1998) 253.

[Wen12] E. Wendler, Th. Bierschenk, F. Felgenträger, J. Sommerfeld, W. Wesch, D. Alber, G. Bukalis, L. C. Prinsloo, N. van der Berg, E. Friedland and J. B. Malherbe, Damage formation and optical absorption in neutron irradiated SiC. Nucl. Instrum. Methods Phys. Res. Sect. B 286 (2012) 97-101.

[Win94] W. Windl, K. Karch, P. Pavone, O. Schütt, D. Strauch, W. H. Weber, K. C. Hass, and L. Rimai, Second-order Raman spectra of SiC: Experimental and theoretical results from ab initio phonon calculations. Phys. Rev. B. Condens. Matter. 49 (1994) 8764-8767.

[Wul01] G. Wulff, Xxv. Zur Frage der Geschwindigkeit des Wachsthums und der Auflösung der Krystallflächen, Z. Krist. 34 (1) (1901) 449-530.

[Zha15] Y. Zhang, R. Sachan, O. H. Pakarinen, M. F. Chisholm, P. Liu, H. Xue and W. J. Weber, Ionization induced annealing of pre-existing defects in silicon carbide. Nat. Comm. 6 (2015) 8049.

[Zie13] J. F. Ziegler, www.SRIM.org, USA, 2013.

CHAPTER 7

CONCLUSION

The effect of ion implantation followed by swift heavy ion (SHI) irradiation and annealing on the structure and surface of polycrystalline 3C-SiC was investigated using Raman spectroscopy and scanning electron microscopy (SEM). Silver and strontium were implanted in separate polycrystalline 3C-SiC samples. Some of these samples (i.e. SiC implanted by Ag and Sr) were irradiated with SHIs. All samples were then annealed under vacuum to temperatures above the melting points of strontium and silver, respectively. In order to study the migration behaviour of Sr and Ag separately, the irradiated (i.e. implanted first then irradiated by SHI) and un-irradiated but implanted samples were annealed from 1100 to 1500 ˚C in steps of 100 ˚C for 5 hours and consequently characterized with Rutherford backscattering spectrometry (RBS).

Raman results showed that implantation of 360 keV Ag ions as well as 360 keV Sr ions into SiC at room temperature to fluence of 2×10^{16} cm^{-2} caused the disappearance of characteristic SiC Raman peaks. This is an indication that ion implantation at room temperature caused amorphization of the implanted layer of the silicon carbide. SEM results showed that the surface of the un-irradiated but implanted SiC was featureless compared to the virgin sample, which exhibited polishing marks. The disappearance of polishing marks in un-irradiated but implanted SiC surface is due to swelling of the SiC caused by the formation of amorphization. This confirmed the amorphization of SiC as revealed by Raman analysis. Irradiation of the as-implanted SiC with Xe (167 MeV) ions at room temperature to fluences of 3.4×10^{14} cm^{-2} and 8.4×10^{14} cm^{-2} caused the partial reappearance of broad SiC Raman characteristic peaks. The appearance of the broad characteristic SiC peaks after irradiation indicates some recrystallization of the initially amorphous SiC layer. This partial recrystallization of the initially amorphous SiC layer is due to the electronic energy deposition by SHIs and thermal spikes (i.e. thermal spikes are caused when SHIs transfer their energy into the target electrons).

Annealing the un-irradiated but implanted samples (Ag and Sr implanted separately into SiC) at 1100 °C caused full recrystallization of the silicon carbide resulting in the appearance of Raman characteristic peaks of SiC. However, annealing the SHI irradiated SiC samples at 1100 °C showed poor recrystallization with a broad Si-Si peak and C-C peak. Therefore, the recrystallization due to the annealing at 1100 °C in these samples was different. The differences

in the recrystallization between the irradiated and un-irradiated but implanted samples is due to the differences in the amount of impurities (i.e. concentration of Ag atoms or Sr atoms) within the substrate. At 1100 ˚C, the samples with high retained ratio of Ag showed full recrystallization, while the samples with high retained ratio of Sr showed poor recrystallization after annealing in the same conditions. This suggest that Ag assists the recrystallization of SiC, while Sr inhibit the recrystallization of SiC. The full width at half maximum (FWHM) of the SiC Raman prominent peak (i.e. longitudinal optical (LO) mode of SiC at around 964 cm^{-1}) increased from 9.4 cm^{-1} (virgin) to 10.6 cm^{-1} for un-irradiated but Ag implanted, 14.5 cm^{-1} and 18.8 cm^{-1} for irradiated samples to at fluences of 3.4×10^{14} cm^{-2} and 8.4×10^{14} cm^{-2}, respectively. This difference in FWHM was also observed in the SiC samples implanted with Sr ions at room temperature. Where the FWHM of the LO mode increased from 9.4 cm^{-1} (virgin) to 11.6 cm^{-1} for un-irradiated but Sr implanted, 11.8 cm^{-1} and 19.6 cm^{-1} for irradiated samples at fluences of 3.4×10^{14} cm^{-2} and 8.4×10^{14} cm^{-2} respectively. The FWHM of the un-irradiated but implanted sample was narrower compared to the irradiated samples (all annealed at 1100 ˚C). This suggests that annealing the un-irradiated but implanted samples at 1100 °C resulted in larger crystallites compared to irradiated samples annealed in the same conditions. Moreover, Raman results showed that the longitudinal optical (LO) phonon mode of SiC for the un-irradiated but implanted sample had a significantly higher intensity compared to that of the SHI irradiated samples. This confirms that the un-irradiated but implanted sample has average larger crystals compared to the irradiated samples.

The average crystal sizes were determined from the SEM images which were obtained from the irradiated and un-irradiated but implanted samples (Ag and Sr implanted separately) and annealed at temperatures from 1100 to 1400 °C. To ensure that the crystals were selected randomly, five straight lines were drawn randomly across the SEM images and the sizes of individual crystals along these lines were determined and averaged. Un-irradiated but Ag implanted samples annealed at 1100 ˚C showed long thin crystals growing in random directions with an average length of about 220 nm and average width of about 40 nm. The crystals in the un-irradiated but Ag implanted samples and annealed at 1200 ˚C (i.e. long thin crystals), had an average length of about 317 nm with average width of about 51 nm. The average crystals size in un-irradiated but Ag implanted samples and annealed at 1200 ˚C is larger than the average crystals size in un-irradiated but Ag implanted samples and annealed at 1100 ˚C. The increase in average crystal size depicts that the increase in annealing temperature increases the mobility of atoms and this is in line with crystal growth theory. The average crystal sizes were

not determined from the un-irradiated but Ag implanted samples annealed at 1300 ˚C, 1400 ºC and 1500 ºC. This is because of the unclear crystals and presence of some crystal clusters on the surfaces. The surfaces of the irradiated samples consisted of pores and irregular-shaped crystals after annealing at 1100 ˚C. The irradiated samples had average crystals sizes of less than 90 nm. The SEM results agrees with Raman results which shows that annealing the un-irradiated but Ag implanted samples at 1100 ˚C resulted in large average crystal size as compared to the irradiated samples annealed in the same conditions. The differences in the average crystal sizes between irradiated and un-irradiated but implanted samples was due to the fact that the initial surfaces/layers were in different states before annealing, i.e. the un-irradiated samples were amorphous while the irradiated samples were composed of crystallites that were randomly orientated in an amorphous matrix. The average crystal sizes were also determined from the SEM images which were obtained from the irradiated and un-irradiated but Sr implanted samples. At 1100 ˚C, the un-irradiated but Sr implanted samples had larger crystals (around 44 *nm*) as compared to the crystals in the irradiated samples which could not be measured from SEM images due to the inability of SEM to detect them at the specified scale (i.e. 200 *nm*). Annealing of the un-irradiated but Ag or Sr implanted samples at 1100 ˚C resulted in larger average crystal size as compared to irradiated samples. The LO mode of SiC for the un-irradiated but implanted sample had higher intensity compared to that of the SHI irradiated samples. Therefore, as the average crystal size increases, the LO phonon intensity increases in the Raman spectra.

After annealing irradiated and un-irradiated but implanted samples sequentially up to 1500 °C, Raman spectra showed appearance of two peaks at 1350 and 1580 cm^{-1} corresponding to the D and G bands which are more dominant in all the carbon materials. The presence of the D and G peaks indicates the presence of a carbon layer on the sample surfaces after annealing at 1500 ºC. The free carbon on the surfaces was due to thermal decomposition of SiC causing the sublimation of silicon thus leaving a free carbon layer on the surface.

The RBS results shows that SHIs irradiation alone did not induce any measurable migration of the implanted Ag or Sr. However, annealing the un-irradiated but Sr implanted samples at 1100 ˚C caused strong releasing of implanted strontium (about 25%) with slight releasing of Ag (<4%) in un-irradiated but Ag implanted samples. The enhanced Sr released in un-irradiated but Sr implanted samples was explained in terms of the high number of pores in their un-

irradiated but Sr implanted samples as compared to few pores in the un-irradiated but Ag implanted samples.

Annealing the SHI irradiated samples (implanted first with Ag then irradiated) at 1100 ^{o}C resulted in significant loss of about 42% and 54% of implanted Ag in both the SHI irradiated samples at fluences of 3.4×10^{14} cm^{-2} and 8.4×10^{14} cm^{-2}, respectively. This was due to the presence of large number of pores in the surfaces of the SHI irradiated samples. The diffusion coefficient of Ag was calculated for the irradiated samples annealed at 1100 ˚C and un-irradiated samples annealed from 1100 to 1300 ˚C. The diffusion coefficients of Ag in the irradiated samples annealed from 1200 to 1500 ˚C could not be determined. This is due to the fast migration of implanted Ag out of the surface leaving a too low concentration of Ag after annealing at 1200 ˚C. Also, the diffusion coefficient of Ag was not determined in un-irradiated samples annealed at 1400 and 1500 ˚C due to asymmetric profiles (i.e. not Gaussian). At 1100 ˚C, the irradiated samples (implanted first with Ag then irradiated) at fluences of 3.4×10^{14} cm^{-2} and 8.4×10^{14} cm^{-2} has a diffusion coefficients of 2×10^{-20} m^2/s and 3.2×10^{-20} m^2/s, respectively. However, after annealing at 1100 ˚C, there was no determinable diffusion coefficient for Ag in un-irradiated but Ag implanted samples. After annealing the un-irradiated but Ag implanted samples at 1200 and 1300 ˚C, the diffusion coefficient (D) was 6.7×10^{-21} m^2/s, 1.6×10^{-20} m^2/s, respectively. These results indicate that bombardment with swift heavy ions enhances the diffusion of Ag in SiC.

Annealing the SHI irradiated samples (implanted first with Sr then irradiated) at 1100 ^{o}C caused Sr to migrate towards the surface and into the undamaged bulk with slightly loss of about 3% and no loss of implanted Sr for the samples irradiated at 3.4×10^{14} cm^{-2} and 8.4×10^{14} cm^{-2} respectively. At 1100 ˚C, the un-irradiated but Sr implanted samples which have pores on their surfaces showed high loss of Sr as compared to the irradiated samples which does not show any pores on their surfaces. Therefore, the different amounts of retained strontium after annealing were due to the difference in surface structure of the samples. The implanted strontium is trapped and released by defect complexes at different temperatures, thereby not exhibiting normal Fickian diffusion which can be analyzed by the conventional equations and methods. The un-irradiated but Sr implanted sample retained about 25% of Sr ions after sequentially annealing up to 1500 ^{o}C, while no Sr ions were retained in the irradiated samples (at fluences of 8.4×10^{14} cm^{-2} and 3.4×10^{14} cm^{-2}) after annealing at 1300 and 1400 ^{o}C,

respectively. These differences in the migration behaviour of Sr is due to the difference in SiC structure and recrystallization in the irradiated and un-irradiated but Sr implanted samples.

CHAPTER 8

RESEARCH OUTPUT

The work presented in this thesis has contributed to several publications and conference presentations. A summary of the outputs is presented below:

8.1 PUBLICATIONS IN PEER- REVIEWED JOURNALS.

[1] H.A.A. Abdelbagi, V.A. Skuratov, S.V. Motloung, E.G. Njoroge, M. Mlambo, T.T. Hlatshwayo and J.B. Malherbe, Effect of swift heavy ions irradiation on the migration behavior of strontium implanted into polycrystalline SiC. Nucl. Instr. Methods Phys. Res. B 451 (2019) 113-121.

[2] H.A.A. Abdelbagi, V.A. Skuratov, S.V. Motloung, E.G. Njoroge, M. Mlambo, J.B. Malherbe, J.H. O'Connell and T.T. Hlatshwayo, Effect of swift heavy ions irradiation in the migration of silver implanted into polycrystalline SiC. Nucl. Instr. Methods Phys. Res. B 461 (2019) 201-209.

8.2 CONFERENCE PRESENTATION

i. South African Institute of Physics (SAIP) conference that was held at the Stellenbosch University, South Africa in 2017 (Poster presentation)

ii. International Conference on Ion Surface Interactions (ISI) held in Moscow, Russia in 2017 (Poster presentation) where the presentation was awarded ‘Best poster presented by young participants’

iii. International Conference on Swift Heavy Ions in Matter and International Conference on Atomic Collisions in Solids (SHIM-ICACS) that was held at Caen-Normandy University, France in 2018 (Poster presentation).

iv. International Conference on Nuclear Microprobe Technology and Applications (ICNMTA) that was held at University of Surrey, England in 2018 (Poster presentation).